University of California
Santa Barbara

Characterizing local structure in complex oxides with quantitative scanning transmission electron microscopy

A dissertation submitted in partial satisfaction
of the requirements for the degree

Doctor of Philosophy
in
Materials

by

Jack Y. Zhang

Committee in charge:

Professor Susanne Stemmer, Chair
Professor James S. Speck
Professor Ram Seshadri
Professor Leon Balents

June 2016

The Dissertation of Jack Y. Zhang is approved.

Professor James S. Speck

Professor Ram Seshadri

Professor Leon Balents

Professor Susanne Stemmer, Committee Chair

April 2016

Characterizing local structure in complex oxides with quantitative scanning transmission electron microscopy

by

Jack Y. Zhang

If we knew what we were doing, it wouldn't be called Research

– Albert Einstein

Acknowledgements

None of this work would be possible without the support and efforts of a great number of people. Foremost, I would like to thank my advisor, Susanne Stemmer, for her guidance and direction over the last five plus years, and for teaching me how to think, write, and plan like a scientist. She believed in me from the beginning, through the failures and successes, and I will be forever grateful for her support.

I also owe much to my colleagues, both past and present. From the four other graduate students who arrived with me - Tyler Cain, Adam Kajdos, Clayton Jackson, and Varistha Chobpattana - and helped me through the trials and tribulations of graduate school, to the older students and post-docs who helped train me and provided insight that can only be gained from experience - Jinwoo Hwang, James LeBeau, Pouya Moetakef, Adam Hauser, Timo Schumann - and the younger students whom I have grown to depend on for help - Santosh Raghavan, Christopher Freeze, Evgeny Mikheev, Brandon Isaac, Patrick Marshall, Manik Goyal, Omor Shoron - I have been truly blessed to work with such a great group of individuals. I would especially like to thank Jinwoo Hwang, now a professor at Ohio State, for his guidance during his time here as a post-doc. He simultaneously played the role of mentor, colleague, and friend, and was instrumental in my success at UCSB.

I would like to thank my committee members - Profs. Speck, Seshadri, and Balents - for overseeing my project and their advice during meetings and exams, as well as providing research breadth and scope through collaborations in outside projects.

The facilities at UCSB have been expertly maintained since my tenure here, and for that I have to thank the CNSI microscopy staff, Mark Cornish and Stephan Kraemer. Their help has been key to me obtaining experimental data in a timely and efficient manner, as well as training me on the instruments.

I would also like to thank Paul Weakliem and Fuzzy Rogers, for their help in maintaining the computing clusters for the times I have had to delve into simulation work.

The staff in the MRL have been instrumental in making my life easier in terms of administrative processes, and especially Joanne McNie has helped me numerous times with questions and reimbursement procedures.

I would like to thank the Department of Defense for supporting me through an NDSEG fellowship, as well as the many other agencies who helped fund the research facilities and projects which I was a part of.

Lastly, I would like to thank my family and friends for their unwavering support and encouragement throughout this whole endeavor. Many of these people have been mentioned above as collaborators and group members, and it's my utmost pleasure to call them friends as well.

– *J.Y.Z.*

Curriculum Vitæ

Jack Y. Zhang

Education

2016 Doctor of Philosophy in Materials, University of California, Santa Barbara, CA 93106 USA.

2010 Bachelor of Science in Materials Science and Engineering, University of Florida, Gainesville, FL 32608 USA.

First Author Publications

2016 *Key role of lattice symmetry in the metal-insulator transition of $NdNiO_3$ films*, J. Y. Zhang, H. Kim, E. Mikheev, A. J. Hauser, and S. Stemmer. Sci. Rep. **6**, 23652 (2016). [DOI]

2015 *Variable-angle high-angle annular dark-field imaging: application to three-dimensional dopant atom profiling*, J. Y. Zhang, J. Hwang, B. J. Isaac, and S. Stemmer. Sci. Rep. **5**, 12419 (2015). [DOI]

2014 *Correlation between metal-insulator transitions and structural distortions in high-electron-density $SrTiO_3$ quantum wells*, J. Y. Zhang, C. A. Jackson, R. Chen, S. Raghavan, P. Moetakef, L. Balents, and S. Stemmer. Phys. Rev. B. **89**, 075140 (2014). [DOI]

2013 *Magnetism and local structure in low-dimensional, Mott insulating $GdTiO_3$*, J. Y. Zhang, C. A. Jackson, S. Raghavan, J. Hwang, and S. Stemmer. Phys. Rev. B. **88**, 121104(R) (2013). [DOI]

2013 *Symmetry lowering in extreme-electron-density perovskite quantum wells*, J. Y. Zhang, J. Hwang, S. Raghavan, and S. Stemmer. Phys. Rev. Lett. 110, 256401 (2013). [DOI]

Co-author Publications

2016 *Carrier density independent scattering rate in $SrTiO_3$-based electron liquids*, E. Mikheev, S. Raghavan, J. Y. Zhang, P. B. Marshall, A. P. Kajdos, L. Balents, and S. Stemmer. Sci. Rep. **6**, 20865 (2016). [DOI]

2016 *High-mobility $BaSnO_3$ grown by oxide molecular beam epitaxy*, S. Raghavan, T. Schumann, H. Kim, J. Y. Zhang, T. A. Cain, and S. Stemmer. APL Mater. **4**, 016106 (2016). [DOI]

2015 *Correlation between stoichiometry, strain, and metal-insulator transitions of $NdNiO_3$ films*, A. J. Hauser, E. Mikheev, N. E. Moreno, J. Hwang, J. Y. Zhang, and S. Stemmer. Appl. Phys. Lett. **106**, 092104 (2015). [DOI]

2015 *Gaps and pseudo-gaps at the Mott quantum critical point in the perovskite rare earth nickelates*, S. J. Allen, A. J. Hauser, E. Mikheev, J. Y. Zhang, N. E. Moreno, J. Son, D. G. Ouellette, J. Kally, A. Kozhanov, L. Balents, and S. Stemmer. APL Materials **3**, 062503 (2015). [DOI]

2015 *Two-dimensional electron liquid at the (111) $SmTiO_3/SrTiO_3$ interface*, S. Raghavan, J. Y. Zhang, and S. Stemmer. Appl. Phys. Lett. **106**, 132104 (2015). [DOI]

2014 *Extremely scaled high-k/$In_{0.53}Ga_{0.47}As$ gate stacks with low leakage and low interface trap densities*, V. Chobpattana, E. Mikheev, J. Y. Zhang, T. E. Mates, and S. Stemmer. J. Appl. Phys. **116**, 124104 (2014). [DOI]

2014 *Quantum critical behavior in confined $SrTiO_3$ quantum wells embedded in antiferromagnetic $SmTiO_3$*, C. A. Jackson, J. Y. Zhang, C. R. Freeze, and S. Stemmer. Nature Comm. **5**:4258 (2014). [DOI]

2014 *Scaled ZrO_2 dielectrics for $In_{0.53}Ga_{0.47}As$ gate stacks with low interface trap densities*, V. Chobpattana, T. E. Mates, J. Y. Zhang, and S. Stemmer. Appl. Phys. Lett. **104**, 182912 (2014). [DOI]

2013 *Growth window and effect of substrate symmetry in hybrid molecular beam epitaxy of a Mott insulating rare earth titanate*, P. Moetakef, J. Y. Zhang, S. Raghavan, A. P. Kadjos, and S. Stemmer. J. Vac. Sci. Technol. A. **31**, 041503 (2013). [DOI]

2013 *High-density two-dimensional small polaron gas in a delta-doped Mott insulator*, D. G. Ouellette, P. Moetakef, T. A. Cain, J. Y. Zhang, S. Stemmer, D. Emin, and S. J. Allen. Sci. Rep. **3**, 3284 (2013). [DOI]

2013 *Influence of plasma-based in-situ surface cleaning procedures on $HfO_2/In_{0.53}Ga_{0.47}As$ gate stack properties*, V. Chobpattana, T. E. Mates, W. J. Mitchell, J. Y. Zhang, and S. Stemmer. J. Appl. Phys. **114**, 154108 (2013). [DOI]

2013 *Structural origins of the properties of rare earth nickelate superlattices*, J. Hwang, J. Y. Zhang, A. Janotti, C. G. Van de Walle, and S. Stemmer. Phys. Rev. B. **87**, 060101(R) (2013). [DOI]

2013 *Temperature-dependence of the Hall coefficient of $NdNiO_3$ thin films*, A. J. Hauser, E. Mikheev, N. E. Moreno, T. A. Cain, J. Hwang, J. Y. Zhang, and S. Stemmer. Appl. Phys. Lett. **103**, 182105 (2013). [DOI]

2013 *Three-dimensional imaging of individual dopant atoms in $SrTiO_3$*, J. Hwang, J. Y. Zhang, A. J. DAlfonso, L. J. Allen, and S. Stemmer. Phys. Rev. Lett. **111**, 266101 (2013). [DOI]

2013 *Wear resistance of ZrC/TiN and ZrC/ZrN thin multilayers grown by pulsed laser deposition*, D. Craciun, G. Socol, G. Dorcioman, S. Niculaie, G. Bourne, J. Zhang, E. Lambers, K. Siebein, and V. Craciun. Appl. Phys. A. **110**, 3 (2013). [DOI]

2012 *Asymmetric interfacial abruptness in N-polar and Ga-polar GaN /AlN/GaN heterostructures*, B. Mazumder, M. H. Wong, C.A. Hurni, J. Y. Zhang, U.K. Mishra, and J. S. Speck. Appl. Phys. Lett. **101**, 091601 (2012). [DOI]

2012 *Coalescence of InP Epitaxial Lateral Overgrowth by MOVPE with V/III Ratio Variation*, N. Julian, P. Mages, C. Zhang, J. Zhang, S. Kraemer, S. Stemmer, S. Denbaars, L. Coldren, P. Petroff, and J. Bowers. J. E. M. **41**, 5 (2012). [DOI]

2012 *Growth and properties of $GdTiO_3$ films prepared by hybrid molecular beam epitaxy*, P. Moetakef, D. G. Ouellette, J. Y. Zhang, T. A. Cain, S. J. Allen, and S. Stemmer. J. Cryst. Growth **355**, 1 (2012). [DOI]

2012 *Nanoscale quantification of octahedral tilts in perovskite films*, J. Hwang, J. Y. Zhang, J. Son, and S. Stemmer. Appl. Phys. Lett. **100**, 191909 (2012). [DOI]

2012 *Process dependence of 1/f noise and defects in ion implanted p-type piezoresistors*, R. Dieme, J. Zhang, N. G. Rudawski, K. Jones, G. Bosman, M. Sheplak, and T. Nishida. J. Appl. Phys. **112**, 033702 (2012). [DOI]

2011 *Al-doped $HfO_2/In_{0.53}Ga_{0.47}As$ metal-oxide-semiconductor capacitors*, Y. Hwang, V. Chobpattana, J. Y. Zhang, J. M. LeBeau, R. Engel-Herbert, and S. Stemmer. Appl. Phys. Lett. **98**:142901 (2011). [DOI]

2011 *Electrostatic carrier doping of $GdTiO_3/SrTiO_3$ interfaces*, P. Moetaef, T. A. Cain, D. G. Ouellette, J. Y. Zhang, D. O. Klenov, A. Janotti, C. G. Van de Walle, S. Rajan, S. J. Allen, and S. Stemmer. Appl. Phys. Lett. **99**, 232116 (2011). [DOI]

2011 *Thin and hard ZrC/TiN multilayers grown by pulsed laser deposition*, D. Craciun, G. Bourne, J. Zhang, K. Siebein, G. Socol, G. Dorcioman, and V. Craciun. Surf Coat Tech. **205**:5493 (2011). [DOI]

2011 *Transport in ferromagnetic $GdTiO_3/SrTiO_3$ heterostructures*, P. Moetakef, J. Y. Zhang, A. Kozhanov, B. Jalan, R. Seshadri, S. J. Allen, and S. Stemmer. Appl. Phys. Lett. **98**:11210 (2011). [DOI]

Presentations

2014 *Control of Electronic and Magnetic Properties in Oxide Heterostruc-*

	tures, J. Y. Zhang, J. Hwang, C. A. Jackson, S. Raghavan, and S. Stemmer. International Microscopy Congress 2014. Poster Session. Prague, Czech Republic.
2014	*Metal-Insulator Transitions in Extreme Electron Density $SrTiO_3$ Quantum Wells*, J. Y. Zhang, J. Hwang, C. A. Jackson, S. Raghavan, and S. Stemmer. EMA 2014. Orlando, FL.
2013	*Metal-Insulator Transitions in Extreme Electron Density $SrTiO_3$ Quantum Wells*, J. Y. Zhang, J. Hwang, C. A. Jackson, S. Raghavan, and S. Stemmer. MRS Fall Meeting 2013. Boston, MA.
2011	*Exploring the Strain Sensitivity of Image Contrast in Quantitative STEM of $SrTiO_3$*, J. Y. Zhang, J. M. LeBeau, A.J. DAlfonso, L.J. Allen, and S. Stemmer. Microscopy & Microanalysis Conference 2011. Poster Session. Nashville, TN.
2010	*Effect of Crystallinity & Thickness on Hardness in ZrC Thin Films*, J. Y. Zhang, G. Bourne, and V. Craciun. STLE 2010. Las Vegas, NV.

Selected Honors

2012	NDSEG National Defense Science & Engineering Graduate Fellowship
2011	MSA Presidential Student Award
2010	UCSB Regents Special Fellowship

Abstract

Characterizing local structure in complex oxides with quantitative scanning transmission electron microscopy

by

Jack Y. Zhang

Perovskite oxides remain a material class with properties that can be difficult to predict. Strong electron correlations, coupling between electron, lattice, spin and orbital degrees of freedoms, combined with the versatility of the structure itself, result in a wide range of properties, with unique emergent phenomena that occur only at heterointerfaces. Structure plays an especially important role in determining the properties of perovskite oxides. Small distortions in the lattice, particularly rotations or tilts of the oxygen octahedra, can have large effects on the material's electrical and magnetic properties. One way we can tune these rotations is by growing thin film heterostructures, allowing us to tailor the properties of these materials in ways not possible in the bulk. Therefore, determining the local atomic structure in these films is critical for understanding the structure-property relationships, and the origin of any emergent behavior that may exist at an interface.

To that end, we utilize scanning transmission electron microscopy (STEM) to develop a link between the atomic structure and electrical/magnetic properties of three different systems: $SrTiO_3$ quantum wells between $GdTiO_3$ and $SmTiO_3$, $GdTiO_3$ quantum wells between $SrTiO_3$, and strained $NdNiO_3$. Using real-space and diffraction techniques, we obtain quantitative information on local octahedral rotations and observe the presence/absence of structural transitions. This information gives us new insight into the driving forces behind the metal-insulator transition and magnetic behavior of the differ-

ent material systems. We also continue the development of quantitative STEM for precise and accurate determination of 3D dopant atom configurations by using variable detector angles in the high angle annular dark field regime. By demonstrating the usefulness of obtaining angle-resolved scattering data, we provide a new avenue for improving STEM image contrast and atom visibility for future studies.

Contents

List of Figures

List of Tables

Chapter 1

Introduction

The perovskite structure, ABX_3, with different cations A and B, and anion X (usually oxygen), contains a vast variety of compounds [1] due to the many combinations of anions and cations that the structure can accommodate. This broad range of compounds contains an incredibly diverse range of physical, electrical, and magnetic properties. Furthermore, the ability to substitute most metallic ions found in the periodic table into the perovskite structure allows one to uniquely tailor the structure to achieve unique properties or enhance existing ones [2, 3].

The perovskite oxide subclass exhibits a wide range of physical properties, such as piezoelectricity [4], high dielectric response [4], high temperature superconductivity [5], colossal and giant magnetoresitance [6, 7], multiferroic [8] and Mott-insulating [9] properties, ferro-, ferri-, and antiferromagnetic properties [4, 9], temperature dependent metal insulator transitions [10], and thermoelectricity [11]. These properties make perovskites not only interesting from a scientific perspective, but also technologically significant in importance industries such as catalysis, ferroelectric memory capacitors, advanced electronics, telecommunications, and energy conversion. As a result, perovskite oxides remain one of the most intensely studied class of materials in condensed matter physics, chemistry, and materials science.

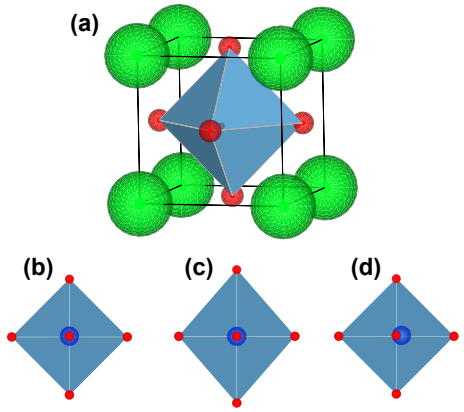

Figure 1.1: (a) Ideal perovskite unit cell (b) Undistorted BO_6 octahedra (c) Jahn-Teller type octahedra distortion (d) Cation displacement inside octahedra.

1.1 Role of Structure

The ideal perovskite structure, space group $Pm\bar{3}m$, is shown in Figure 1.1, with the A cations on the corners of the unit cell and the B cation in the center of the octahedra formed by anions located at face-center positions. The multifaceted structural, electronic, and magnetic properties of perovskite oxides arise from slight distortions of this underlying prototype cubic lattice[12] [*e.g.* Fig. 1.1(c, d)]. Due to the strong electron-lattice correlations in perovskite oxides, lattice distortions, and in particular, octahedral rotations of the BO_6 octahedra, can have a significant effect on the physical properties, particularly the electrical and magnetic properties, of the material [13]. For example, it was found that colossal magnetoresistance in manganese oxide compounds are largely influenced by MnO_6 octahedra deformations via the Jahn-Teller effect [14] and that the electron bandwidth can be controlled in a $Ca_{1-x}Sr_xVO_3$ system by only varying the V-O-V bond angle (VO_6 octahedral rotation)[15]. In thin film heterointerfaces, the individual properties of strongly-correlated oxides become even more interesting, with an enormous number of possible combinations leading the way for novel behavior and new emergent

phenomena [16]. Research into these materials will therefore require high-resolution structural characterization, preferably on the local scale, to understand the mechanisms behind the observed physical properties [17, 18].

1.1.1 Octahedral Tilts

Although the ideal perovskite is cubic (see Fig. 1.1), structural distortions can cause the unit cell to become triclinic, monoclinic, orthorhombic, tetragonal or rhombohedral. Most known perovskites are actually distorted from the prototypic structure [2]. The three mechanisms of distortion from the cubic phase are: distortion of the octahedra, such as elongation along one axis (e.g. Jahn-Teller distortion in $KCuF_3$ [19]), cation displacement within the octahedra (e.g. ferroelectric displacement of titanium in $BaTiO_3$ [20]), and rotation of the octahedra while maintaining corner-sharing connectivity. Figures 1.1(b-d) depict these first two types of octahedral distortions.

Octahedral tilts are the most common distortion, and occur to reduce the overall lattice energy (such considerations include the bonding nature, electronegativity, and size of the atoms). A comprehensive analysis of the interatomic forces behind octahedral tilts can be found in [21]. To maintain corner connectivity between BO_6 octahedra in adjacent unit cells, tilting one octahedron causes the neighboring octahedra to tilt in certain ways; the particular type of tilt results in the different possible space groups. In a previous work by Glazer, all possible combinations of octahedral tilts are indexed into 23 distinct tilt systems [22]. The Glazer notation is widely used in describing octahedral tilts and will be used in this work.

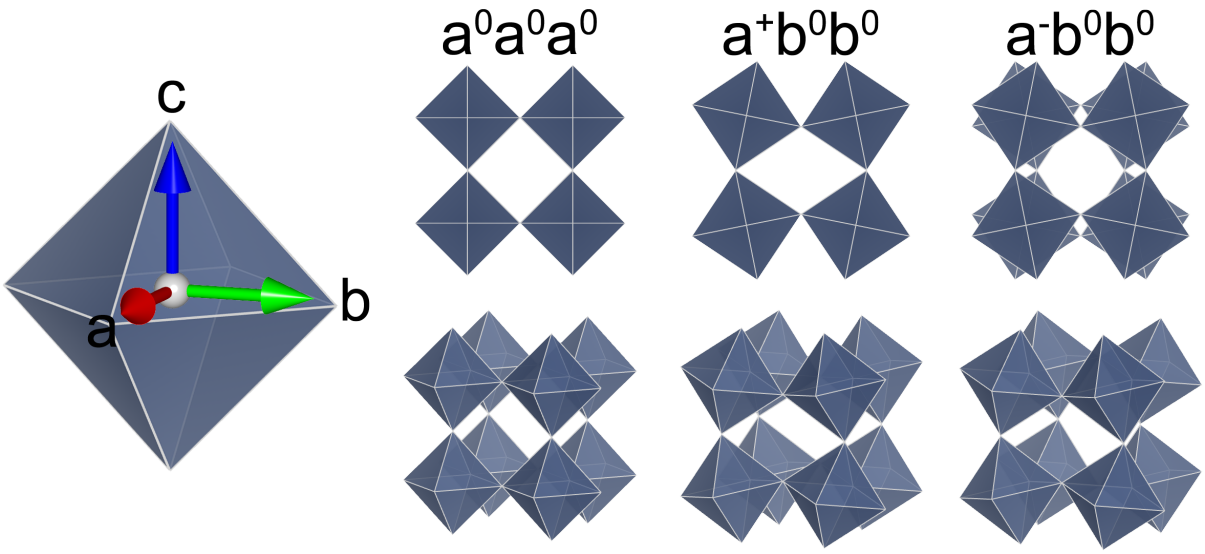

Figure 1.2: In Glazer notation, octahedral tilts can be described as a combination of rotations along the three tetrad axes (left). Schematics for the zero tilt, $a^0a^0a^0$, and one-tilt systems, $a^+b^0b^0$ and $a^-b^0b^0$ (right).

Glazer Notation

In Glazer notation, each octahedra rotation can be described as a combination of tilts about its three tetrad axes, as shown on the left in Figure 1.2. The rotation about each axes is described by a letter *(a, b,* or *c)*, according to the pseudocubic [100], [010], [001] directions, and a superscript symbol (+, -, or 0). The letter signifies the degree of the tilt about that axes, with different letters representing different magnitudes of rotation. The symbol describes the phase of tilt in the adjacent octahedra along that direction, since rotating an octahedra about one axis automatically constrains the tilts of adjacent octahedra in the perpendicular directions, but adjacent octahedra in the same direction can be tilted either in the same or opposite direction. A zero superscript indicates zero tilt along that axis. For example, the $a^0a^0a^0$ system signifies no rotations about each of the three axes, or a cubic cell, while $a^+b^0b^0$ indicates a one-tilt system, with in-phase tilts along the [100] axis. Alternatively, $a^-b^0b^0$ indicates a one-tilt system with out-of-phase

tilts along the [100] axis. These three systems are shown to the right in Fig. 1.2, for a $2 \times 2 \times 2$ octahedra supercell. Note that due to corner connectivity constraints, the octahedral tilt along the **a** axis automatically determines the tilt of adjacent octahedra perpendicular to **a**. For the in-phase tilt, adjacent octahedra along **a** are rotated in the same direction, while for the out-of-phase tilt, adjacent octahedra along **a** are rotated in the opposite direction.

1.1.2 Octahedral Tilts in Heterostructures

The growth of heterostructures offers a powerful way to additionally tailor the structure and properties of perovskite oxides, often in new and unexpected ways [23, 18, 24]. Unique physical phenomena can occur in thin film heterostructures, as a result of epitaxial strain and interfacial effects [25, 26], as well as reduced dimensionality through quantum confinement [27]. At interfaces, especially, we see the emergence of novel behavior not present in either of the bulk constituents [28, 29, 16], which offers significant opportunities for new novel devices for electronic and photonic applications [30]. Understanding the effects that occur at these interfaces, such as lattice coupling and structural coherency, is therefore key to understanding these emergent phenomena and a prerequisite for advanced materials design.

Both epitaxial coherency strain (the "clamping effect" as described by He [31]) and the presence of heterointerfaces is expected to modify the octahedral tilt rotations of thin films from that of the bulk material. For example, May showed that compressive and tensile strain induced different types of octahedral rotations in a $LaNiO_3$ film [32], confirmed by Hwang using an alternate approach [16]. Of particular interest is the octahedral behavior at the interface between two structurally different perovskites, such as the $GdTiO_3$ (orthorhombic)/$SrTiO_3$ (cubic) interface. Due to the geometric constraint of

corner connectivity between the BO_6 octahedra, modification of the octahedral rotations at an interface between structures with different octahedral tilts would be expected. It is unclear which structure's octahedra, or both, would be altered, and to what depth in the film that modification would extend to.

Density-functional theory calculations by Rondinelli examing the proximity effects a substrate with octahedral rotations had on a non-tilted film indicates that the substrate can induce its octahedral tilt onto a film at the interface, with an exponential decay to bulk film rotations away from the interface [25]. Another work by May studying $(LaNiO_3)_n$ (distorted perovskite)/$(SrMnO_3)_m$ (cubic perovskite) superlattices showed either the presence of large rotations or suppressed rotations depending on the superlattice composition [33]. These studies highlight the importance of careful substrate selection when growing oxide heterostructures, and how strain and symmetry can modify the structure of the film. An understanding of how these octahedral rotations are modified is crucial in controlling the electronic behavior of oxide heterostructures, as these rotations couple to the electronic bandwidth, and could allow for specific tuning of novel properties in these multifunctional perovskite oxides.

1.2 Measuring Octahedral Tilts

While critical in understanding the structure-property relationships, the measurement of octahedral tilts has remained a difficult problem. Oxygen spacings are often small and difficult to resolve using real space methods. Selected area electron diffraction (SAED) has been used to differentiate tilt systems [34] and aberration-corrected ultrahigh-resolution transmission electron microscopy (TEM) has been used to visualize oxygen displacements [17], but these techniques remain either qualitative in nature, require extensive simulations, or require access to state-of-the-art instrumenta-

tion/techniques. Other methods involve using synchrotron x-ray diffraction [32, 33] to look for half-order peaks caused by octahedral tilts, but these suffer from an inability to obtain local structural information, as the large probe size can only capture average structural information from large regions of the sample. These difficulties have so far precluded experimental octahedral characterization in any quantitative manner.

1.2.1 Transmission Electron Microscopy

To precisely characterize octahedral tilts and structural distortions locally, especially at interfaces, new characterization techniques need to be developed that can resolve these features on an atomic scale. Transmission electron microscopy (TEM) is well suited for such atomic resolution locally resolved studies. The TEM is an unparalleled characterization tool that offers high spatial resolution over a broad range of techniques. Atomic structure, crystal orientation, elemental composition, defect structure, and phase variation are just a few examples of the vast amount of potential information the instrument can measure. The two main techniques for atomic resolution imaging, scanning transmission electron microscopy (STEM) and high resolution transmission electron microscopy (HRTEM) are shown in Figure 1.3.

HRTEM uses a coherent parallel illumination system, while STEM uses a convergent electron probe that rasters across the sample to build up an image pixel-by-pixel. STEM has several advantages over conventional TEM. The use of a high angle annular dark field (HAADF) detector in STEM to detect electrons that have been scattered to high angles results in intuitive and directly interpretable images [35], as opposed to phase-contrast imaging of HRTEM, where image interpretation is complicated by contrast reversals [36, 37, 38]. Instead, the image contrast in HAADF STEM is highly sensitive to the atomic number of the atoms in the sample (Z-contrast images), and can be obtained in parallel

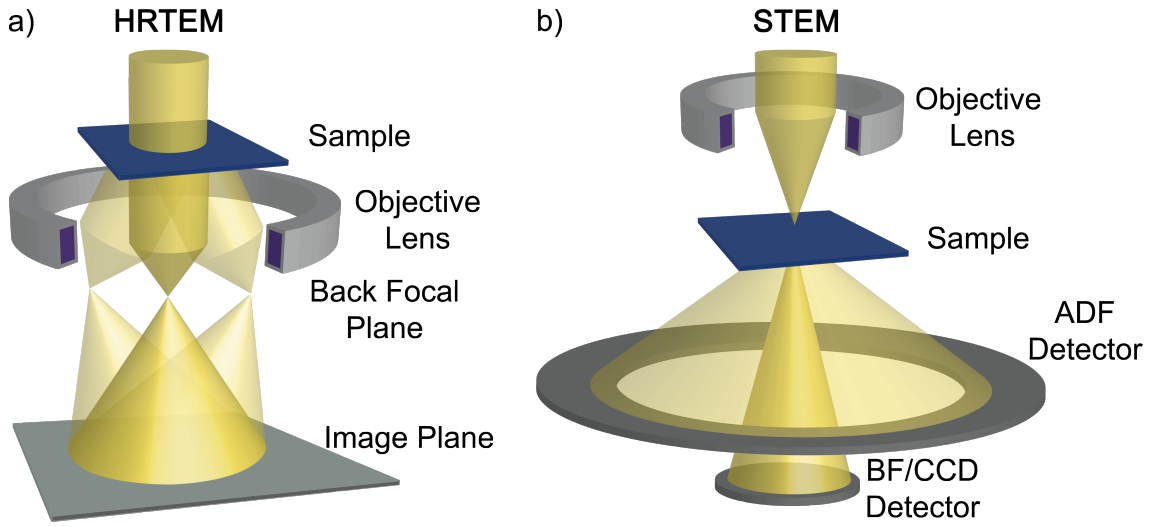

Figure 1.3: Schematic difference between (a) HRTEM and (b) STEM.

with bright field (BF) data, electron diffraction, or electron energy loss spectroscopy (EELS), an advantage no other characterization technique can provide.

In this thesis, we combine both real space imaging and diffraction techniques using STEM to measure and quantify the octahedral rotations in perovskite oxide thin films. Although oxygen atoms are too light to be directly observed in HAADF STEM [39], we show that the octahedral tilts can be inferred by measuring the heavier and more visible A-site cations, thereby avoiding the difficulties in analysis and interpretability of HRTEM. We also utilize position averaged convergent beam electron diffraction (PACBED) [40] to qualitatively verify the degree of octahedral tilt, and in conjunction with symmetry constraints, determine the tilt systems of epitaxially grown films. PACBED is described in greater detail in Appendix A, and can be obtained simultaneously with HAADF images using a CCD camera, as shown in Fig. 1.3(b).

1.3 Outline

This thesis dissertation is organized into four main chapters, each one covering a separate materials system. Chapter 2 focuses on metal-insulator transitions (MITs) in $SrTiO_3$ quantum wells grown between the rare earth titanates, $GdTiO_3$ and $SmTiO_3$. The changes in the local octahedral rotations are characterized by measuring the A-site cation displacements using HAADF STEM, and related to the electronic properties to give insight into the underlying physics behind the electronic transitions.

In Chapter 3, we use the same characterization technique to look at inverse structures, $GdTiO_3$ quantum wells grown between $SrTiO_3$, in order to study how the octahedral rotations in $GdTiO_3$ are affected by interfacial constraints, along with the subsequent magnetic response. Here, we also employ PACBED to confirm the structural distortions we measure using HAADF STEM.

Chapter 4 returns to the subject of metal-insulator transitions, but now we focus on the nickelate system, $NdNiO_3$, which has a fundamentally different origin of the MIT. Employing a liquid nitrogen cold stage holder, we use $in-situ$ STEM to acquire PACBED patterns from above and below the MIT temperature of strained $NdNiO_3$ films. From analysis of these patterns along with symmetry constraints from the epitaxial growth, we arrive at a new understanding of the driving forces behind the MIT.

The last research Chapter, 5, details a new experimental technique, variable-angle HAADF (VA-HAADF), for achieving greater contrast and visibility in quantitative STEM by using multiple HAADF detectors in parallel, and offers experimental demonstration for the method as applied to three-dimensional dopant depth determination. As the only section that focuses solely on TEM technique development, this chapter has less overlap with any of the previous ones, which are more materials based, but presents a new avenue for future TEM advancement. The adoption of VA-HAADF may be determined

by hardware advances, but its usefulness has considerable potential far beyond dopant imaging.

Finally, I conclude this dissertation in Chapter 6 with a summary of each topic, their results, and possible future prospects.

1.4 Permissions and Attributions

1. The contents of Chapter 2 have previously appeared in Physical Review Letters, **110**, 256401 (2013) [41] and Physical Review B, **89**, 075140 (2014) [42]. It is reproduced here with the permission of the American Physical Society.

   - `http://journals.aps.org/prl/abstract/10.1103/PhysRevLett.110.256401`
   - `http://journals.aps.org/prb/abstract/10.1103/PhysRevB.89.075140`

2. The contents of Chapter 3 have previously appeared in Physical Review B, **88**, 121104(R) (2013) [43]. It is reproduced here with the permission of the American Physical Society.

   - `http://journals.aps.org/prb/abstract/10.1103/PhysRevB.88.121104`

3. The contents of Chapter 4 have previously appeared in Scientific Reports, **6**, 23652 (2016) [44]. It is distributed under a Creative Commons CC-BY license and reproduced here.

   - `http://www.nature.com/articles/srep23652`

4. The contents of Chapter 5 have previously appeared in Scientific Reports, **5**, 12419 (2015) [45]. It is distributed under a Creative Commons CC-BY license and reproduced here.

Several Figures have been adapted with permission from Ref. [46]. They are Copyrighted by the American Physical Society.

- http://www.nature.com/articles/srep12419
- http://journals.aps.org/prl/abstract/10.1103/PhysRevLett.111.266101

Chapter 2

Metal-Insulator Transitions in Rare Earth Titanates

2.1 Structure and Electronic Properties

Perovskite rare-earth titanates ($R\mathrm{TiO_3}$, where R is a rare-earth ion, including Y but not Eu) are prototypical "Mott" insulators [47, 48], with strong electron-electron interactions in the singly occupied Ti t_{2g} orbital. These materials often feature some combination of structural distortion, magnetic, orbital, or charge ordering. For example, the bulk rare-earth titanates all adopt the distorted orthorhombic $\mathrm{GdFeO_3}$ structure (space group Pbnm, see Fig. 2.1), with rotated oxygen octahedra, or Ti-O-Ti bond angles away from the ideal 180° angle in the cubic perovskite structure. These octahedral tilts and rotations are intimately coupled to the electrical and magnetic properties. Electrically, structural distortions would promote an insulating state, as the reduced Ti-O-Ti bond angle results in reduced charge transfer between neighboring Ti t_{2g} oribtals, which occur via O $2p$ orbitals, thereby reducing the Ti $3d$ bandwidth [49]. Similarly, the nature of the magnetic interaction (ferromagnetic or antiferromagnetic), magnetic ordering temperatures, and critical doping densities needed for metallic conduction are all correlated to the amount of octahedral tilt in the structure [49, 50, 9].

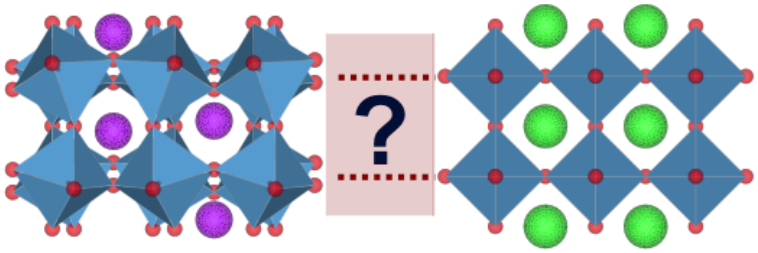

Figure 2.1: Local structure at heterointerfaces are often different than the bulk, due to interfacial connectivity requirements, which can be difficult to predict and lead to new properties.

2.1.1 Thin Film Heterostructures

Thin film heterostructures additionally modify the structure of the film, through epitaxial strain, interfacial connectivity, and reduced dimensionality effects [25, 51, 24]. Coherency strain imposed by the substrate can be accommodated by rotation of the octahedra in addition to bond length expansion/contraction [51], while corner connectivity requirements will lead to local distortions (*i.e.* rotations) at heterointerfaces, as depicted in Fig. 2.1. Electrostatic doping can also be used to modulate carrier concentrations without introducing chemical disorder, while very thin films and quantum wells offer additional methods for creating new states of matter through quantum-confinement and reduced dimensionality [27]. Thin film heterostructures therefore offer a powerful tool for *separately* controlling the contributions due to lattice distortions and electronic configurations on the properties of the film.

2.1.2 $SrTiO_3$ Quantum Wells

An example of electrostatic carrier doping can be found in the $SrTiO_3/RTiO_3$ system. $SrTiO_3$ is a prototypical perovskite at room temperature, with the ideal cubic $Pm\bar{3}m$ symmetry. It has drawn considerable interest in the past due to its incipient ferroelectricity, high tunable dielectric constant [52], and soft-mode superconductivity [53]. When inter-

faced with a $R\mathrm{TiO_3}$, a high density two-dimensional electron gas/liquid (2DEG/2DEL) is formed at the interface ($\sim 1/2$ electron per interface unit cell, or 3×10^{14} cm^{-2}), with the electrons residing in the d bands of $\mathrm{SrTiO_3}$ [54]. This sheet carrier density is due to the charge discontinuity at the interface, and is independent of the film thicknesses. In quantum wells, where a thin $\mathrm{SrTiO_3}$ layer is interfaced on both sides with a $R\mathrm{TiO_3}$, a 2DEG is formed at each interface, with the three-dimensional electron carrier density controllable by varying the $\mathrm{SrTiO_3}$ thickness.

Magnetism and signatures of electron correlation effects, including mass enhancement, have been observed in these narrow, metallic quantum wells [55, 56]. Quantum wells grown between $\mathrm{GdTiO_3}$ show an abrupt transition from a conducting to insulating state, when the average thickness of the $\mathrm{SrTiO_3}$ is reduced from 3 to 2 SrO layers, while quantum wells grown between $\mathrm{SmTiO_3}$ remain metallic all the way down to the extreme limit of a single SrO layer, as seen in Fig. 2.2 [41, 42]. This is remarkable because $\mathrm{SrTiO_3}$ is a nonmagnetic band insulator with cubic symmetry, a material that does not exhibit correlation behavior or Mott physics in the bulk. Many questions naturally arise concerning the origin of the metal-insulator transition in these quantum wells, as well as why they only occur in the quantum wells confined between $\mathrm{GdTiO_3}$, but not in those between $\mathrm{SmTiO_3}$.

Many other perovskite systems, such as $\mathrm{LaNiO_3}$ [10, 57, 58], $\mathrm{NdNiO_3}$ [59], and $\mathrm{SrVO_3}$ [60], also show metal-insulator transitions at reduced thicknesses in narrow quantum wells and thin films. For materials that undergo a metal-insulator transition in these narrow d-band electron systems, symmetry breaking of lattice, spin, or orbital degrees of freedom generally plays a crucial role in promoting the insulating state. Density functional theory (DFT) simulations of $\mathrm{SrTiO_3}$ quantum wells between $\mathrm{GdTiO_3}$ have indicated that oxygen octahedral tilts are critical in promoting a Mott insulating state in the thinnest quantum wells [61]. Therefore, key to understanding the driving force of

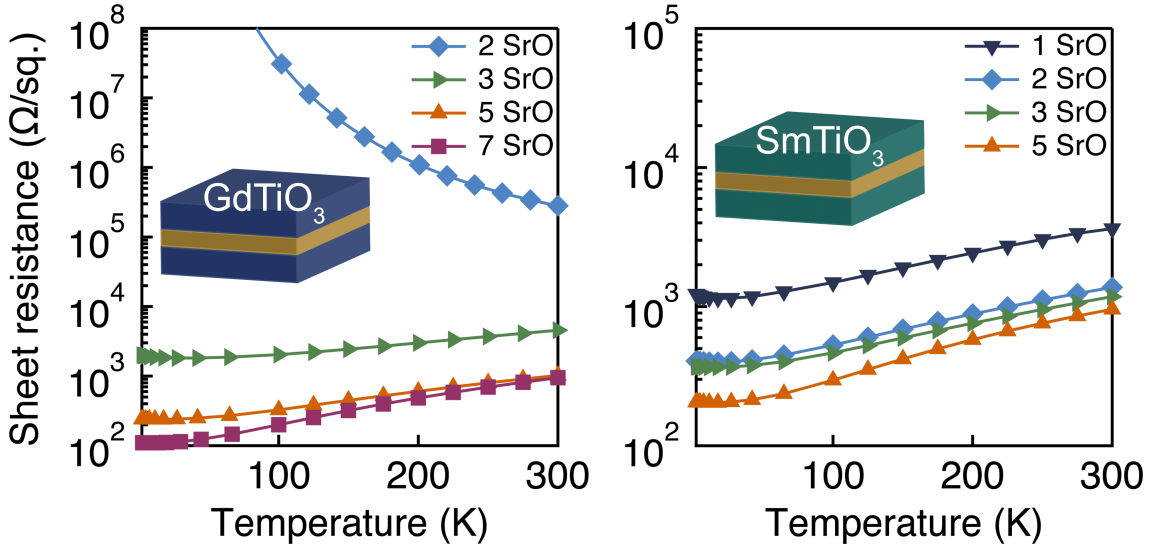

Figure 2.2: Temperature dependent sheet resistance for $GdTiO_3/SrTiO_3/GdTiO_3$ (left) and $SmTiO_3/SrTiO_3/SmTiO_3$ (right) structures as a function of $SrTiO_3$ layer thickness. A metal-insulator transition occurs in $GdTiO_3/SrTiO_3/GdTiO_3$ structures when the $SrTiO_3$ thickness is reduced to two SrO layers. Data is replotted from Ref. [42].

the metal-insulator transition in these quantum wells is determining whether structural distortions exist, and if so, how they are correlated to the the insulating state. For example, what role does interfacial oxygen connectivity requirements or electronic effects caused by the high-electron-density have on the distortion? Resolving such questions will help to separate the effects of strong electron-electron interactions vs. disorder (which can also cause localization) in these extreme-electron-density quantum wells.

To understand the relative roles of disorder, electron-electron, and electron-lattice interactions, we explore the localization behavior in thin $SrTiO_3$ quantum wells by systematically changing the external parameters of the system through choice of interfacial material, $GdTiO_3$ and $SmTiO_3$. Both RTiO$_3$s are prototypical Mott insulators in the bulk, with a d^1 electron configuration, and have the distorted orthorhombic perovskite structure (space group Pbnm [62]), with octahedral tilts described by $a^+b^-b^-$ in Glazer notation [22], although $SmTiO_3$ has slightly smaller octahedral distortions [62]. The

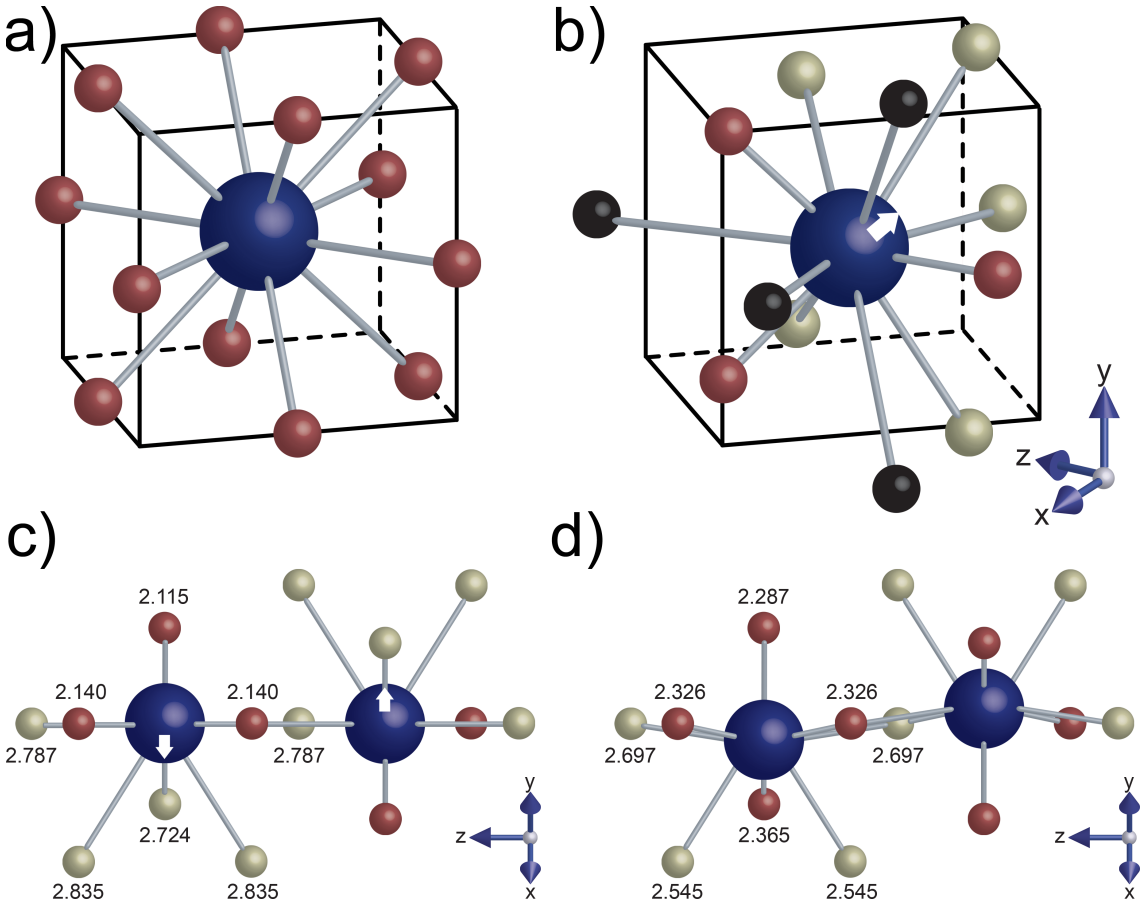

Figure 2.3: Oxygen coordination around central A-site cation, using a shifted unit cell. (a) Undistorted unit cell with 12 equal length A-O bonds. (b) Short (red), medium (yellow), and long (black) A-O bond lengths in the $a^-b^+b^+$ octahedral tilt system. The A-site cation can shift to a more favorable position along x and y (white arrow) to reduce short bonds. (c) $[110]_O$ projection of local A-site oxygen coordination, showing only short (red) and medium (yellow) bonds in the Pbnm structure without cation displacement. The A-site can shift along x and y (white arrow). Numbers indicate bond lengths in Å for bulk $GdTiO_3$. (d) $[110]_O$ projection of local A-site oxygen coordination after cation displacement, showing more equal bond lengths.

two compounds also differ in their magnetic properties: $GdTiO_3$ is ferrimagnetic while $SmTiO_3$ is antiferromagnetic at low temperatures [9]. Furthermore, the two titanates exhibit different orbital ordering, at a higher temperature than the magnetic ordering temperature: antiferro-orbital ordering in $GdTiO_3$ and ferro-orbital ordering in $SmTiO_3$ [63, 64, 65]. The orbital and magnetic properties of these systems are discussed in more detail in Chapter 3, but have important implications in the present study as they couple to the electron system in the quantum wells [55].

A key feature of the $a^+b^-b^-$ tilt system is the two degrees of freedom of the A-site cation (x and y in Pbnm), allowing it to shift to a more favorable position in order to optimize its local oxygen coordination [2, 21], as illustrated in Fig. 2.3. While direct observation of oxygen atomic positions are not yet possible by HAADF STEM, these cation displacements can be easily measured, and are directly related to the degree of oxygen octahedral tilts in bulk rare-earth titanates.

2.2 A-Site Cation Displacements

We measure the A-site cation displacements in thin $SrTiO_3$ quantum wells grown between thick layers of $GdTiO_3$ and $SmTiO_3$ using high angle annular dark field (HAADF) STEM imaging. Bulk $SrTiO_3$, which is cubic ($a^0a^0a^0$ in Glazer notation) has no A-site displacements nor octahedral tilts. Alternating layers of coherently strained $SrTiO_3$ and $GdTiO_3/SmTiO_3$ were grown on (001) $(LaAlO_3)_{0.3}(SrAl_{0.5}Ta_{0.5}O_3)_{0.7}$ (LSAT) in a multilayer structure by hybrid molecular beam epitaxy (MBE) [66, 67, 68], as shown in Figure 2.4. The $GdTiO_3/SmTiO_3$ layers had constant thicknesses of 4 nm while the $SrTiO_3$ layers varied in thickness from half a unit cell (1 SrO layer) to 4 unit cells (8 SrO layers), with a 10 nm buffer and cap on either side. The quantum wells are specified in terms of the number of SrO layers they contained, as verified by TEM. This multilayer

structure was grown specifically for the present investigation to match the quantum wells used in previous electrical studies [56] while negating any possible variability in microscope conditions from day-to-day operations.

TEM cross-section samples were prepared by focused ion beam in an FEI Helios NanoLab, with final thinning using 5 kV Ga ions, and imaged on an FEI Titan S/TEM with a field-emission source and super-twin lens (C_s = 1.2 mm) operated at 300 kV. A Fischione Model 3000 HAADF detector was used for STEM imaging while diffraction patterns were taken on a Gatan Ultrascan 1000 charge coupled device. Position averaged convergent beam electron diffraction (PACBED) [40] was used for orientation determination and precise tilt alignment. PACBED simulations were carried out using the Kirkland frozen phonon multislice simulation package [38]. A summary on PACBED formation and different simulation approaches can be found in Appendix A and B, respectively. A convergence semi-angle of 9.6 mrad was used in simulations and experiments. All HAADF images were acquired with a 1024×1024 frame size recorded at the same magnification. A dwell time of 30 μs was used to obtain a high signal-to-noise ratio while reducing the effects of drift. Centroid positions of each atomic column were extracted using a custom algorithm utilizing the MATLAB image processing toolbox [69].

2.3 TEM Characterization

Figure 2.5(a) shows the orientation relationship of orthorhombic rare-earth titanate on cubic LSAT. The preferred growth orientation, due to lower lattice mismatch, is $[110]_O//[001]_C$, where the subscript indicates the orthorhombic or cubic unit cells, respectively. Orientation variants, related by a 90° rotation about $[001]_C$, are expected [70, 68], as illustrated in Fig 2.5(a). Cross section samples imaged parallel to $\langle 100 \rangle_{LSAT}$ will contain both $[110]_O$ and $[001]_O$ projections. Figure 2.5(b) shows the bulk orthorhom-

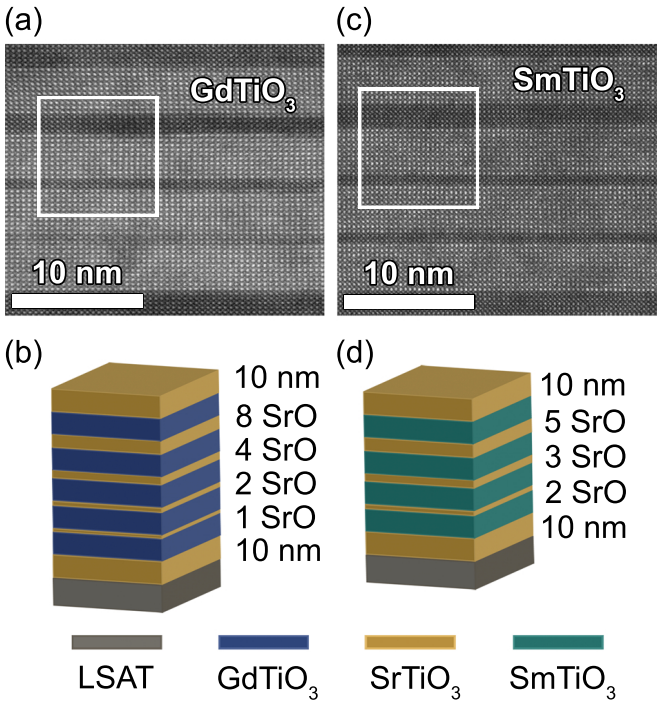

Figure 2.4: (a, c) HAADF-STEM images and (b, d) schematics of multilayer structures with $SrTiO_3$ quantum wells embedded in $GdTiO_3$ and $SmTiO_3$ layers. The brighter regions in (a, c) are $GdTiO_3$ or $SmTiO_3$ layers, respectively, while darker regions are $SrTiO_3$ layers. The labels in (b, d) indicate the thicknesses of the $SrTiO_3$ layers, measured in number of SrO planes. The $GdTiO_3$ and $SmTiO_3$ layers were 4 nm thick. Figure reproduced from [42] with permission from the American Physical Society.

bic $GdTiO_3$ unit cell viewed along the $[110]_O$ and $[001]_O$ direction, along with simulated and experimental PACBED patterns, which are visibly distinct and can be used to distinguish the two orientations. PACBED has previously been shown to be sensitive to small structural distortions [71, 72], and good agreement between the experimental and simulated PACBED patterns in Fig. 2.5(b) indicates that the $GdTiO_3$ has close to bulk-like symmetry. The average in-plane strain of coherent $GdTiO_3$ and $SmTiO_3$ films in this orientation is approximately -0.6% and -1.0%, respectively. Although films under compressive in-plane strain should be more accurately described by tilt system $a^+a^-a^-$ (monoclinic) [13], this difference lies in the precise values for the tilt angles, which are not important for this study. Therefore the structural distortion in the rare-earth titanate film will be referred in this chapter as "orthorhombic-like".

2.4 Results of Quantum Wells in $GdTiO_3$

Quantitative analysis of the A-site displacements was performed on $[110]_O$ domains, as they are most easily resolved in this projection [see Fig. 2.5(b)]. An HAADF STEM image from the superlattice containing $GdTiO_3$ is shown in Fig. 2.6(b), with magnified regions indicated by the red boxes shown in Fig. 2.6(a, c). These regions show representative sections in the 2 SrO quantum well and $GdTiO_3/SrTiO_3$ interface, respectively. From Fig. 2.6(a), we can see Sr column displacements in the 2 SrO quantum well (the red line serves as a guide for the eye), while Sr displacements in the first SrO interfacial buffer layer are absent [see Fig. 2.6(c)]. A deviation angle, 180 - θ, where θ is the angle formed between three successive A-site cations (centroid positions) is marked in Figure 2.6(c), and serves as a measure of the degree of displacement. This deviation angle is directly related to the degree of octahedra tilt, or Ti-O-Ti bond angle (for both apical and basal angles), in the bulk rare-earth titanates, as plotted in Figure 2.7, and

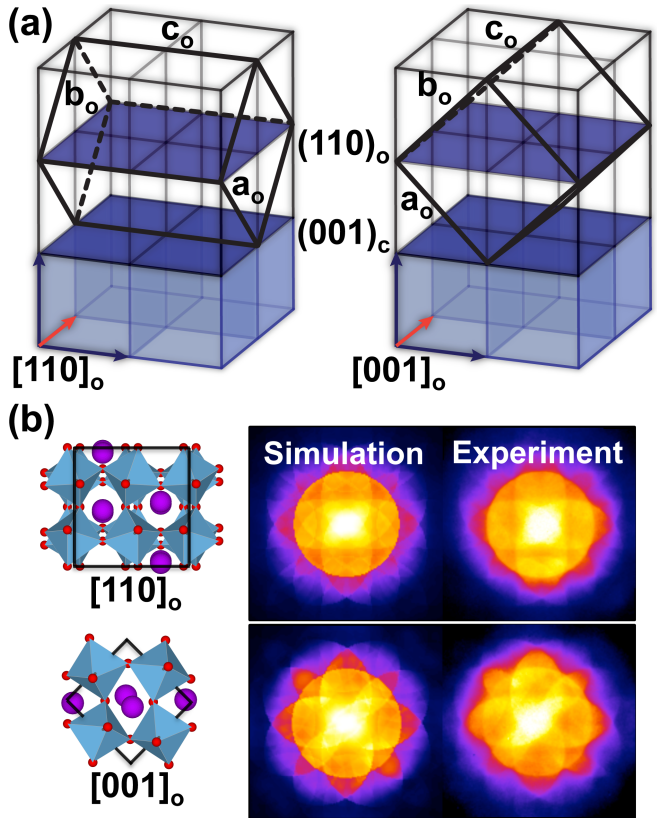

Figure 2.5: (a) Orientation relationships of orthorhombic $GdTiO_3$ cell (black outline) grown on cubic LSAT (blue). Relationship on left, $[110]_O//[001]_C$ has smaller lattice mismatch and is the preferred growth orientation. (b) Projected view of $GdTiO_3$ $[110]_O$ and $[001]_C$ structure, respectively, along with simulated and experimental PACBED patterns. Figure reproduced from Ref. [41] with permission from the American Physical Society.

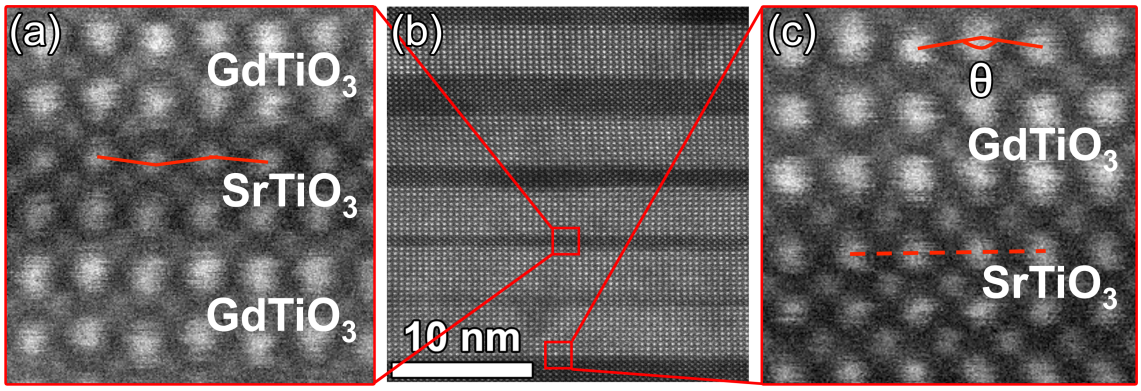

Figure 2.6: (a) Magnified region of 1 u.c. $SrTiO_3$ between $GdTiO_3$ layers shows cation displacements of Sr columns. Red line drawn to aid visualization. (b) HAADF STEM cross section showing the overall structure of the sample. Bright layers correspond to $GdTiO_3$ due to the larger atomic number of Gd. (c) Magnified region at the first $SrTiO_3/GdTiO_3$ interface showing Gd displacements along the growth direction in alternating columns. θ represents the angle between three successive A-site cations. First row of SrO in the buffer layer does not show Sr displacements. Figure reproduced from Ref. [41] with permission from the American Physical Society.

serves as an indirect measurement of the octahedral rotations in the film.

Figure 2.8 shows the deviation angle for each AO layer, where A represents the A-site cation, obtained by averaging over 18 separate images. Shaded (blue) regions in the figure represent $GdTiO_3$ layers, and are easily identified by higher intensities in the HAADF images. The left and rightmost $SrTiO_3$ regions in Figure 2.8 correspond to the 10 nm $SrTiO_3$ cap and buffer, respectively, and serve as a reference and estimate of the systematic error of the deviation angle measurement. The deviation angle in these layers is not quite zero, as expected for an undistorted cubic perovskite, but close to 1.5°, due to a combination of scan distortions, sample drift, and any system noise that may alter the atomic centroid positions from a perfect line. This same value is measured even in unstrained $SrTiO_3$ substrates and films.

It can be seen from Figure 2.8 that while the 8 SrO and 4 SrO layers show bulk-like displacements, the thinnest quantum wells containing 1 or 2 SrO layers exhibit a much

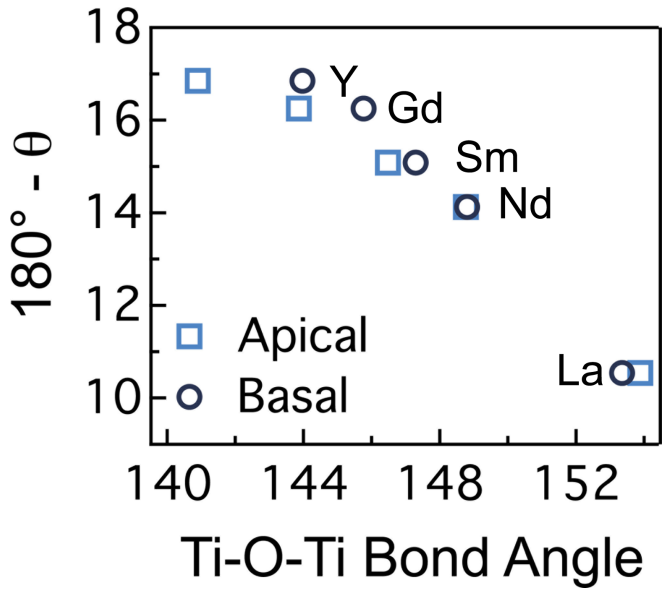

Figure 2.7: Plot of deviation angles in bulk rare-earth titanates as a function of Ti-O-Ti bond angles, showing inversely proportional relationship. Labels indicate the rare-earth A-site cation.

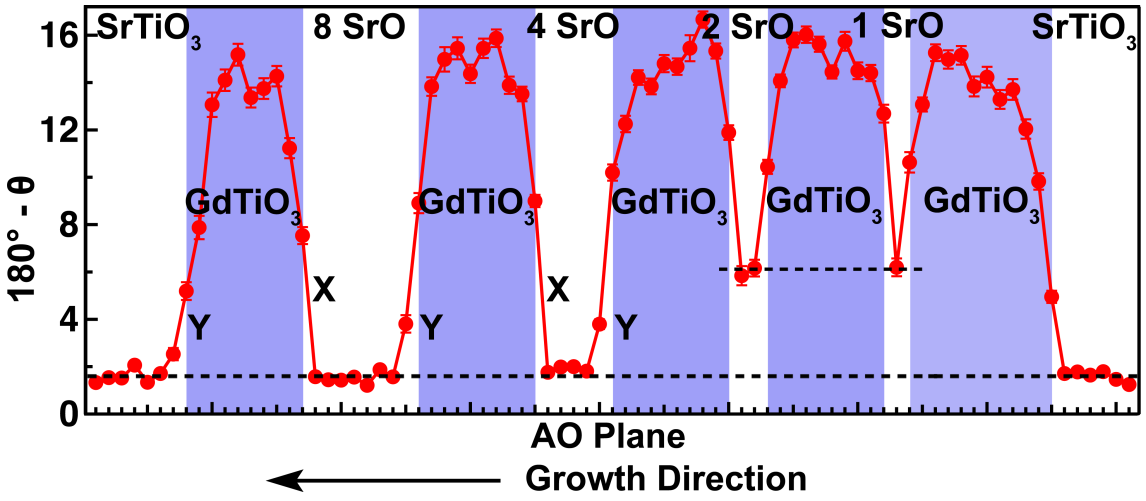

Figure 2.8: Plot of deviation angle, 180 - θ, of each A-O layer across the sample. 3 u.c. $SrTiO_3$ (4 SrO) show bulk-like angles ($\sim 1.5°$) while angles in 2 SrO and 1 SrO quantum wells show much higher angles ($\sim 6°$). Error bars represent standard error of the mean. Figure reproduced from Ref. [41] with permission from the American Physical Society.

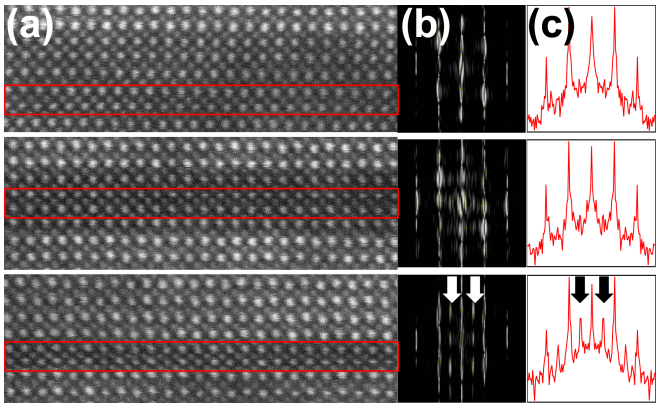

Figure 2.9: (a) HAADF STEM image of 4 u.c., 2 u.c., and 1 u.c. $SrTiO_3$ quantum wells. (b) Fourier transform of 2 SrO layers (64 x 1024 px) from each quantum well and integrated intensity profiles (c) of the FT. Extra peaks appear in the FT from the 1 u.c. quantum well, indicated by arrows, which are absent in thicker layers. Figure reproduced from Ref. [41] with permission from the American Physical Society.

larger deviation angle ($\sim 6°$). The difference in Sr column displacements can be seen in Fig. 2.6 as well as Fourier transforms (FTs) of the HAADF images. Figure 2.9 shows representative regions of the 8, 4, and 2 SrO layer quantum wells, FTs of a 64×1024 pixel region (the width of 2 SrO layers) in the center of each quantum well [Fig. 2.9(b)] and the corresponding integrated intensity profiles of each FT [Fig 2.9(c)]. Unambiguous chemical determination of each A-O layer can be made from image intensities and show clear, segregated $SrTiO_3/GdTiO_3$ layers. Extra half-order peaks are observed in the FT of the 2 SrO quantum wells (indicated by arrows), which are not present in the thicker quantum wells. These extra peaks are a result of Sr displacements parallel to the growth direction, causing a doubling of the unit cell.

As illustrated in Fig. 2.1, the need to maintain oxygen connectivity across the $SrTiO_3/GdTiO_3$ interface requires structural adjustments in either/both layers. Based on the cation displacements from Figure 2.8, this adjustment mostly occurs in the $GdTiO_3$. The measured deviation angles in the interior of the $GdTiO_3$ layers are close to those in the bulk (16.3° in the $[110]_O$ projection), while $\sim 2-3$ GdO layers adjacent to the $SrTiO_3$

show reduced cation displacements. This suggests that structurally, the octahedral tilts in the $GdTiO_3$ interface region are reduced, or the Ti-O-Ti bond angles are closer to 180°. The oxygen octahedra mismatch at the interface appears to be largely accommodated in the $GdTiO_3$, indicating "softer" bond angles in the $GdTiO_3$ than the $SrTiO_3$. The reduced octahedral tilts in the interfacial $GdTiO_3$ layers have major implications on the local magnetic properties, which will be discussed in Chapter 3.

2.4.1 Ruling out Interfacial and Strain Effects

Looking at the thinnest quantum wells, we see that the 1 SrO and 2 SrO layers show significant Sr column displacements, indicating a structural transition to an "orthorhombic-like" $a^+b^-b^-$ tilt system. While changes in the cation displacements of the interfacial GdO layers were attributed to interfacial connectivity constraints, it appears that the large displacements in the thin SrO quantum wells are not (entirely) a consequence of this effect because:

i. the GdO layers directly adjacent to the thinnest SrO quantum wells still show reduced Gd displacements, indicating that the interfacial connectivity constraints are still being largely accommodated in the $GdTiO_3$, and

ii. SrO layers in the thicker quantum wells still show bulk-like displacements, even when directly adjacent to $GdTiO_3$.

It should also be stressed that the larger deviation angle in the 2 SrO quantum well should not be attributed to interdiffusion. While interfacial roughness is likely present, the effect it would have on the deviation angle would apply equally at all other $SrTiO_3/GdTiO_3$ interfaces as well. This is clearly not the case, since as previously pointed out, SrO layers directly adjacent to $GdTiO_3$ in thicker $SrTiO_3$ films show bulk

displacements (points labelled X in Fig. 2.8). An exception can be seen in the layers where $SrTiO_3$ is grown on top of $GdTiO_3$ (points labeled Y in Fig. 2.8). These layers show a small increase in the deviation angle in the first SrO layer, due to interfacial roughness (relative to $GdTiO_3$ grown on $SrTiO_3$). This difference in interfacial roughness has been previously observed, and in general, α/β vs β/α interfaces are extremely common in epitaxy.

The larger degree of intermixing at one interface is present in certain images as an extra mixed layer (points labeled Y in Fig. 2.8), which is the reason the nominal 4 SrO layer contains five data points. However, the deviation angle in these intermixed layers are much smaller than the ones in the 2 SrO quantum wells. While MBE-grown films can be grown with atomic layer precision, the presence of surface steps and roughness results in a practical limit of ± 1 atomic layer in cross-section projections through a sample with finite thickness (20-30 nm for the samples in this study, estimated from PACBED). As a result, extra GdO layers are also present in the first $GdTiO_3$ layer on top of the $SrTiO_3$ buffer layer. These limitations in controlling one atomic layer, however, do not impact the prior analysis of cation displacements, but rather support the conclusion that the 2 SrO deviation angle is a significant measurement and not the result of interfacial disorder or connectivity effects.

Epitaxial strain can also modify film structures, and compressively strained $SrTiO_3$ is expected to become tetragonal [73], similar to the low temperature phase in the bulk. However, the tetragonal phase does not exhibit Sr displacements, and no A-site shifts are expected due to film strain. Comparing deviation angles in unstrained and compressively strained $SrTiO_3$ films (not shown here) verified that no Sr displacements are induced.

2.4.2 Relating Structure to Extreme Electron Densities

Ruling out strain and interfacial effects as the origin of the Sr displacements in the thinnest quantum wells, the observed symmetry lowering is most likely associated with the extreme electron densities as the wells are reduced in thickness. Although electrical measurements show localized behavior in the 1 and 2 SrO layer quantum wells (Fig. 2.2), Hall measurements indicate that these wells still contain the same electron density of $\sim 6 \times 10^{14}$ cm^{-2} (1 electron shared between three TiO_2 planes for the 2 SrO layer quantum well) [67, 74]. Meanwhile thicker quantum wells, which have a lower 3D electron density, are metallic. These metallic quantum wells do not have Sr displacements (which are correlated to octahedral tilts), while the thin quantum wells that are insulating show large Sr displacements (and therefore indicate the presence of octahedral tilts). The Sr displacements are indicative of a symmetry lowering distortion, most likely to an "orthorhombic-like" structure similar to bulk RTiO$_3$, and occurs precisely at the thickness for which the metal-insulator transition is observed from dc transport measurements. These parallels between the insulating quantum wells and bulk RTiO$_3$, which are Mott insulators, indicate that true "Mott" physics are occurring in the thinnest quantum wells, and that the insulating state is being driven by on-site repulsion interactions caused by the extreme electron densities.

2.4.3 Relationship to Polaronic Transport

The measured deviation angle in the 2 SrO quantum well ($\sim 6°$) is significantly smaller than that of any bulk RTiO$_3$ (LaTiO$_3$ has the smallest at 10.5°). These deviation angles are directly correlated to Ti-O-Ti bond angles, as shown in Figure 2.7 for bulk RTiO$_3$. By interpolating this empirical data with the cubic structure (0° deviation angle, 180° Ti-O-Ti bond angle), we obtain a Ti-O-Ti bond angle estimate of $\sim 160 \pm 5°$ for the 2 SrO

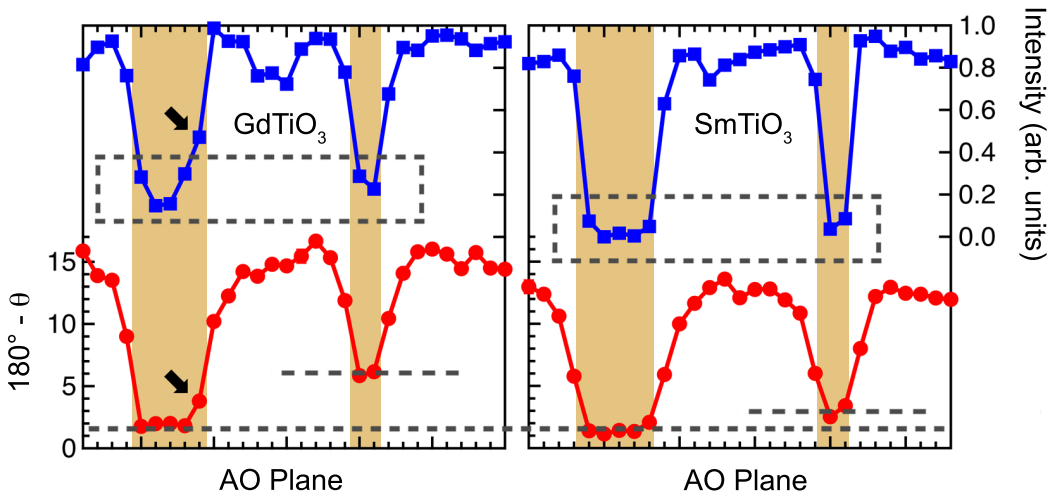

Figure 2.10: Deviation angles (red circles) in each AO plane and corresponding normalized HAADF intensities (blue squares), for regions containing two SrO and five SrO layers [indicated by the white boxes in Fig. 2.4(a, c)]. SrO layers are highlighted in gold. The dashed lines serve as guides to mark structural distortions (or lack of) in the $SrTiO_3$ wells. The dashed boxes indicate atomic planes of similar intensity. Figure reproduced from Ref. [42] with permission from the American Physical Society.

layer quantum well. In bulk $RTiO_3$, a lower activation energy for polaronic transport is associated with larger Ti-O-Ti bond angles, with $LaTiO_3$ (Ti-O-Ti bond angle of 154°) having the lowest activation energy ($\sim$ 0.025 eV) [9]. The measured activation energy of the 2 SrO quantum well is 0.02 eV [67], and consistent with the larger Ti-O-Ti bond angle.

2.5 Results of Quantum Wells in $SmTiO_3$

Deviation angles were measured in $SrTiO_3$ quantum wells embedded in $SmTiO_3$ using the same procedure as described previously for quantum wells grown between $GdTiO_3$. Figure 2.10 shows the measured deviation angles (red circles), integrated across each atomic plane, for the 2 SrO and 4/5 SrO quantum wells grown between both $GdTiO_3$

and $SmTiO_3$ [regions indicated by white boxes in Fig. 2.4(a, c)]. The data in both plots are averaged over multiple images from different regions of each sample to improve the signal-to-noise ratio and improve sampling. Corresponding HAADF image intensity profiles, where the intensity is averaged over a five pixel radius around each centroid position and averaged for each atomic plane, are plotted above the deviation angles (blue squares in Fig. 2.10). Since HAADF-STEM intensities are sensitive to atomic number (Z) differences [75, 76, 77], the pronounced atomic number contrast of the A-site cations ($Z_{Sr} = 38$, $Z_{Gd} = 64$, $Z_{Sm} = 62$) allows for straightforward identification of the atomic layers from the image intensities. The SrO planes, identified by their lower HAADF intensities in Fig. 2.4(a, c), are highlighted in yellow in Fig. 2.10.

From Figure 2.10, we can see that similar to $GdTiO_3$, the deviation angles in the interfacial $SmTiO_3$ layers show reduced deviation angles, indicating that the structural mismatch at the interface is accommodated by the RTiO$_3$. In the center of the RTiO$_3$ films, however, the deviation angles are larger, and closely match those expected from the bulk values for a coherently strained film (15.7° for $GdTiO_3$ and 14.7° for $SmTiO_3$). The smaller deviation angle in the $SmTiO_3$ interior is due to smaller octahedral rotations, and expected from the bulk structure. Similar to quantum wells grown between $GdTiO_3$, those embedded in $SmTiO_3$ show no deviations from the cubic structure for all quantum wells with thicknesses greater than 2 SrO (the apparent deviation angle of $\sim 1.5°$ is due to noise and experimental instability, as described earlier). In the 2 SrO quantum wells, however, while significant Sr displacements are observed in quantum wells embedded in $GdTiO_3$, the ones grown between $SmTiO_3$ show only a very slight increase in the deviation angle. This difference indicates that while octahedral distortions and an "orthorhombic-like" structural change is occurring in the quantum wells grown between $GdTiO_3$, those grown between $SmTiO_3$ remain close to cubic, with nearly 180° Ti-O-Ti bond angles.

2.5.1 HAADF Intensity Profiles

The HAADF intensity profiles in Fig. 2.10 provide additional insight into the degree of chemical intermixing at the $SrTiO_3/RTiO_3$ interface, and its potential effect on the measured A-site displacements. $Gd_xSr_{1-x}TiO_3$ alloys remain cubic up to Gd concentrations of $x = 0.3$ [78]; therefore large concentrations of Gd intermixing would be needed to induce an orthorhombic distortion. HAADF STEM intensity is highly sensitive to Z, so a Gd concentration of $> 30\%$ would be easily detectable in the image intensity (given the $\sim$15-20 nm sample thicknesses used here, even taking into account the contrast dependence on the dopant position along the column direction [79, 80]). A similar argument can be made for $Sm_xSr_{1-x}TiO_3$. While experimental data is not readily available, a similar doping concentration, or larger, is expected based on closer ionic radii between Sm and Sr [81, 82].

From the image intensities in Fig. 2.10 (normalized for each sample), the 2 SrO layer quantum wells show similar intensities to the 5 SrO layer quantum wells (marked by dashed boxes), indicating similar chemical composition between the two quantum wells. The intensities in the center of the 5 SrO layer quantum wells are similar to intensities from the buffer and capping layers after accounting for the TEM sample thickness (not shown), and serves as a reference for pure $SrTiO_3$ image intensities. An intermixed atomic layer in the 5 SrO quantum well between $GdTiO_3$, marked by an arrow in Fig 2.10, is clearly discernible from the HAADF intensity, and shows a small deviation angle. By contrast, the intensities from the 2 SrO layer quantum well in the same sample are *lower* than this intermixed layer (meaning it is less intermixed), yet show much *higher* deviation angles (structural distortion). These observations show that:

1. the chemical composition between the 2 SrO and 5 SrO layer quantum wells (where the metal-insulator transition occurs for those grown between $GdTiO_3$ but not

$SmTiO_3$) are similar, and therefore the detected structural differences between them cannot be attributed to a higher degree of intermixing in the thinner quantum wells.

2. the measured distortion in the 2 SrO quantum well grown between $GdTiO_3$ is significantly larger than what would be caused by disorder or intermixing at the interface.

2.5.2 DFT Calculations

Density functional theory (DFT) calculations of periodic structures similar to the experimental quantum wells was carried out by Ru Chen from the Balents group at UCSB. These calculations were carried out in the same experimentally observed orientation relationship. Simulation superlattices consisted of 2 SrO layers embedded in four layers of SmO or GdO, along with intervening Ti-O layers, e.g. $(SrTiO_3)_2(SmTiO_3)_4$. DFT calculations were performed in the WIEN2K [83] implementation using the generalized gradient approximation (GGA) [84], and used $2a \times 2a \times c$ unit cells, where a was set to the experimental LSAT lattice constant of 3.86 Å. The expanded unit cell allows for every possible tilt configuration. Structural optimization using the GGA+U approximation, as described in [61], was performed for the atomic coordinates as well as the c/a ratio. A $U_{\text{eff}} = 3.5$ eV was used on the Ti d orbitals while $U_{\text{eff}} = 8.5$ eV was used for the Gd and Sm f orbitals, where $U_{\text{eff}} = U - J$. Atomic relaxations on the superlattice were performed until the Hellmann-Feynman forces on the atoms were <5 meV/Å.

Deviation angles in the same projection were calculated from the optimized DFT structure, and compared to the experimental results in Figure 2.11. In general, the two results are in close agreement. The DFT calculations showed that the Ti-O-Ti bond angles (not shown) in the 2 SrO layers embedded in $SmTiO_3$ are less distorted than those in $GdTiO_3$, which results in the smaller deviation angles. The main quantitative

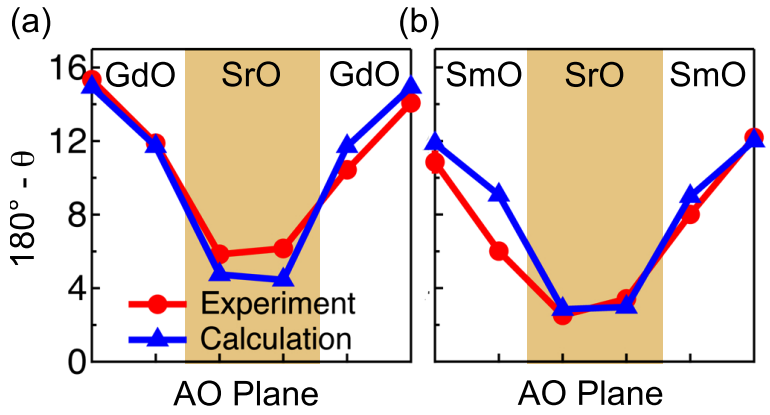

Figure 2.11: Comparison between experimental (circles) and calculated (DFT, squares) deviation angles for 2 SrO layers (shaded) between (a) $GdTiO_3$ and (b) $SmTiO_3$. Figure reproduced from Ref. [42] with permission from the American Physical Society.

difference between the DFT and experimental results are smaller calculated distortions in the quantum wells between $GdTiO_3$. This same trend occurs between bulk simulation calculations and experimental values [62]: DFT slightly underestimates the orthorhombic distortions in bulk $GdTiO_3$ and slightly overestimates the orthorhombic distortion in bulk $SmTiO_3$. The difference in Ti-O-Ti bond angles between DFT and experimental results is $< 2°$.

2.6 Correlation Physics of Perovskite Titanates

Comparing Figs. 2.2 and 2.10, we see that the thinnest $SrTiO_3$ quantum wells embedded in $GdTiO_3$ show a structural distortion, featuring (relatively) large octahedral tilts and reduced Ti-O-Ti bond angles, which precisely correlates to the onset of the metal-insulator transition in these films. Films grown between $SmTiO_3$, which show metallic behavior over all thickness ranges, are correlated with a (relative) lack of structural distortions, and Ti-O-Ti bond angles close to 180°.

Although structural disorder (*i.e.* interfacial mixing, $SrTiO_3$ thickness fluctuations)

exists in both samples (as pointed out previously), and likely plays a role in low-temperature transport measurements [56], the previous discussion on the effects of chemical disorder and the results of Figs. 2.2 and 2.10 provide evidence that true Mott-Hubbard physics is driving the metal-insulator transition. Specifically, we showed that the *abrupt transition to an insulator* by an increase in sheet resistance of several orders of magnitude, caused by a thickness change of a single SrO atomic plane, is associated with an *abrupt structural transition* that cannot be caused by disorder effects. While the TEM results show compelling evidence that large octahedral tilts and reduced Ti-O-Ti bond angles are directly correlated to the transition to an insulating state, the question remains why this only occurs in the quantum wells embedded in $GdTiO_3$, despite similar 3D electron densities in the quantum wells between both materials.

2.6.1 Polaronic Transport

From the bulk titanates, we know that small differences in octahedral distortions around a critical point can lead to large effects on the electrical properties of the material. Octahedral distortions in these systems have multiple effects: lifting the t_{2g} orbital degeneracy, decreasing the Ti-O-Ti bond angles, and reducing the Ti $3d$ bandwidth. While all bulk rare-earth titanates are insulating at all temperatures, a crossover occurs between lightly doped, insulating $SmTiO_3$ and $GdTiO_3$ from large to small polaron transport [9]. This behavior has been observed in insulating $SrTiO_3$ quantum wells in $GdTiO_3$ [74]. A high density small polaron gas is formed in those structures, which contain (relatively) large distortions, while quantum wells in $SmTiO_3$ feature much smaller distortions, and an electron gas that never localizes.

2.6.2 Interfacial Coupling

Although it appears that the Ti-O-Ti bond angles play a crucial role in promoting the insulating state in these high-electron-density quantum wells, identifying the underlying origin of the quantitative difference in the degree of the structural distortion is complicated. Mechanical considerations due to interfacial coupling serves as a natural starting point in comparing the two $R\mathrm{TiO_3}$ structures. In the bulk, $\mathrm{GdTiO_3}$ has slightly smaller Ti-O-Ti bond angles than in $\mathrm{SmTiO_3}$ (145.76° basal, 143.87° apical for $\mathrm{GdTiO_3}$ vs 147.29° basal, 146.48° apical for $\mathrm{SmTiO_3}$, see Fig. 2.7). To maintain oxygen corner connectivity (coherent bonding) at the interface, these distortions may couple to the Ti-O-Ti bond angles in the $\mathrm{SrTiO_3}$ quantum well by influencing the degree of octahedral tilt. However, as previously discussed, the data in Figs. 2.8 and 2.10 indicates that the interfacial coupling is mostly accommodated by reduced distortions in the $R\mathrm{TiO_3}$ layers. Furthermore, the difference in deviation angle between the 2 SrO layer quantum well structures ($\sim 3°$, Fig. 2.10) is significantly larger than the difference in deviation angle between the two bulk $R\mathrm{TiO_3}$ structures ($\sim 1°$, Fig. 2.7). These observations suggest that the slightly larger octahedral tilts in bulk $\mathrm{GdTiO_3}$ is not the driving force for the larger structural distortions in the embedded $\mathrm{SrTiO_3}$ quantum wells. There are additional factors promoting the larger distortions in these quantum wells, which incidentally, are also not completely captured by the DFT calculations.

2.6.3 Orbital Ordering

One possibility is strong electron correlations in the quantum wells driving orbital order which then couples to the structure. While $\mathrm{GdTiO_3}$ and $\mathrm{SmTiO_3}$ have different magnetic behavior (ferrimagnetic and antiferromagnetic, respectively), and associated orbital ordering, the magnetic ordering temperatures occur at much lower temperatures

($\sim$ 32 K and 45 K, respectively [9]) to be able to affect the room temperature structure (for more discussion on magnetic ordering and orbital ordering, see Ch. 3). According to Takubo, however, a crossover temperature significantly above the Neél temperature exists in $SmTiO_3$, where the antiferro-orbital order changes to ferro-orbital order [63], which does not occur for $GdTiO_3$. It is possible then, that coupling with the antiferro-orbital ordering in $GdTiO_3$ favors a more structurally distorted state in the $SrTiO_3$ quantum wells. This example highlights the strong interplay between spin and orbital fluctuations with the lattice, a characteristic feature in correlated perovskite oxides. The crossover temperature occurs below room temperature in bulk $SmTiO_3$, but it could potentially be shifted to higher temperatures due to epitaxial strain in thin films. While the question of whether orbital ordering occurs above the magnetic ordering temperature is still under debate [85], the results in this chapter support a view of strong electron correlations in the $SrTiO_3$ quantum wells driving the structural distortion, at least to a certain degree.

2.7 Conclusions

In summary, we have shown using HAADF STEM that high-electron-density $SrTiO_3$ quantum wells undergo a metal-insulator transition below a critical thickness only if "orthorhombic-like" distortions are sufficiently large. This metal-insulator transition is associated with a symmetry-lowering structural distortion, and appears to be driven by the strong correlations in the extreme-electron-density quantum wells. These results indicate that the transition is an intrinsic phenomena, with Mott-Hubbard physics playing a leading part and disorder contributing at most a secondary role. Specifically, even a single SrO layer embedded in $SmTiO_3$, the most "disordered" possible quantum well, remains metallic. The degree of the distortion can be controlled by the choice of interfacing $RTiO_3$, but cannot be predicted from simple geometric lattice considerations, suggesting

that more complex underlying physics (*e.g.* strong electron correlation and orbital order) are influencing the structure in the quantum wells.

Chapter 3

Magnetism in $GdTiO_3$

From Chapter 2, we observed that at $GdTiO_3/SrTiO_3$ interfaces, approximately 1-3 GdO planes at the interface showed a significant reduction in Gd displacements, which are correlated with octahedral tilts, while the interior of the $GdTiO_3$ showed displacements in good agreement with bulk values. Thus the need to maintain oxygen octahedral connectivity at the interface due to structural dissimilarity (see Fig. 2.1) is accommodated by the $GdTiO_3$. This suggests that by controlling the thickness of a $GdTiO_3$ film grown between $SrTiO_3$, we can modify the octahedral tilts in the entire $GdTiO_3$ film, which is likely to impact the magnetic properties of the film, since those are closely tied to the octahedral tilts. In this chapter, we study the "inverse" structures from Chapter 2, thin orthorhombic $GdTiO_3$ grown between cubic $SrTiO_3$. Using the same TEM characterization techniques that were described previously, along with magnetization measurements, we relate the atomic structure of confined $GdTiO_3$ to its magnetic properties.

3.1 Magnetism and Orbital Ordering

The rare-earth titanates ($R\mathrm{TiO_3}$) are strongly correlated Mott insulators, and adopt the orthorhombic $GdFeO_3$ structure (space group Pbnm, see Fig. 2.5) in the bulk, which removes the t_{2g}^1 orbital degeneracy [50, 85, 86]. The $GdFeO_3$ structure is common in

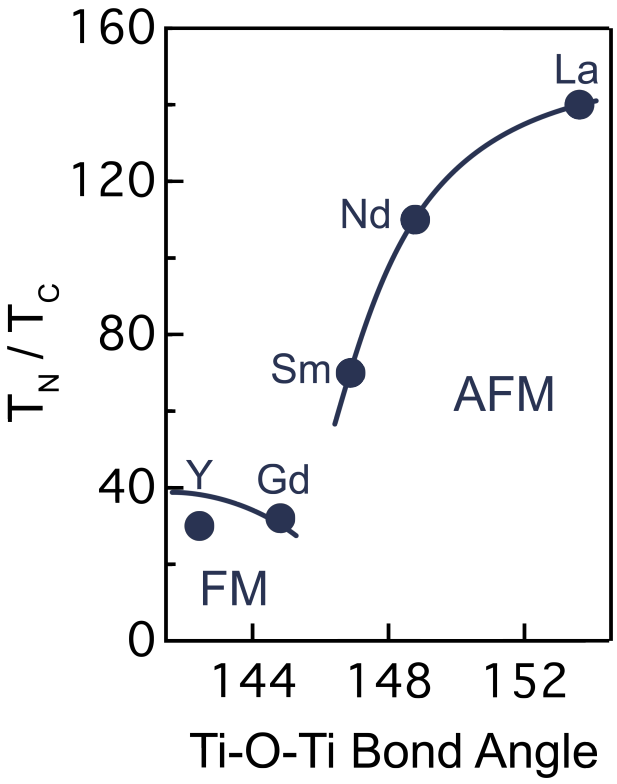

Figure 3.1: Magnetic ordering temperatures [9] as a function of Ti-O-Ti bond angles [62] in bulk rare-earth titanates. Rare-earth ion is indicated next to each data point. Ferromagnetic (FM) and antiferromagnetic (AFM) regimes are indicated below the respective Curie/Néel temperatures. Lines are drawn as an aid to the eye, indicating the general trend in bulk $R\mathrm{TiO}_3$.

perovskites, and feature the $a^+b^-b^-$ octahedral tilt system in Glazer notation [22]. The degree of the $GdFeO_3$-type distortion affects the Ti-O-Ti bond angles, which is intimately linked with the magnetic ordering in $R\mathrm{TiO}_3$. In the bulk, the Ti-O-Ti bond angle can be systematically varied by choice of rare-earth ion, and appears to be a primary factor in determining the magnetic ground state and ordering temperature [50, 86, 62, 9], as shown in Figure 3.1. A change of the Ti spin states from ferromagnetic (FM) to G-type antiferromagnetic (AFM) occurs between R = Sm and Gd.

Two distinct types of orbital ordering have been reported in the titanates, as shown in Figure 3.2, and are both compatible with Pbnm symmetry. Antiferro-oribtal ordering [Fig 3.2(a)] involves the alternate occupation of $\alpha \mid d_{xy}\rangle + \beta \mid d_{yz}\rangle$ and $\alpha \mid d_{xy}\rangle + \beta \mid d_{zx}\rangle$ orbitals in the ab plane of the orthorhombic structure, and is associated with the ferromagnetic titanates (those with larger octahedral rotations). Ferro-orbital ordering [Fig 3.2(b)] involves the occupation of $(\mid d_{xy}\rangle + \mid d_{yz}\rangle + \mid d_{zx}\rangle)/\sqrt{3}$ orbitals, and is found in the antiferromagnetic titanates (those with smaller octahedral rotations) [63]. Both types of orbital polarization also contain small lattice distortions of the TiO_6 octahedra (marked by arrows in Fig 3.2): long and short Ti-O bonds for antiferro-orbital ordering and a trigonal distortion with long and short O-O bonds for ferro-orbital ordering. While the magnetic behavior and orbital ordering seems strongly linked to the $GdFeO_3$-type distortion, the relative roles of the orbital-lattice coupling and structural distortions in determining the FM to AFM threshold is still under significant debate [63, 62, 87, 88].

3.2 Controlling Octahedral Tilts

Thin film heterostructures allow for precise ways of tuning octahedral rotations and distortions, using epitaxial strain mismatch and oxygen interfacial coherency constraints, without introducing disorder from chemical substitution [24, 72]. In that regard, they

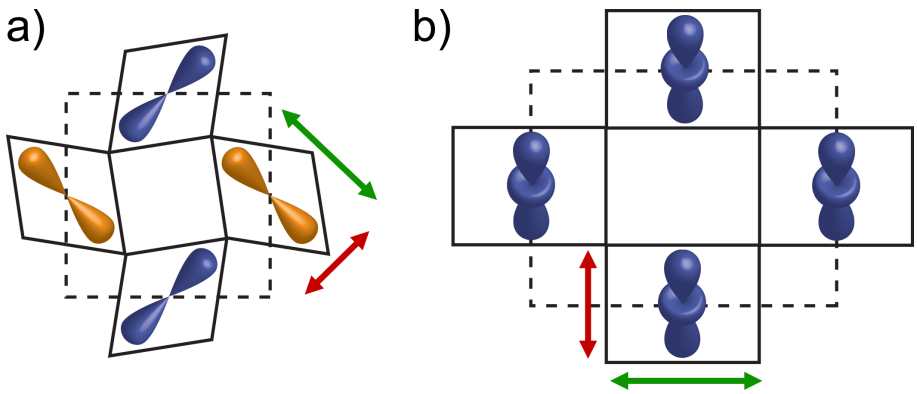

Figure 3.2: (a) Antiferro-orbital ordering for ferromagnetic ground state, showing alternate occupation of $\alpha \mid d_{xy}\rangle + \beta \mid d_{yz}\rangle$ and $\alpha \mid d_{xy}\rangle + \beta \mid d_{zx}\rangle$ orbitals. The d_{xy} orbitals are omitted for clarity. (b) Ferro-orbital ordering for antiferromagnetic ground state, showing occupation of $(\mid d_{xy}\rangle + \mid d_{yz}\rangle + \mid d_{zx}\rangle)/\sqrt{3}$ orbitals.

present distinct advantages for studying the orbital-lattice coupling, their effects on the magnetic ground state, and offer new insights into the underlying materials physics not possible with bulk studies.

It was shown in Chapter 2 that octahedral tilts in interfacial layers of $GdTiO_3$ are reduced by interfacing with cubic $SrTiO_3$. To study how these octahedral tilts are modified as a function of film thickness, $GdTiO_3$ films and $GdTiO_3/SrTiO_3$ superlattices were grown on (001) $(La_{0.3}Sr_{0.7})(Al_{0.65}Ta_{0.35})O_3$ (LSAT) by hybrid molecular beam epitaxy (MBE) [68, 66]. A 20 nm film of $GdTiO_3$ was grown directly on LSAT to represent the bulk structure. Superlattices containing 3.5 (10 GdO layers), 2.4 (7 GdO layers), and 2.0 (6 GdO layers) nm of $GdTiO_3$ between 5 nm of $SrTiO_3$ spacers were also grown on LSAT, and contained either five or ten $GdTiO_3$ layers to achieve approximately the same volume amount of $GdTiO_3$ as the 20 nm sample. While MBE provides atomic level thickness control on the single monolayer level, substrate miscut and surface steps are always present, and cause uncertainties in the layer thickness of $\sim \pm 1$ atomic plane in the growth direction. All thicknesses given here represent the average number of atomic planes, as verified by TEM, and only regions containing GdO layers with the nominal

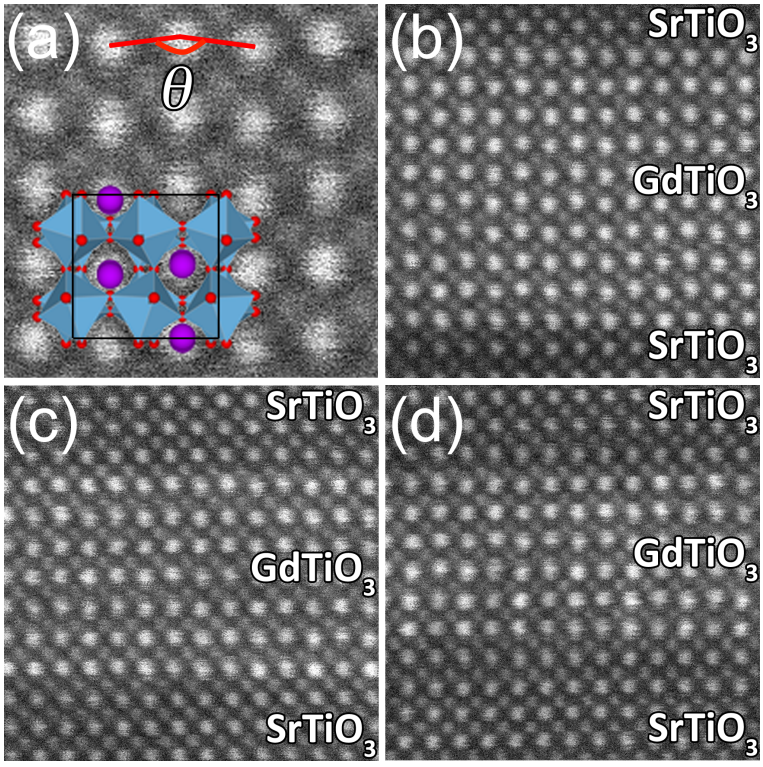

Figure 3.3: (a) HAADF-STEM image of a 20 nm $GdTiO_3$ film showing Gd displacements. The angle θ is measured between three successive Gd columns. A schematic of the bulk unit cell is superimposed. (b)-(d) Representative images of 3.5, 2.4, and 2.0 nm thick films. Figure reproduced from Ref. [43] with permission from the American Physical Society.

thickness were selected for further analysis. All superlattice samples also had 10 nm of $SrTiO_3$ as a buffer and cap layer.

3.3 TEM Characterization

TEM cross sections were prepared by focused ion beam (final thinning using 5 kV Ga ions) and imaged on a field-emission FEI Titan S/TEM with a super-twin lens (C_s = 1.2 mm) at 300 kV. Images were acquired using a 1024 × 1024 frame size and 30 μs dwell. The convergence angle was 9.6 mrad. Orientation domains in $GdTiO_3$ films are present

due to the lattice mismatch and preferred growth direction on LSAT (see Fig. 2.5) [68]. For this study, all images were taken along $[110]_O$, since this is the orientation that can best distinguish the A-site displacements.

Figure 3.3 shows representative HAADF STEM images of each $GdTiO_3$ film. A deviation angle, 180 - θ, where θ is the angle between three successive A-site cations, is indicated in Fig. 3.3(a) for the 20 nm thick $GdTiO_3$ sample. A schematic unit cell of $GdTiO_3$ is also overlaid in Fig. 3.3(a), showing the alternating displacement of the A-site cations along the growth direction. The A-site positions were quantitatively determined by extracting the centroid positions from multiple HAADF images using a custom MATLAB algorithm.

Figure 3.4 shows the deviation angles, averaged along each AO plane (where A is the A-site cation) in the growth direction, for each $GdTiO_3$ sample of different thickness. The shaded regions indicate the $GdTiO_3$ layers, which can be easily identified by the HAADF image intensities. The deviation angle of the 20 nm $GdTiO_3$ film, $\sim 15^\circ$, is averaged over four images ($\sim$ 100 atomic rows) and represented by the dashed line. This value is similar to that of bulk $GdTiO_3$ and serves as a reference for bulk-like strained $GdTiO_3$. As discussed in Chapter 2, SrO planes show no Sr displacements, since $SrTiO_3$ is cubic, so the apparent deviation angle ($\sim 1^\circ$) is due to experimental noise and instability, and serves as a measure of the error.

From Fig. 3.4, approximately one to three GdO planes at the $SrTiO_3$ interface show reduced deviation angles in all samples, as expected from the results of Chapter 2. More surprisingly, each of the $GdTiO_3$ quantum wells (3.5, 2.4 and 2.0 nm) also showed reduced deviation angles *in the films' interior*, not just at the interface. The 3.5 and 2.4 nm films both show a constant deviation angle at the center: a slightly reduced deviation angle from the bulk ($\sim 14^\circ$) for the 3.5 nm film, and a significantly reduced value ($\sim 11^\circ$) for the 2.4 nm film. The 2.0 nm film (six GdO layers) has a maximum deviation angle

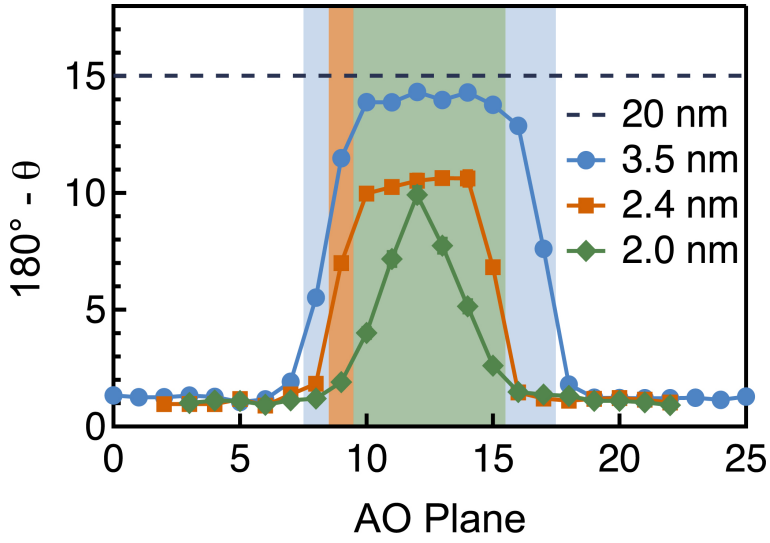

Figure 3.4: Deviation angles for each AO plane across $SrTiO_3/GdTiO_3/SrTiO_3$ interfaces with different $GdTiO_3$ thicknesses. The angle for the 20 nm film is indicated by the dashed line and is an average over $\sim$ 100 GdO planes. Shaded regions indicate the extent of the $GdTiO_3$ film for each sample, determined from the HAADF image intensities. Figure reproduced from Ref. [43] with permission from the American Physical Society.

of $\sim 10°$ in the central GdO layer, but has continuously decreasing angles toward the interface.

3.4 PACBED

To confirm that the Gd displacements in the $GdTiO_3$ quantum wells correlate with octahedral tilts, as they do in the bulk (see Fig. 2.7), position averaged convergent beam electron diffraction (PACBED) was done on the $GdTiO_3$ films. An overview of how PACBED patterns are formed is given in Appendix A. PACBED has been used previously to determine small structural distortions, including octahedral tilts in the nickelates [72, 40, 71]. PACBED simulations were carried out for $[110]_O$ $GdTiO_3$ structures with varying degrees of octahedral tilts and Gd displacements using the Kirkland multislice code [38]. An overview of simulation methods can be found in Appendix B. For more

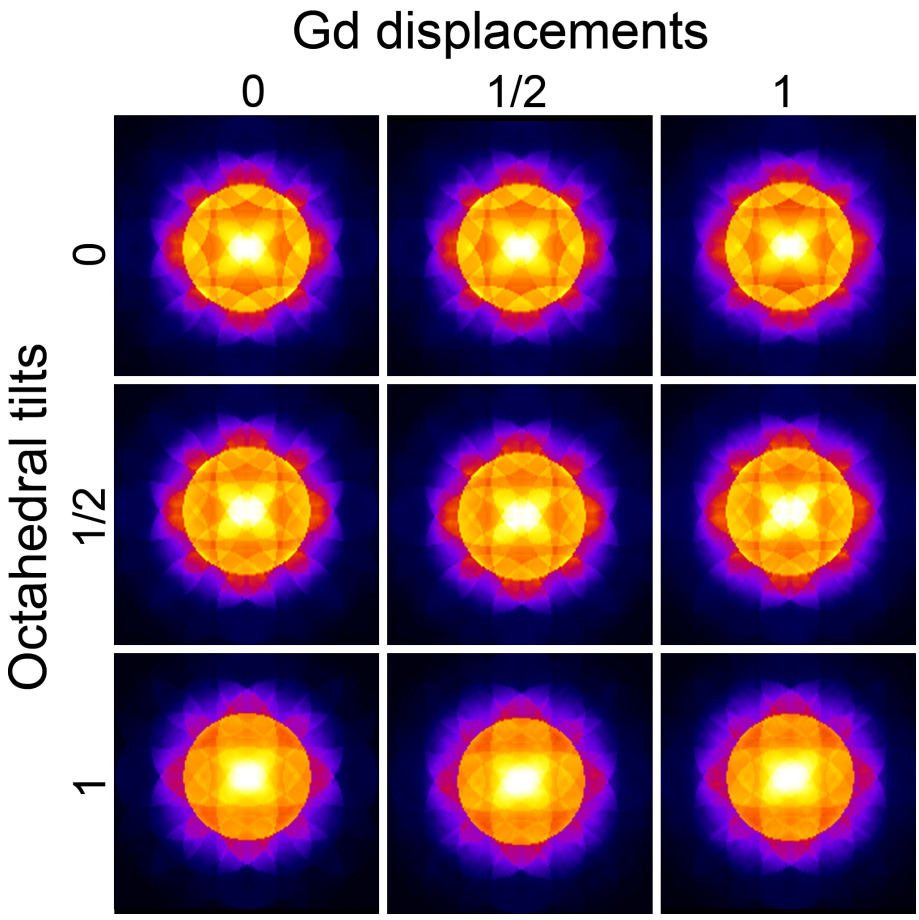

Figure 3.5: Simulated "$GdTiO_3$" PACBED patterns for different Gd displacements and octahedral tilts (TEM foil thickness is 18.8 nm). The numbers indicate the degree of distortion, with 0 signifying no distortion, 1 the distortion in $GdTiO_3$, and 1/2 corresponding to the intermediate distortion. The top-left panel corresponds to the cubic structure, while the bottom-right panel is bulk $GdTiO_3$. Figure reproduced from Ref. [43] with permission from the American Physical Society.

details on the PACBED procedure, including difficulties and subtleties in generating the structures, see Appendix C.

Figure 3.5 shows these simulations using structures containing a combination of no distortion (indicated by 0), bulk-like distortion (indicated by 1), or an intermediate degree of distortion (indicated by 1/2). From the symmetry and features of the simulated PACBED patterns, we see that in this orientation, the patterns are more sensitive to the octahedral tilts (columns), while the effects of the Gd displacements are minor (rows). Patterns without octahedral tilts (top row) contain a dark concave octagonal shape in the central disk, with four "cross-shaped" regions at the corners. Meanwhile, patterns with bulk-like octahedral tilts (bottom row) appear squarer, with a "lens-like" or "football-shaped" feature in the center, and triangular corners instead of crosses. These features are consistent regardless of Gd displacements (columns), indicating that PACBED can be used for *separate* characterization of octahedral tilts vs Gd displacements.

Experimental PACBED patterns were acquired from the central regions of each $GdTiO_3$ film, from an area of approximately four pseudocubic unit cells [slightly larger than the primitive orthorhombic unit cell in the $[110]_O$ projection, see Fig. 2.5(b)]. Figure 3.6 compares the simulated and experimental PACBED patterns from the different thickness $GdTiO_3$ films and $SrTiO_3$. For the simulations, the octahedral tilts were varied, with the degree of tilt based on the measured deviation angles for that particular film (Fig. 3.4), and interpolated to tilt angles from bulk rare-earth data (Fig. 2.7). Bulk Gd displacements were used for all $GdTiO_3$ simulated patterns, since it has little effect on the features in the $[110]_O$ projection (Fig. 3.5). The top halves of each simulated pattern is convolved with a Gaussian function, to account for the experimental point spread function, and show good qualitative agreement with the experimental pattern. From Fig. 3.6, as the $GdTiO_3$ film becomes thinner (smaller deviation angles and hence less octahedral tilts), the PACBED pattern becomes more "$SrTiO_3$-like" (i.e. cubic).

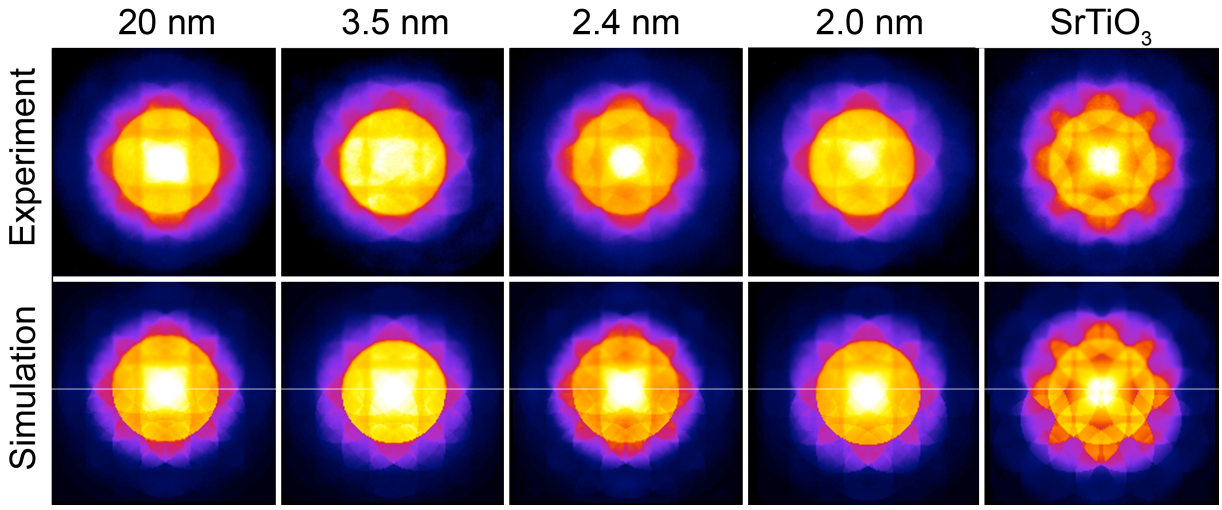

Figure 3.6: Experimental (top row) and simulated (bottom row) PACBED patterns of $GdTiO_3$ and $SrTiO_3$. The thickness labels indicate the $GdTiO_3$ layer thickness from which the experimental data was acquired. Simulated patterns use the expected octahedral tilts from measured deviation angles. Gd displacements were taken to be bulk-like for all $GdTiO_3$ simulations. The top half of simulated patterns include Gaussian convolution to account for detector point spread function, and show a better match to experimental patterns. Figure partially reproduced from Ref. [43] with permission from the American Physical Society.

This confirms that the lower deviation angles in the thinner $GdTiO_3$ films are indeed correlated with lower octahedral tilts, as expected from bulk data.

We note, that while the quantification of oxygen octahedral tilts has been accomplished in the nickelate systems using PACBED [71, 72], octahedral tilt quantification in the current structures are more challenging: different preparation techniques and sample instability leads to less than ideal surface conditions, which creates a diffuse background in the PACBED pattern, hindering quantification. The tilt system is also different, and simulations show that changes in the PACBED pattern between small differences in octahedral tilts are difficult to resolve. Excellent qualitative agreement between PACBED patterns containing different degrees of octahedral tilts and experimental patterns are obtained, however, indicating that using Gd displacements to indirectly measure octahedral tilts is valid.

3.5 Magnetic Measurements

Bulk magnetization measurements were made in a superconducting quantum interference device magnetometer (Quantum Design) with the magnetic field in the plane of the film. Figure 3.7(a) shows the magnetization for each $GdTiO_3$ sample of varying thickness as a function of temperature, under a constant field of 100 Oe. The shapes of the thicker layers (> 2.0 nm) are indicative of ferromagnetism, with the Curie temperature (T_C) marked by the arrows at the upturn in the magnetization. The T_C of the 20 nm film (~ 30 K) agrees well with that in the bulk [62, 9, 89], while thinner films show decreasing T_C until the 2.0 nm film no longer shows ferromagnetism. Figure 3.7(b) shows magnetization as a function of magnetic field, measured at 2 K. Hysteresis indicative of ferromagnetism is clearly seen in the 20, 3.5, and 2.4 nm films. The 2.0 nm film was not hysteretic, indicating the absence of ferromagnetism, and is not shown.

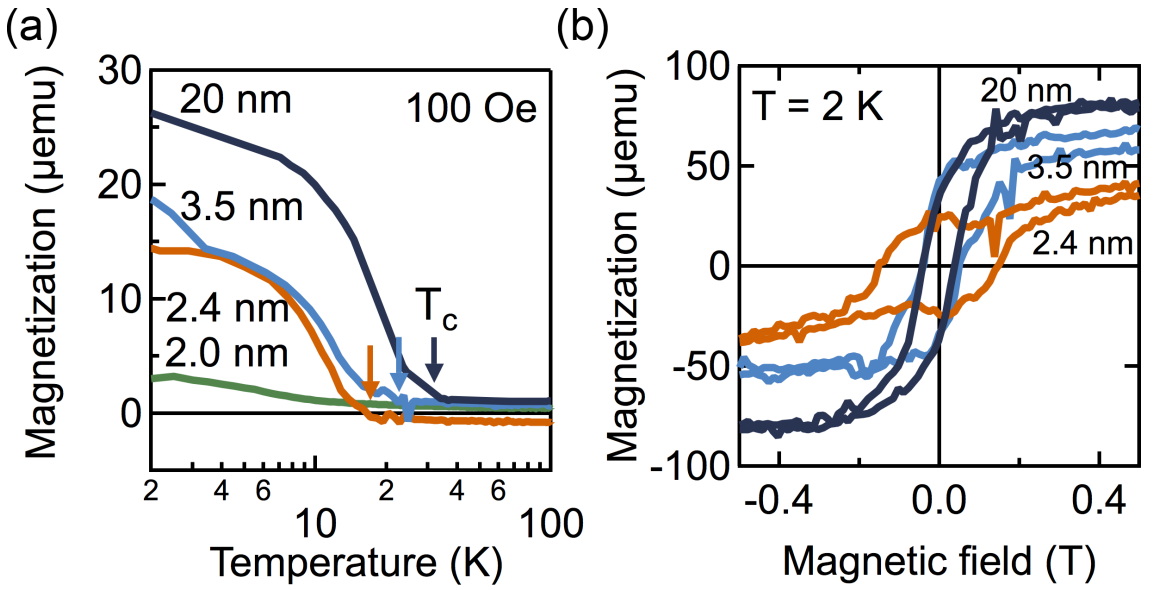

Figure 3.7: (a) Magnetization as a function of temperature for samples with $GdTiO_3$ films of various thicknesses recorded on cooling under a field of 100 Oe. The arrows indicate T_C. The data from the 20 nm sample is from Ref. [68]. (b) Magnetization as a function of magnetic field at 2 K. Figure reproduced from Ref. [43] with permission from the American Physical Society.

The magnetization measurements were from the entire sample, and includes the diamagnetic and paramagnetic signals from the LSAT substrate, the $SrTiO_3$ layers, and a Ta backing layer. Isolating the $GdTiO_3$ response was not possible due to the superlattice structure, and although all measured samples were similar in size and contained roughly the same amount by volume of $GdTiO_3$, small size and thickness variations in the substrate and backing layers are unavoidable, and thus cannot be subtracted out. Therefore, any conclusions about volume dependent parameters, such as saturation magnetization cannot be reliably made. However, the T_C and coercivity are properties of only the FM $GdTiO_3$, and independent of the sample amount.

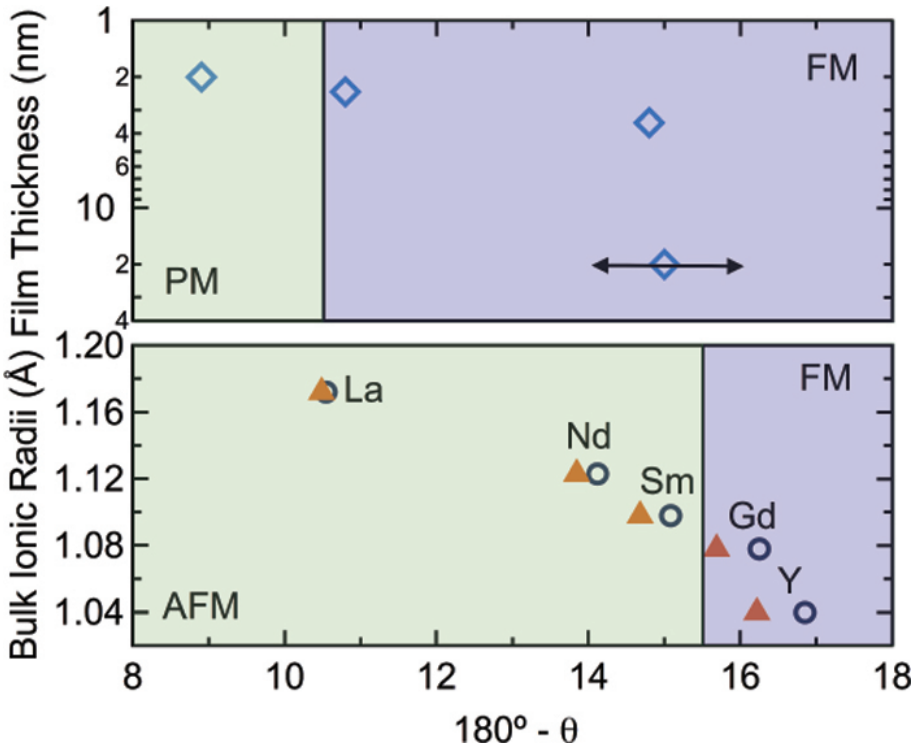

Figure 3.8: Measured deviation angles (open diamonds, top graph) for $GdTiO_3$ films with different film thicknesses. The FM stability region is indicated. The angles are an average of the center regions in the 3.5 and 2.4 nm quantum wells, and the peak value for the 2.0 nm quantum well. The arrow represents the estimated uncertainty of $\pm 1^\circ$, estimated from the $SrTiO_3$ deviation angle measurements, shown only on the 20 nm film data for clarity, but applies to all measurements. The bottom graph (open circles) shows the deviation angles for bulk rare-earth titanates [62] with different rare earth ionic radii [82]. Filled triangles estimate the effects of coherent substrate strain and microscope scan asymmetry ($\sim 2\%$ difference between x and y directions, measured from cubic samples). Both change the measured lattice parameters and, hence, deviation angles. The FM and AFM stability regions are indicated. Figure reproduced from Ref. [43] with permission from the American Physical Society.

3.6 Influence of Octahedral Tilts

Figures 3.4 and 3.7 shows that the reduction in octahedral tilts in the $GdTiO_3$ corresponds to a decrease in the T_C. This behavior is analogous to the trend in bulk RTiO$_3$, which also show a decrease in T_C as octahedral rotations are reduced (Fig. 3.1). Both systems can be understood in terms of band ferromagnetism [90], since reduced octahedral distortions (*i.e.* Ti-O-Ti bond angles closer to 180°) correspond to increasing bandwidth. A quantitative comparison between the film and bulk data, however, reveals some significant differences.

The magnetic phase diagram for $GdTiO_3$ films and the bulk RTiO$_3$s as a function of deviation angle is shown in Figure 3.8. In the bulk, the deviation angles (octahedral tilts) vary as a function of the rare-earth ion, while film thickness is used to control the distortion in the epitaxially grown samples. Circles in the bottom graph represent the measured values for single crystals [62] while triangles estimate the effect of substrate strain and the imaging distortions present in the current study. In bulk, the AFM to FM transition occurs for a deviation angle of approximately 15°, between Gd and Sm (see Fig. 3.1). In contrast, for the films, the critical deviation angle for FM to vanish occur at $\sim 10.5 \pm 1°$. The arrow in the top graph represents the estimated uncertainty (from the deviation angle measurement of cubic $SrTiO_3$), and is present for each data point. This critical angle of 10.5° is comparable to that of $LaTiO_3$, which is AFM, has the smallest octahedral tilts out of all the rare-earth titanates, and is barely insulating.

While bulk data seems to strongly suggest that the degree of the $GdFeO_3$ distortion is the main external driving force of the magnetic ordering in both pure and mixed rare-earth compounds, Fig. 3.8 indicates that the FM (and associated antiferro-orbital) ordering is not as strongly dependent on the orthorhombic distortion as previously thought. Rather, these results suggest a direct interaction between orbital ordering (which is cou-

pled to the magnetism) and the lattice, with the degree of orthorhombic distortion playing a lesser (independent) role. Reports of structural anomalies that occur at the magnetic ordering temperature [62], and orbital ordering changes in the AFM titanates at the ordering temperatue [63] also suggest a direct lattice-orbital coupling.

The FM rare-earth titanates (such as $GdTiO_3$) thus seem to be well described by narrow band, insulating, single electron models [91, 92, 93] with a FM ground state. In these systems, antiferro-orbital ordering, along with intra-atomic exchange leads to ferromagnetism below the orbital ordering temperature. The $4f^7$ electron configuration on the Gd ion ensures that there are no orbital angular momentum contributions from the Gd, suggesting that the interatomic exchange field, even at low Ti-O-Ti bond angles, favors the FM ground state.

The FM ground state vanishes in the 2.0 nm film, which is also the only film that does not contain any continuous planes with the same Gd displacements (octahedral tilts, see Fig. 3.4). The vanishing T_C in the thinnest films could be due to the structure, which makes long-range, coherent orbital ordering [87] difficult, similar to what is observed in alloys such as $La_{1-x}Y_xTiO_3$ [62] or $Sm_{1-x}Gd_xTiO_3$ [90]. These interfacial effects also offer an explanation for the so-called "magnetic dead layers," which are widely-reported in many perovskite films. If they are indeed a result of distortions from interfacial connectivity constraints, properly designed heterostructures with smaller interfacial mismatch could be used to mitigate the effect.

3.7 Conclusions and Outlook

By analyzing cation displacements in $GdTiO_3$ films grown between cubic $SrTiO_3$ using STEM, and bulk magnetization measurements, we showed that the octahedral tilts in $GdTiO_3$ can be reduced, and is concomitant with a reduction in the T_C. A FM to

non-FM transition is induced in the thinnest $GdTiO_3$ film. The FM state in the films persists to smaller deviation angles than in the bulk rare-earth titanates, indicating that the magnetic ground state is strongly controlled by the lattice-orbital coupling, and only to second order depends on the amount of $GdFeO_3$-type distortion.

Although a reduction in deviation angle is expected at the interface in $GdTiO_3$, due to oxygen connectivity requirements, an open question remains as to why deviation angles are reduced in the *interior* of films thicker than (twice) the expected interfacial thickness region. This could be due to long range structural coherency effects, or even coupling between the two high-density two-dimensional electron gases located at each interface.

The last two Chapters both demonstrate local control of octahedral tilts in perovskite oxides by proper choice of interface materials and film thicknesses. Through unique heterostructuring, new physical phenomena can be studied and controlled in ways not possible in the bulk. We hope that this work helps provide new insights into understanding complex oxide interfaces, and promotes new ways to create functional materials systems through proper materials selection and design.

Chapter 4

Metal-Insulator Transitions in Nickelates

Metal-insulator transitions (MITs) of correlated transition metal oxides have long been a central subject in condensed matter physics [49, 94]. Understanding MITs can help develop the theoretical framework for other exotic related phenomena (*i.e.* high T_C superconductivity), and controlling its behavior is key for developing useful device applications. Identifying the underlying mechanism in these transitions is often difficult however, as the many competing forces between electronic, structural and spin degrees of freedom can often compete or cooperate simultaneously. As a result, the subject continues to be a topic of strong debate, even for seemingly simple materials systems [95, 96, 97, 98, 99, 100, 101].

4.1 Origin of MIT in Nickelates

An example of such a system is the rare-earth nickelates (RNiO$_3$, where R is a trivalent rare-earth ion, except for La), a prototypical strongly correlated material which undergoes a metal-insulator transition below a certain temperature. Similar to the RTiO$_3$s, RNiO$_3$s also adopt the distorted GdFeO$_3$-type structure (space group Pbnm, see Fig. 4.1). This structural distortion is characterized by octahedral tilts in all three cartesian axes, which directly control the Ni-O-Ni bond angles. In bulk RNiO$_3$, the amount of the structural

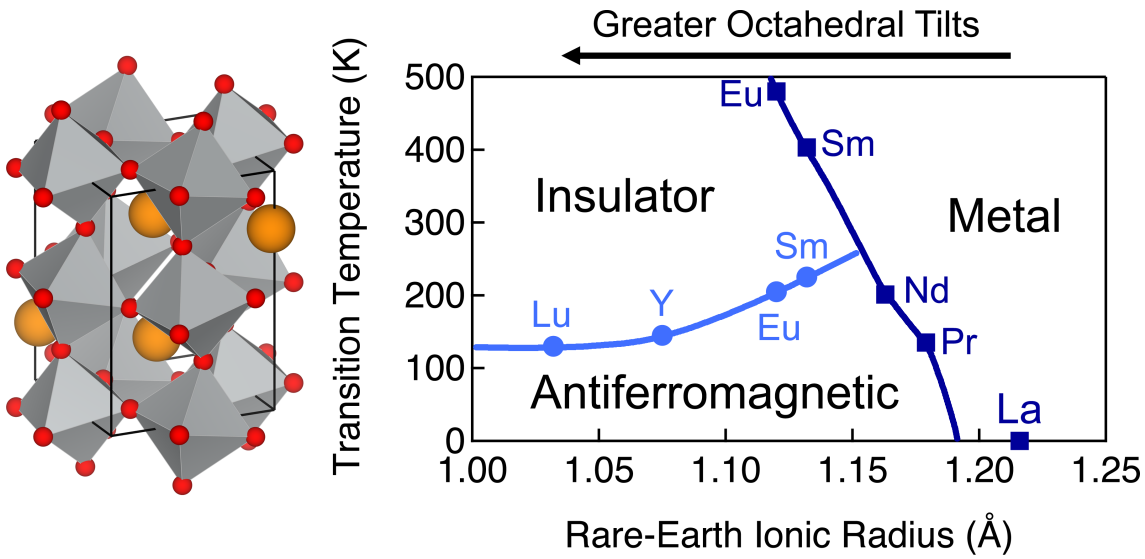

Figure 4.1: Bulk RNiO$_3$ orthorhombic structure showing octahedral tilts, which decrease the Ni-O-Ni bond angles (left). Phase diagram of bulk RNiO$_3$, showing magnetic and electrical transition temperatures as a function of rare-earth ionic radius (right). Transition temperatures from Refs. [102, 111, 112]; ionic radii from [82].

distortion is determined by the rare-earth ionic radii, with smaller radii leading to larger distortions, which increases the MIT temperature (T_{MIT}) [102], as seen in Fig. 4.1. Hydrostatic pressure [9, 103, 104] and epitaxial strain [105, 106, 107, 108, 109, 110] has also been applied in the bulk and thin films, respectively, to modify T_{MIT}. The direct correlation between the ionic radius and T_{MIT} can be strongly attributed to the Ni-O-Ni bond angles in the distorted structure, which are crucial in determining the electronic bandwidth and magnetic exchange interactions.

Early studies attributed the MIT in the RNiO$_3$s to a bandwidth-controlled charge transfer gap [102, 113]. With the larger rare-earth ions, such as Nd and Pr, magnetic ordering occurs concomitantly to form an insulating antiferromagnetic ground state [114], while for smaller ions, the magnetic ordering temperature occurs below the MIT (Fig. 4.1). Structural anomalies that occurred at the MIT were identified as a slight change in the unit cell volume, caused by a change in the Ni-O bond lengths, with no change in

lattice symmetry [102]. However, any orbital ordering that would match the magnetic wave vector, or signs of Jahn-Teller effects, the two common mechanisms for breaking the twofold degeneracy of the singly occupied e_g orbital in narrow band oxides, were not detected [114, 115, 116].

More recently, however, high-resolution measurements have revealed that the structural changes that occur at the MIT are better characterized as a structural phase transition from orthorhombic Pbnm to monoclinic P$2_1/n$ [117]. This subtle symmetry change, evidenced by signatures of two inequivalent Ni sites, points to a charge ordered (CO), or charge disproportionation (CD) ground state, and a lifting of the e_g degeneracy: $2e_g^1 \rightarrow e_g^{1-\delta} + e_g^{1+\delta}$ [118, 119, 120]. The CO ground state is also referred to as a bond-length ordered state, as it is characterized by alternating NiO_6 octahedra with different Ni-O bond lengths, since the nominal charges on the Ni sites may not vary significantly (*e.g.* $\delta \approx 0.2 - 0.3 \ll 1$ according to [117]). In the literature, the terms charge/bond order, charge/bond length disproportionation is often used interchangeably, as I do in the present Chapter. Figure 4.2 shows a schematic of the CO structure. These new findings have provided important insight into the origin of the MIT in the nickelates, and offer structural parameters for theoretical calculations. However, the relative importance of the electronic, magnetic, and structural parameters in driving the MIT remain uncertain.

4.2 Strain Effects in Thin Films

Thin films offer additional tuning parameters for controlling structure, not available in the bulk, and have been proposed as a mechanism for separating the lattice from the electronic and magnetic effects. One such example is in $LaNiO_3$, where strain has been used to alter the octahedral tilt patterns in thin films, thereby affecting its electronic structure and band degeneracy as well [32, 16].

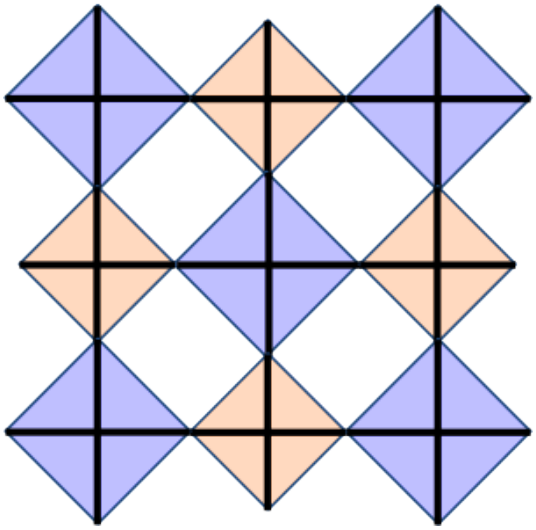

Figure 4.2: Schematic representation of the charge ordered/charge disproportionation ground state. Two inequivalent NiO_6 octahedra (colored blue and orange, respectively), have different bond lengths, which alternate between nearest neighbors.

Similarly, recent efforts have been made to utilize epitaxial constraints to controllably modify the structure of $NdNiO_3$ films in an effort to disentangle the different competing mechanisms responsible for the MIT and identify the primary factor. For example, ultrathin (15 unit cells) $NdNiO_3$ films on $NdGaO_3$ grown by Meyers et al. showed an MIT and bulk-like magnetic ordering, but x-ray absorption spectroscopy (XAS) and resonant x-ray scattering (RXS) did not detect any symmetry lowering in the structure [121]. They therefore suggested that the magnetic ordering independently drives the MIT. Upton et al. also dismiss any charge ordering/disproportionation mechanism involving symmetry changes, instead proposing Ni $3d$ and O $2p$ hybridization, as well as Ni charge redistribution to Nd $5d$ states as underlying mechanisms [122]. These results are in contrast to other experimental [120, 123, 124] and theoretical work [97, 125, 126] based on charge/bond length disproportionation on the Ni sites.

A key issue in this debate relies on the structural symmetry of the $NdNiO_3$, and the ability to detect this subtle change in strained films as they go through the MIT. The

charge disproportionation model requires a structure with two inequivalent Ni sites, such as the low temperature monoclinic phase in the bulk. This distortion in bulk $NdNiO_3$ is very small [117], and would be even more challenging to detect in ultrathin films, where the signal would be much weaker. In addition, structural information from the opposite case, *i.e.* when the MIT does *not* occur, such as in compressively strained films, could also provide insight into the microscopic reasons for the MIT.

In this Chapter, we analyze the structure of compressive and tensile strained $NdNiO_3$ thin films, grown on $YAlO_3$ and $NdGaO_3$, respectively, using position averaged convergent beam electron diffraction (PACBED) in scanning transmission electron microscopy (STEM). PACBED has been previously used to analyze extremely small structural distortions [127, 71, 72], such as octahedral tilts and ferroelectric displacements, and can be obtained from unit cell length scales. A summary of PACBED formation can be found in Appendix A. We use a liquid nitrogen cold-stage holder to obtain PACBED patterns above and below T_{MIT}. From PACBED, we show that tensile strained films (grown on $NdGaO_3$), which exhibits a MIT, undergoes a structural transition, while compressively strained films (grown on $YAlO_3$), which are metallic at all temperatures, do not. We combine these results with symmetry arguments and geometric constraints to provide a remarkably simple, yet complete picture of the MIT in these films and reasons for its suppression.

In addition to understanding the temperature-driven MIT, many other aspects of this material system, such as non-Fermi liquid phases [128, 107, 9] and tuning the Fermi surface to mimic those of the cuprate superconductors [129, 130], are strongly dependent on the interplay between structural and electronic degrees of freedom. Elucidation of the mechanisms behind the MIT in the nickelates could potentially extend to insights into these other fascinating phenomena as well.

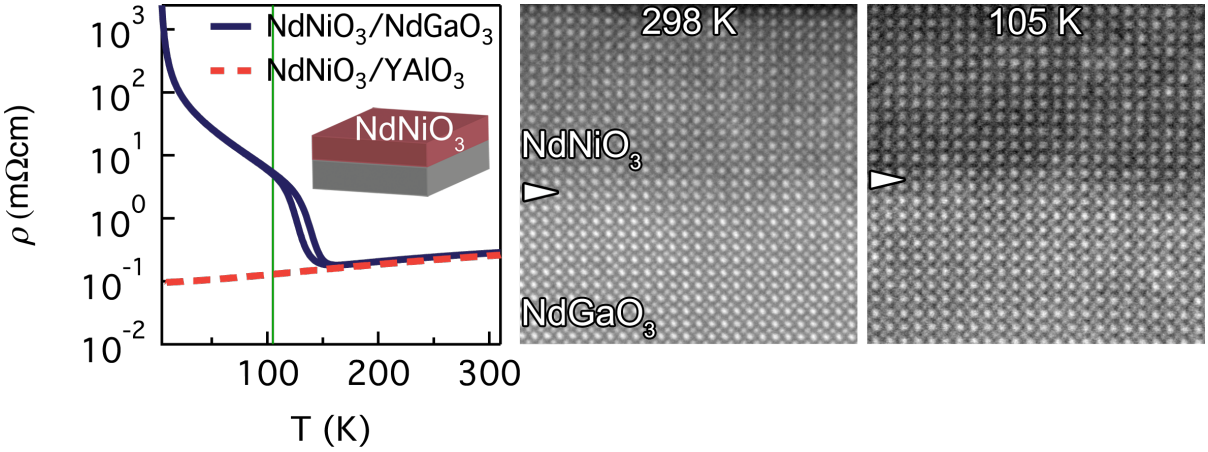

Figure 4.3: Resistivity as a function of temperature for $NdNiO_3$ films grown on $NdGaO_3$ (solid line) and $YAlO_3$ (dashed line) substrates. A MIT occurs on the $NdGaO_3$ grown film at $\sim$ 130 K. Green vertical line marks cold stage temperature ($\sim$ 105 K). Corresponding STEM images for the film grown on $NdGaO_3$ at room and cryo temperatures are shown on the right. Arrows mark the approximate interface between the film and substrate. Images were acquired using fast acquisition and cross-correlated over many frames for higher signal-to-noise.

4.3 Transport in Strained $NdNiO_3$ Thin Films

$NdNiO_3$ films were grown on $NdGaO_3$ and $YAlO_3$ substrates by RF magnetron sputtering in an Ar/O_2 gas mixture at a 9 mTorr growth pressure, as described in [105]. The films were 15 unit cells ($\sim$ 6 nm) thick, as confirmed by TEM, and fully strained to the substrate (0.85% tensile and -3.5% compressive for $NdGaO_3$ and $YAlO_3$, respectively), as verified by high-resolution x-ray diffraction. In-plane longitudinal resistivity measurements as a function of temperature were made in a Quantum Design Physical Properties Measurement System (PPMS).

Figure 4.3 shows resistivity curves of both films, along with corresponding STEM images at room and cryo temperatures for the film grown on $NdGaO_3$. The images were acquired using a high angle annular dark field (HAADF) detector with a convergence semi-angle of 9.6 mrad. The arrows in the image mark the approximate interface between the film and substrate. From the resistivity, we see that the film grown on $YAlO_3$ shows

metallic behavior across all temperatures, while an MIT is observed in the film grown on $NdGaO_3$, occurring at ~ 150 K, with a hysteresis of ~ 25 K. This T_{MIT} is consistent with other similarly reported films in the literature [121], but is lower than bulk $NdNiO_3$ (~ 200 K [111, 102]), as is typical for constrained films.

A Gatan liquid nitrogen cold stage holder is used to bring the specimen temperature to 105 K (green line in Fig. 4.3, well within the insulating regime for the film that undergoes an MIT. In the compressively strained film, grown on $YAlO_3$, we see a complete suppression of the MIT, which is consistent with other reports in the literature [106, 107, 131].

4.4 Orientation Relationships

Both substrates, $NdGaO_3$ and $YAlO_3$, are Pbnm orthorhombic perovskites with the growth direction oriented along $(110)_O$, where the subscript indicates the orthorhombic unit cell. Figure 4.4 shows the orientation relationship of the $NdNiO_3$ film on a $(110)_O$ surface, where the subscripts s and f denote the substrate and film, respectively. All directions are given in orthorhombic notation. We note that while the $(001)_O//(110)_O$ orientation has similar lattice mismatch as $(110)_O//(110)_O$, structural mismatch at the interface due to different oxygen octahedral arrangements make this orientation unlikely.

From Fig. 4.4, the film is epitaxially constrained along the ab ($[1\bar{1}0]$) and c ($[001]$) orthorhombic axes, but the a and b lattice parameters change to accomodate the strain, forming a characteristic angle, γ, that deviates from the 90° angle in the bulk. A general $2 \times 2 \times 2$ pseudocubic supercell containing the original orthorhombic unit cell is outlined in blue.

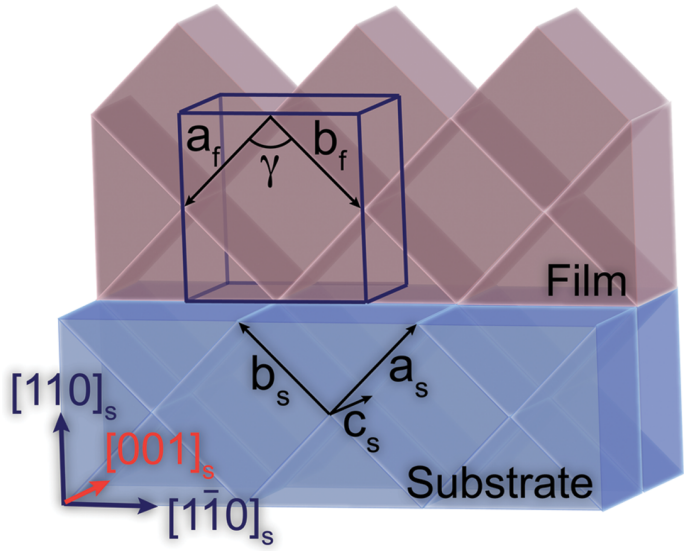

Figure 4.4: Schematic of an orthorhombic film grown on a (110) oriented orthorhombic substrate. The lattice parameters of the orthorhombic substrate are indicated by subscript "s". An expanded $2 \times 2 \times 2$ pseudocubic unit cell is marked in the film, with arrows tracing the traditional **a** and **b** orthorhombic lattice parameters, denoted by subscript "f". The angle between these two directions are denoted by γ.

4.4.1 Transmission Electron Microscopy and PACBED

Transmission Electron Microscopy (TEM) cross-sections were prepared using a focused ion beam with final milling energies of 5kV Ga ions along both the $[001]_O$ and $[1\bar{1}0]_O$ projections for each sample. A 300 kV FEI Titan S/TEM (C_s = 1.2 mm) was used for HAADF STEM imaging and PACBED acquisition, with a 9.6 mrad convergence semi-angle for high resolution imaging. Both 9.6 and a reduced 3.4 mrad angle was used for position averaged convergent beam electron diffraction (PACBED). Room temperature imaging and PACBED was done on an FEI double-tilt holder while a Gatan 636 double-tilt LN_2 holder (operating at a measured 105 K) was used for low temperature experiments. The temperature remained stable throughout the data acquisition.

PACBED patterns are similar to conventional TEM diffraction patterns, except the convergent semi-angle of the probe spreads each diffraction beam from a point to a disc.

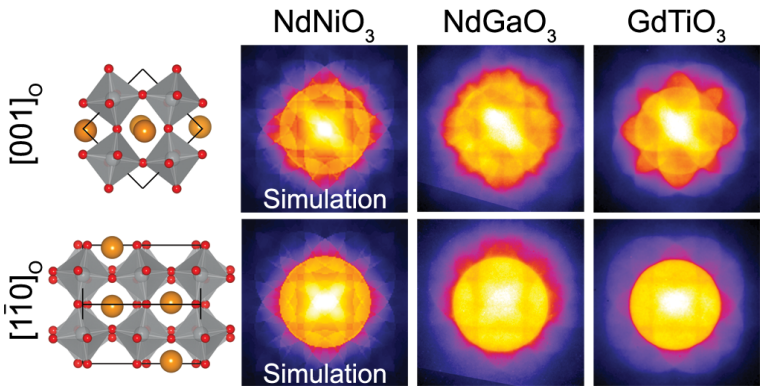

Figure 4.5: Unit cell schematic of the two cross-section views of $NdNiO_3$, along with simulated and experimental PACBED patterns of orthorhombic P*bnm* films, showing similar features.

A larger convergence angle results in a larger disc, and greater disc overlap. The data is acquired serially in STEM mode rather than in parallel, as is the case for conventional CBED. The intensities of the different diffraction discs overlap to create unique looking patterns, but the reflections still maintain the point group (or more accurately Laue group) symmetry of the structure. An artificial color table has been applied to all PACBED patterns in this work, to better highlight the intensity variations in the patterns.

PACBED of $NdNiO_3$ projected in the $[001]_O$ and $[1\bar{1}0]_O$ directions produces patterns with distinct features, similar to those previously observed in Chapters 2 and 3, for orthorhombic films grown on cubic substrates. Figure 4.5 shows PACBED patterns from the simulated $NdNiO_3$ bulk structure and experimental patterns from a $NdGaO_3$ substrate and $GdTiO_3$ film. Patterns along $[1\bar{1}0]_O$ contain a square-like feature in the central disc, while those along $[001]_O$ show a diagonal intensity stripe. These features are accurately reproduced in the simulations, and experimentally observed in other perovskite structures with the same tilt structures and space group, as seen in Fig. 4.5.

One use for the distinct PACBED patterns is simple identification of the zone axis

by visual inspection. The present study focuses on the $[001]_O$ projection (orange arrow in Fig. 4.4), since PACBED patterns from $[1\bar{1}0]_O$ did not show sensitivity to the structural changes seen in $[001]_O$. While PACBED has been used to detect small structural distortions [71, 72, 127], the overlap of large diffraction discs can hide subtle symmetry changes. Therefore, we employ low-angle PACBED (LA-PACBED) in this Chapter to reduce the size of the diffraction discs in order to better distinguish them and again additional insight into the film structure. For all LA-PACBED patterns, a film area of $\sim 12 \times 12$ unit cells was scanned. The reduction in the convergence semi-angle (9.6 to 3.4 mrad) in LA-PACBED results in a decrease in the resolution of the HAADF STEM image. However, the film and substrate could still be differentiated using the smaller convergence angle during the LA-PACBED acquisition.

4.5 $NdNiO_3$ Films Grown on $NdGaO_3$

4.5.1 Room Temperature Structure

Figure 4.6(a) shows experimental LA-PACBED patterns from the substrate and film areas of $NdGaO_3/NdNiO_3$, at room temperature, with a simulated pattern of bulk $NdNiO_3$ for comparison. The simulation was carried out using the Kirkland multislice code [38], at 0 K for speed. An overview of simulation methods are given in Appendix B. A Sobel edge filter was applied to each pattern and displayed in Fig. 4.6(b) to highlight sharp changes in the intensity and better distinguish the diffraction discs. Relevant discs are indexed in the orthorhombic notation.

In the larger angle PACBED patterns (9.6 mrad, Fig. 4.5), we noted that a characteristic diagonal intensity stripe exists in the central beam when looking down $[001]_O$. We see a similar bright band running diagonally in the LA-PACBED in Fig. 4.6 for the

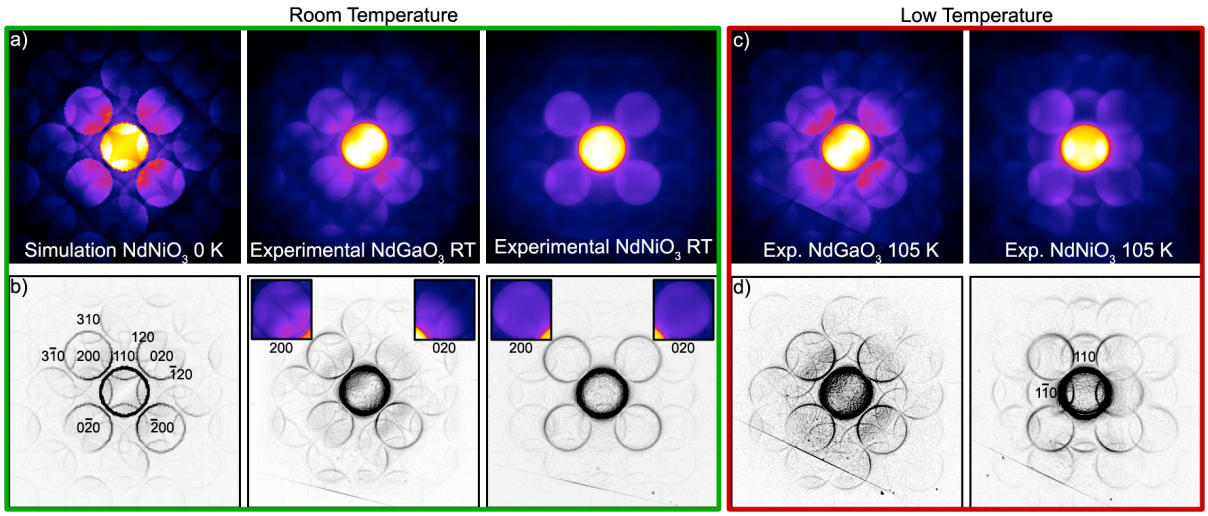

Figure 4.6: (a) Simulated LA-PACBED patterns for bulk $NdNiO_3$ ($\sim$ 23 nm), and experimental LA-PACBED patterns for the $NdGaO_3$ substrate and the $NdNiO_3$ film on $NdGaO_3$ at room temperature. (b) LA-PACBED patterns from (a) after a Sobel edge filter, with enhanced contrast to allow for identification of the diffraction discs. Selected diffraction discs are indexed in orthorhombic notation. The insets show the experimental 200 discs. The $NdGaO_3$ substrate shows very similar features and intensities as the simulation, while the $NdNiO_3$ film shows a different symmetry than the substrate and bulk structure. (c) Low temperature LA-PACBED patterns from the $NdGaO_3$ substrate and $NdNiO_3$ film. While the substrate pattern is similar to its room temperature counterpart, the low temperature film displays a different symmetry from both the room temperature film and the substrate. (d) LA-PACBED patterns from (c) after a Sobel edge filter. Asymmetry between 110 and $1\bar{1}0$ diffraction disc intensity is clearly visible.

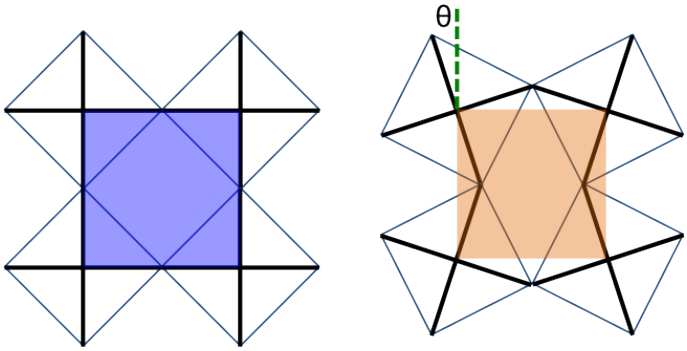

Figure 4.7: Cubic perovskite lattice (left) with TiO_6 octahedra at the corners of the unit cell. Rotating each octahedra by θ in the plane of the page (right) reduces the two in-plane lattice parameters by $\cos\theta$. Unit cells, shaded in blue (larger) and orange (smaller), respectively, have different lattice parameters.

simulated bulk $NdNiO_3$ structure, and substrate $NdGaO_3$. Furthermore, clear differences in diffraction features can be seen between 200 and 020 discs for the same patterns: a bright region of intensity can be clearly seen in 200 near the central beam, as well as overlapping 310 reflections, but are barely observable in 020. Insets of the 200 and 020 discs for the experimental patterns are highlighted in Fig. 4.6(b). These asymmetric features are caused by the octahedral rotations and A-site (Nd) cation displacements characteristic of the orthorhombic P*bnm* structure, and are a close match with the bulk $NdNiO_3$ simulation. In contrast, the LA-PACBED pattern of the $NdNiO_3$ film on $NdGaO_3$ shows similar intensity features and variation between 200 and 020, indicating that the strained film has different symmetry from the bulk structure as well as the substrate.

We can also see from Fig. 4.6(a) that the 200 and 020 disc spacing, which correspond to the a and b orthorhombic lattice parameters (see Fig. 4.4), are clearly different for the $NdGaO_3$ substrate, as expected, but are equal for the $NdNiO_3$ film (although it should be noted that bulk a and b lattice parameters of $NdNiO_3$ are almost identical as well). Equal a and b lattice parameters are expected for a tensile strained orthorhombic film [13]: as the film is constrained along $[1\bar{1}0]_O$ and $[001]_O$, the strain is accommodated by

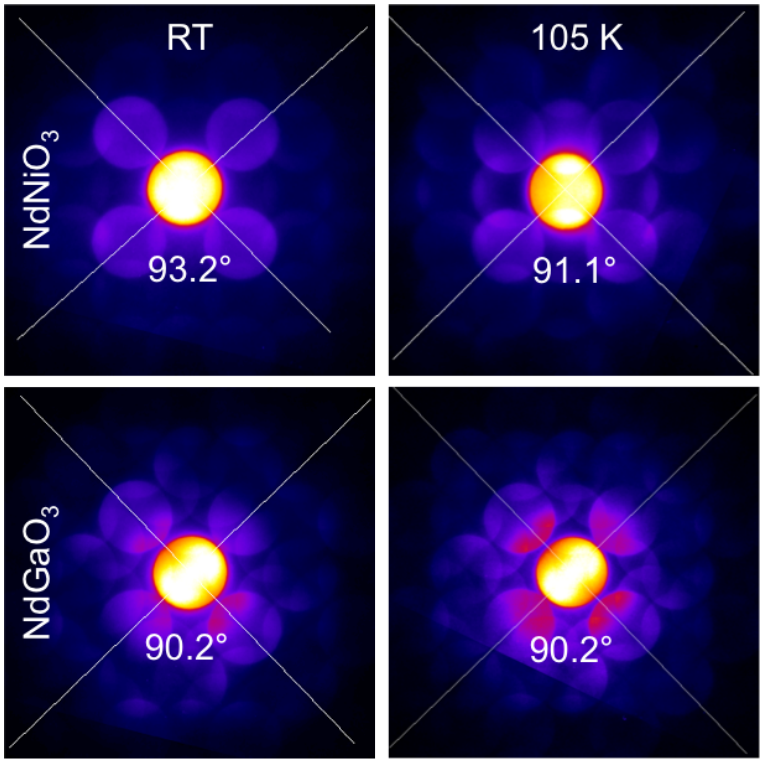

Figure 4.8: Measurement of γ in $NdNiO_3$ films on $NdGaO_3$. Large ($> 90°$) γ indicates reduced octahedral tilts along the growth direction ($[110]_s$, see Fig. 4.4). Reduced γ in $NdNiO_3$ at low temperature indicates increased rotations compared to room temperature. Measured γ in $NdGaO_3$ substrate is $\sim 90°$ for both temperatures, as expected.

an increase in γ (the angle between a and b, Fig. 4.4), and a reduction in octahedral tilts along the growth axis, $[110]_O$. The reduction in octahedral tilts is due to oxygen corner-connectivity constraints; octahedral tilts around a cartesian axis will cause a reduction in the lattice parameters perpendicular to that axis, as illustrated in Figure 4.7, or in the present case, the opposite effect will occur. We note that these structural changes occur in the film as a result of the strain state, whether the substrate is cubic or orthorhombic.

The angle γ can be accurately measured from the LA-PACBED patterns, as the center of the diffraction discs can be easily determined from the overlapping features. Figure 4.8 shows the measurement of γ from the $NdNiO_3/NdGaO_3$ diffraction patterns,

with $\gamma = 90.2°$ for the $NdGaO_3$ substrate and 93.2° for the $NdNiO_3$ film. The large increase in γ in the film indicates that the octahedral tilts about the growth direction, $[110]_O$, are either mostly or completely suppressed.

4.5.2 Low Temperature Structure

Figure 4.6(c) shows LA-PACBED patterns of the $NdNiO_3/NdGaO_3$ sample at 105 K. While the substrate pattern shows similar features as the room temperature pattern (expected since $NdGaO_3$ does not undergo a structural change at low temperatures [132], we see a noticeable change in the $NdNiO_3$ film. Most prominently, a strong asymmetry in intensity can be observed between the 110 and $1\bar{1}0$ reflections, which can be seen as bright overlaps in the central disc, especially noticeable in the edge-filtered patterns in Fig. 4.6(d). This difference in the LA-PACBED pattern indicates a reduction in film symmetry, most likely a transition to monoclinic $P2_1/n$, similar to what occurs in the bulk at low temperature. Synchrotron powder diffraction of polycrystalline $NdNiO_3$ also reports similar peak splittings between $40\bar{4}/404$ reflections as a sign of the monoclinic transition [117]. We also see from Fig. 4.8 that γ decreases to 91.1° at low temperatures in the $NdNiO_3$ film, which indicates that the octahedral rotations about the growth direction ($[110]_O$) increases, consistent with $P2_1/n$ symmetry (a three tilt system [2]).

4.6 $NdNiO_3$ Films Grown on $YAlO_3$

Figure 4.9 shows LA-PACBED patterns of the compressively strained $NdNiO_3$ film grown on $YAlO_3$. Similar compressively strained films are reported to be monoclinic ($P2_1/m$) [13]. The patterns from the substrate are similar to the $NdGaO_3$ substrate patterns at both temperatures; even though the intensities are different, due to the different scattering strength of the atoms, they possess similar symmetry elements. From the

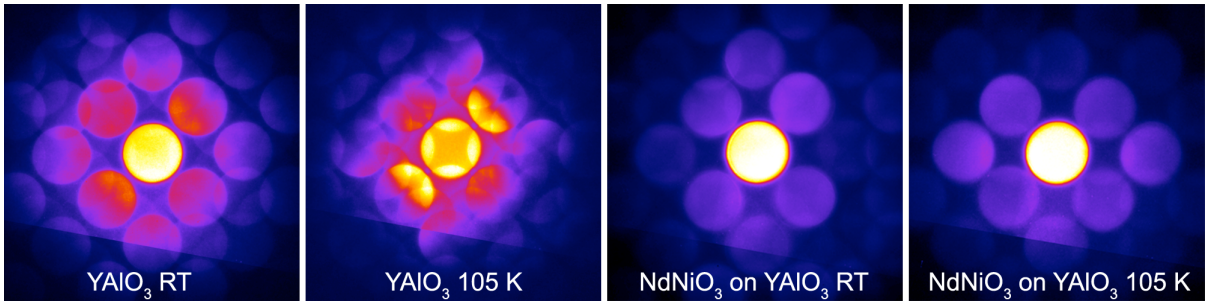

Figure 4.9: LA-PACBED patterns of substrate and film $NdNiO_3/YAlO_3$ at room temperature and at 105 K. The substrate shows similar features to the $NdGaO_3$ substrate. The film does not show any structural change at low temperature.

LA-PACBED of the $NdNiO_3$ film, we do not observe any noticeable differences between the room and low temperature patterns, although the 220 and $2\bar{2}0$ reflections (using orthorhombic indices) may have slightly different intensities.

Overall, the patterns from the film grown on $YAlO_3$ had considerably weaker diffraction intensities. This may have been due to TEM sample preparation and beam damage, since the film contained structurally disordered regions, as observed in HAADF STEM (not shown), likely as a result of the very large compressive strain (-3.6%).

4.7 Space Group and Octahedral Tilts of Strained $NdNiO_3$

Figure 4.10 illustrates the space group and Glazer tilt configuration [22] of bulk $NdNiO_3$ (a) and the most likely configurations for tensile (b) and compressively (c) strained films at room temperature. The orange axes represent the projected direction ($[001_O]$) of all images and diffraction patterns presented in this Chapter. The bulk structure is well known, and detailed in the literature, while the tilt configurations for both the tensile and compressively strained films are determined from geometric considera-

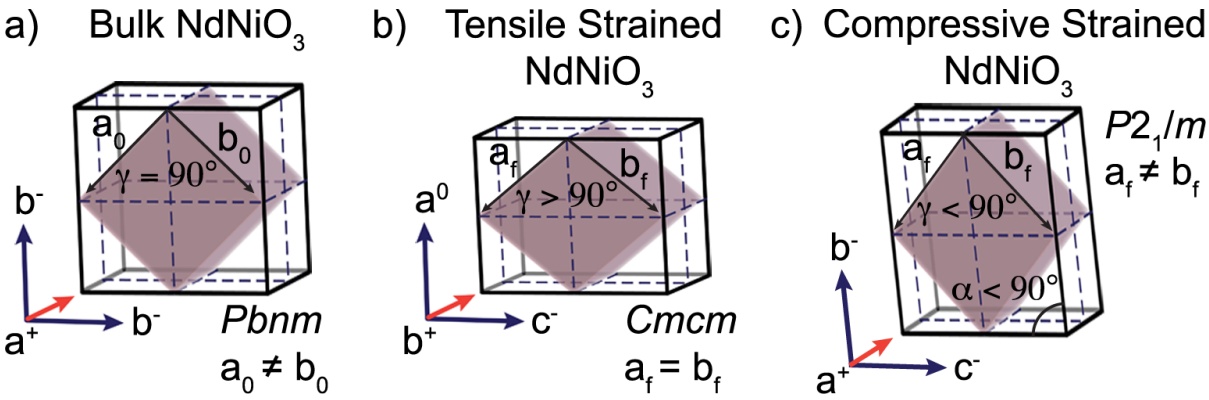

Figure 4.10: Schematic of the expanded $2 \times 2 \times 2$ pseudocubic unit cell for (a) bulk, (b) tensile strained, and (c) compressively strained $NdNiO_3$ films, showing relationships between key features in the orthorhombic/monoclinc lattice parameters, and the most probable Glazer octahedral tilts.

tions based on the epitaxial constraints of the substrate and the film lattice parameters [13, 2, 133]. A detailed analysis in determining the tilt systems of similarly strained films can be found in [13].

For the tensile strained film, the original primitive orthorhombic unit cell (P*bnm*) becomes best described using a centered orthorhombic cell (C*mcm*). The phases of the octahedral rotations remain the same as in the bulk, but their magnitudes change, with negligible tilt along the growth direction ($[110]_O$), for reasons mentioned earlier. Here, we use the convention of denoting the axis of zero tilt the *a*-axis. This configuration is the same as proposed by Vailionis [13], and the in-phase and out-of-phase tilts are likely different (this difference has no bearing on the tilt system or space group). In particular, the in-phase tilt along the projected viewing direction ($[001]_O$) is probably small.

Figure 4.11 shows simulated LA-PACBED of $NdNiO_3$ with certain distortions from the bulk structure, such as the absence of cation displacements or octahedral tilts. The simulations indicate that the similarity in intensity between 200 and 020 reflections in the tensile strained experimental $NdNiO_3$ pattern, as well as the absence of 120 reflections [Fig. 4.6(a)], are likely indications of reduced octahedral tilts.

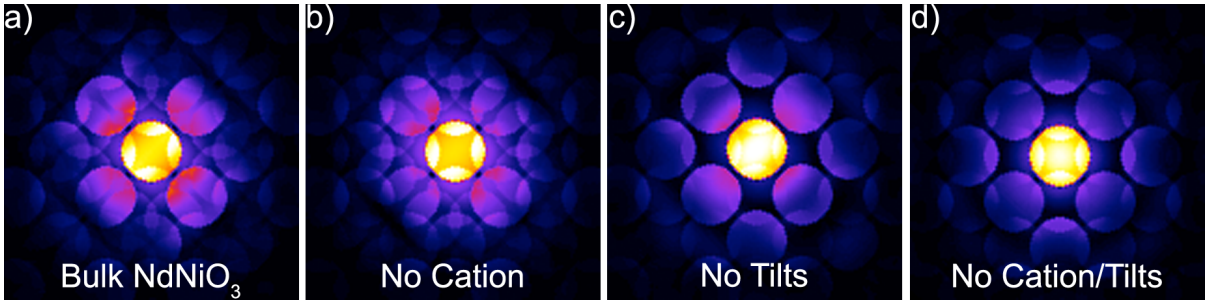

Figure 4.11: Simulated LA-PACBED of (a) bulk $NdNiO_3$, (b) bulk $NdNiO_3$ without cation displacements, (c) bulk $NdNiO_3$ without octahedral tilts, and (d) bulk $NdNiO_3$ without cation displacements and octahedral tilts. Sample thickness for all simulations is 23 nm.

For the compressively strained film, the most likely octahedral tilt rotation and space group is shown in Fig. 4.10(c). The angles, γ and α, are consistent with angle measurements from the experimental LA-PACBED patterns in Fig. 4.9 ($\gamma = 88.1°$, $\alpha = 89.4°$).

While a rigorous determination of the space group symmetry, based on electron diffraction (*e.g.* CBED [134]) is possible, it could not be done for the present study due to experimental challenges, such as the thinness of our samples and holder stability issues. However, the present analysis still presents compelling evidence for the structural symmetry of the films studied, and the proposed octahedral tilt patterns (Fig. 4.10) are consistent with both previous literature [13] as well as geometric arguments of the allowed tilts within their respective space groups [2].

4.8 Role of Lattice Symmetry in the MIT

Comparing the different structures between strained and bulk $NdNiO_3$ (Fig. 4.10), it seems curious that the compressively strained film does not undergo an MIT, even though it is the same crystal system (monoclinic) as the low temperature bulk insulating phase, and also has a similar tilt pattern as bulk $NdNiO_3$. To explain this observation,

Table 4.1: Space groups for selected three and two-tilt systems with and without ordering [2].

Tilt system number	Tilt system symbol	Space group (no ordering)	Space group (1:1 ordering)
Three-tilt systems			
8	$a^+b^-c^-$	$P2_1/m$ (#11-1)	$P\bar{1}$ (#2)
9	$a^+a^-c^-$	$P2_1/m$ (#11-1)	$P\bar{1}$ (#2)
10	$a^+b^-b^-$	$Pnma$ (#62)	$P2_1/n$ (#14-2)
11	$a^+a^-a^-$	$Pnma$ (#62)	$P2_1/n$ (#14-2)
Two-tilt systems			
15	$a^0b^+c^+$	$Immm$ (#71)	$Pnnn$ (#48)
16	$a^0b^+b^+$	$I4/mmm$ (#139)	$P4_2/nnm$ (#134)
17	$a^0b^+c^-$	$Cmcm$ (#63)	$C2/c$ (#15-1)
18	$a^0b^+b^-$	$Cmcm$ (#63)	$C2/c$ (#15-1)

we first point out that the expected space group of the compressively strained film is $P2_1/m$, which is *not* the same as the low temperature bulk space group $P2_1/n$. Although the difference seems small, its effect becomes clear when we consider the presence of ordering.

4.8.1 Effect of Ordering on Space Groups

The space group of a perovskite structure can be uniquely determined based on its Glazer tilt system [22, 2]. In many cases, octahedral tilts are also accompanied by some type of ordering on the cation site, which always results in a reduction of structural symmetry; at the least, translational symmetry will be lost if neighboring octahedral sites are no longer equivalent. The ordering can take any form: cation ordering of different atoms, spin/orbital/charge ordering, or bond length disproportionation, but its effect on lowering the original symmetry of the structure is the same.

Table 4.1 (data from [2]) shows the space group of relevant three and two-tilt systems, as well as the symmetry reduction that occurs when a 1:1-type ordering occurs (such as in

Fig. 4.2). As observed in bulk nickelates, order in the Pbnm space group (Pnma in Table 4.1) results in a symmetry reduction to P$2_1/n$. Introducing order into the P$2_1/m$ space group would similarly reduce the symmetry of the unit cell, to triclinic P$\bar{1}$. However, epitaxial constraints from a cubic or (110) orthorhombic substrate, with 90° in-plane angles, makes this impossible; any expitaxially strained film is bound to contain higher symmetry elements than the triclinic system. Therefore, by symmetry considerations, compressively strained films on cubic or orthorhombic substrates are unable to reduce to an ordered structure upon cooling. These simple considerations could answer the question on why compressively strained films have been observed to remain metallic and do not undergo an MIT, and is consistent with a charge/bond length order driven MIT.

4.8.2 Structural Transition in Tensile Strained $NdNiO_3$

The difference between room and low temperature LA-PACBED patterns (Fig. 4.6) for the tensile strained $NdNiO_3$ film shows clear evidence that the MIT is accompanied by a symmetry-lowering structural distortion. From Table 4.1, we see that ordering for the orthorhombic Cmcm space group results in a reduction to monoclinic C$2/c$. However, we noted earlier that the reduction of γ in the low temperature LA-PACBED indicates an increase in the octahedral rotations about the growth direction (Fig. 4.8). A re-introduction of tilts along this axis means that the structure returns to a three-tilt system, making P$2_1/n$ the likely space group of the low temperature tensile strained films.

From Fig. 4.10(b), we can see that tensile strained films grown on [110] orthorhombic substrates have 2-fold rotational symmetry along each of its cartesian tilt axes. If these films were grown in tension, on cubic substrates such as $(LaAlO_3)_{0.3}(Sr_2AlTaO_6)_{0.7}$ (LSAT) or $SrTiO_3$, the diad axis along the growth direction would change to a tetrad

axis, meaning that the unit cell would possess tetragonal symmetry. While this may seem trivial, the space group symmetry limits the Glazer tilt system the structure can possess, and the most likely tilt pattern with a tetragonal space group would be $a^0b^+b^+$ (Table 4.1), meaning that the out-of-phase tilt in Fig. 4.10(b) would change to in-phase. Although such a change might be expected to have a large effect on the bandwidth and electronic properties of the film, transport measurements [107] suggest otherwise: films grown on cubic LSAT and $SrTiO_3$ show MITs which vary systematically with the degree of strain, but do not show any anomalous behavior due to different substrate symmetry. These observations further support the view that the symmetry lowering structural distortion is a key requirement for the MIT to take place; the exact starting symmetry of the high temperature structure is not as important as long as it allows a transition to an ordered structure with lower symmetry. This occurs for tensile strained films, but is geometrically prohibited for compressively strained films.

4.9 Conclusions and Broader Impacts

In this Chapter, we used LA-PACBED, a STEM diffraction technique, to detect subtle symmetry changes due to epitaxial film strain and the presence/absence of an MIT in ultrathin $NdNiO_3$ films. Tensile strained films showed a structural transition below the MIT, while compressively strained films did not show a structural change, and did not undergo an MIT. While transport measurements show that the degree of epitaxial strain varies the MIT transition temperature, the strain state also affects the high temperature (above the MIT) symmetry and octahedral tilt pattern. Tensile strained films become orthorhombic (Cmcm) with Glazer tilt pattern $a^0b^+c^-$, while compressively strained films are monoclinic ($P2_1/m$) with tilt pattern $a^+b^-c^-$, similar to the octahedral tilt system of bulk $NdNiO_3$ ($a^+b^-b^-$). Thus even at room temperature, epitaxially strained $NdNiO_3$

has a different structure than in the bulk, and this modified structure should be used as the starting model in future theoretical work involving the MIT and other associated phenomena of coherently strained films.

Our results present a remarkably simple understanding of the MIT in $NdNiO_3$ thin films: the MIT only occurs in films with a high temperature space group that will permit a symmetry reduction to an ordered state. This occurs in tensile strained films, which undergo an MIT, but not compressively strained ones, which remain metallic at all temperatures, due to geometric constraints. More generally, these results present clear evidence for charge ordering, or bond length disproportionation, being intimately linked to the insulating state of RNiO$_3$s. This transition is highly reliant on the high temperature "parent" space group symmetry, which can be tuned by epitaxial strain.

Lastly, we note that the present results could also provide insight into the nature of the non-Fermi liquid phase observed in RNiO$_3$ films for when the MIT is suppressed. In particular, these films would have a lower symmetry starting structure, which may be incompatible with reaching a long-range ordered state. The non-Fermi liquid phase could therefore be potentially caused by such a suppressed or "frustrated" ground state, which is limited to only local or short-range fluctuations in magnetic or bond length order parameters.

Chapter 5

Variable-Angle HAADF

This Chapter is different from the others in that it is focused on transmission electron microscopy (TEM) technique development, rather than materials properties or physics. Here, I develop a new technique called variable-angle high angle annular dark field (VA-HAADF), a technique which utilizes the angular dependence of electron scattering to improve sensitivity in scanning TEM (STEM) imaging. I provide simulation and experimental demonstration of the effectiveness of this new method, specifically, as applied for precise and accurate determination of three-dimensional (3D) dopant depth locations. However, the general concepts behind VA-HAADF can be applied in STEM to enhance overall contrast and improve image analysis in a wide range of applications.

In this chapter, I first provide an overview of quantitative STEM, and its implementation in determining the position of substitutional dopants in crystalline materials. Then I introduce the concept of variable-angle HAADF, and demonstrate its applicability in increasing the contrast in STEM imaging. A detailed review of the quantitative STEM procedure is given in Appendix D while additional supporting information and calculations for VA-HAADF are provided in Appendix E.

5.1 Quantitative STEM

High angle annular dark field (HAADF) scanning transmission electron microscopy (STEM) is a popular and widely employed technique for atomic resolution imaging. Strong scattering of the incident probe electrons by the sample nucleus results in image intensities that are highly sensitive to the atomic number (Z) [135], producing intuitive and directly interpretable images. For example, the Z-contrast allows individual dopant atoms to be detected in crystals, using both HAADF imaging [136, 137, 138, 139, 80, 140, 141, 142] or electron energy loss spectroscopy (EELS) [143, 144, 145, 146].

A schematic of the STEM imaging mode is shown in Figure 5.1(a), where the ADF detector lies in the back focal plane to detect electrons that have been scattered by the sample. The scattered electrons are incoherently integrated over the detector geometry to form the STEM intensity signal for each probe position (image pixel). Images formed using an ADF detector with sufficiently high inner angle [147, 148, 149, 150] (HAADF) can be described by an incoherent imaging model, allowing simple determination of the actual specimen structure.

Additionally, the use of a convergent "point" probe and an annular detector also allows parallel acquisition of diffraction or elemental (EELS) data, by using a CCD camera or spectrometer located within the inner angle of the ADF detector [Fig. 5.1(a)], for complementary structural analysis. Different experimental setups can be used to acquire simultaneous information in parallel from a combination of ADF and bright field (BF) detectors, CCD camera, or EELS spectrometer.

More recently, quantitative interpretation of HAADF STEM images have been achieved by using the detector response function [created by scanning the incident beam across the detector, see Fig. 5.1(b)], to normalize the scattered electron intensity to the incident beam [35, 69]. This procedure places image intensities on an absolute scale [Fig. 5.1(c)],

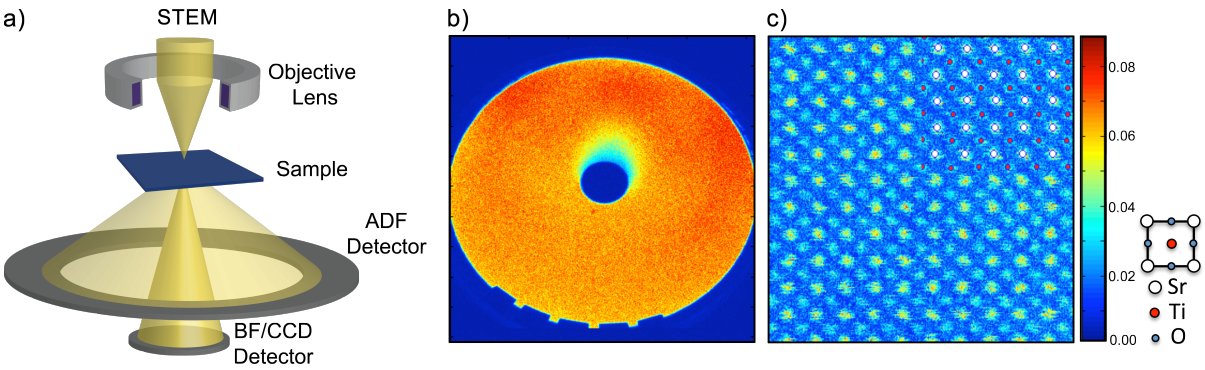

Figure 5.1: (a) Schematic of STEM imaging mode, with ADF detector in the diffraction plane below the sample. (b) Image of actual HAADF detector, captured by scanning the probe across the detector surface, showing the intensity response of each point on the detector. (c) HAADF image of $SrTiO_3$ normalized to the incident beam. Inset on top right shows schematic of Sr and Ti columns in the projected [100] direction.

which allows for direct comparison between experimental and simulated image intensities. Near perfect agreement has been achieved for atomic resolution HAADF images, with sensitivity within single atom precision [151]. Direct quantitative analysis of STEM image intensities is now routine [152, 153, 154], and has been used to provide important structural information such as elemental composition [152, 155], thickness [39, 156], and direct atom counting [151]. An overview of the quantitative STEM procedure used in this chapter can be found in Appendix D.

The advancement of quantitative microscopy is crucial for the development of new materials. As devices shrink to increasingly smaller scales, new techniques will be needed with the resolution to adequately characterize those materials. Quantitative STEM does just that, allowing us to probe materials at the atomic level and extract quantitative information in ways that were previously impossible. Of particular importance is the study of interfaces and defect structures. As materials approach the nanoscale, their properties become dominated by interfaces and defects. For example, the performance of current generation silicon transistors and devices are already mainly controlled by

individual dopant atoms [157, 158, 159]. Quantitative STEM offers a way to precisely locate and analyze these interfaces and defects, providing important atomic information on the local structure, such as which types of atoms and how many of them are present, and where specific atoms are located.

5.2 3D Dopant Depth Determination

While current hardware advancements on spherical aberration (C_s) lens correctors in TEM now allow for sub-angstrom lateral resolution [160, 161, 162, 163], obtaining three-dimensional (3D) depth information is significantly more challenging. Approaches involving through-focus series, depth sectioning, or confocal microscopy [137, 164, 165, 166] remain limited in resolution, due to finite depth-of-focus limitations, while tomographic reconstructions [167, 168] are also resolution limited and require the acquisition of many images at different sample tilts.

Alternatively, quantitative STEM has recently been employed to determine the 3D arrangement of dopant atoms in a host matrix [46, 169]. In the study by Hwang et al., Gd dopant atoms were located in a $SrTiO_3$ matrix, as seen in Figure 5.2(a-c) [46]. Their approach compared the experimental intensities of A-site (Sr/Gd) and B-site (Ti-O) columns with simulated intensities containing a certain number and configuration of dopant atoms [Fig. 5.2(d, e)]. Using statistical analysis based on an experimentally determined noise or "error" function [a 2D gaussian fit to the experimental data spread, see inset of Fig. 5.2(d)], the number and location of dopant atoms in each column can be calculated, with an uncertainty of a unit cell or less. An example of two regions containing dopant atoms is shown in Figure 5.3(a, b), where the expected value and uncertainty of the dopant depth position is indicated in Fig. 5.3(c, d). While the result is remarkably promising, and a prime demonstration of the capabilities of quantitative STEM, many

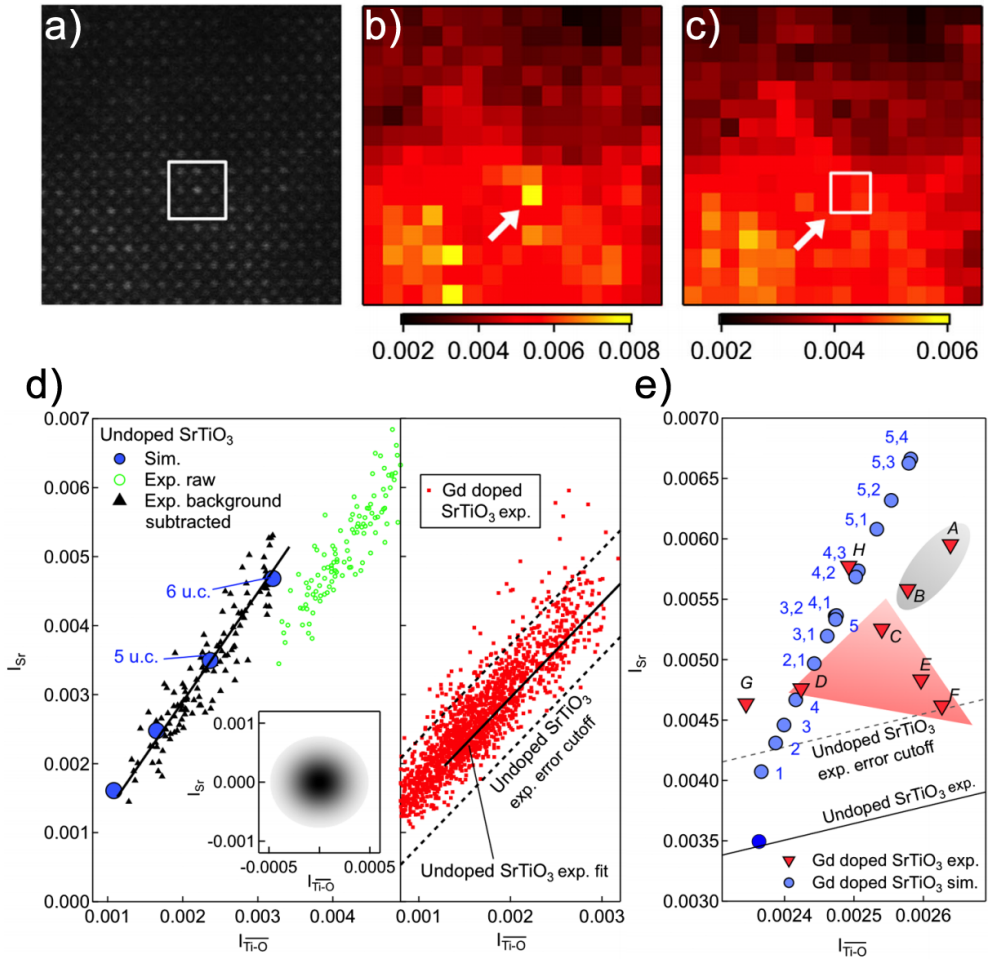

Figure 5.2: (a) HAADF STEM image of 3.4% Gd-doped $SrTiO_3$. White box indicates location of dopant. Intensity maps of Sr (b) and Ti-O (c) columns unambiguously show lateral position of dopant atom based on image intensity. Scale bars indicate the intensity value normalized to the incident beam. (d) Experimental plot of Sr and Ti-O column intensities for undoped $SrTiO_3$, before (green open circles) and after (black triangles) background subtraction. The inset shows the 2D error function calculated from the experimental data spread. Experimental data for Gd-doped $SrTiO_3$ is shown by red data points, with a fit for undoped $SrTiO_3$ shown by the solid black line, and the experimental error indicated by dashed lines. (e) Multislice simulations (blue circles) of all possible dopant configurations, for a column containing one or two dopants in a 5 unit cell (u.c.) thick region. The labels (numbers) indicate the dopant position in the column, with 1 being the closest to the top surface, and 5 being the closest to the bottom surface. Figure is adapted with permission from Ref. [46]. Copyrighted by the American Physical Society.

challenges remain in increasing the robustness of the analysis and increasing its adoption for more general use.

Due to dynamical scattering of the electron beam, the probe intensity will undergo "channelling", or intensity oscillations through the depth of a sample aligned along a zone-axis. Figure 5.3(e) [46] plots the electron probe intensity as it propagates through a Sr column in $SrTiO_3$, showing this oscillatory behavior. This same effect is what causes the column intensities to be sensitive to the dopant depth position [170, 171, 172, 80]. Currently, the approach used by Hwang et al. [46] has been purposefully limited to the monotonically increasing portion of the first probe intensity oscillation [$\sim$ 3.9 nm for the particular microscope and dopant/host combination, Fig. 5.3(e)]. Such thin samples can be difficult to make, depending on the material system, and would need to be even thinner for aberration-corrected microscopes with larger convergence angles [80]. While Ishikawa et al. [169] used thicker samples, their dopant/host system (Ce-doped AlN) has a much higher atomic number difference. Their analysis is limited to one full intensity oscillation, and only takes into account a single dopant in each column.

In general, depth-resolved information from STEM will require thin samples to enhance dopant visibility [136, 80], with larger Z-differences between the dopant and host atoms also serving to enhance contrast [80, 145, 173]. However, determining dopant locations from image intensity alone can often be difficult since intensities from different dopant configurations can often be very similar, particularly when taking into account multiple dopants per column [see Fig. 5.2(e)].

The primary limitation for accurate dopant depth identification is inherent experimental noise, such as from the detector, sample instability under the electron beam, sample contamination, surface amorphous layers, sample imperfections, etc [174, 175]. In the study by Hwang [46], all these different sources were accounted by a single "error" function, estimated from the experimental data spread [see inset of Fig. 5.2(d)]. When

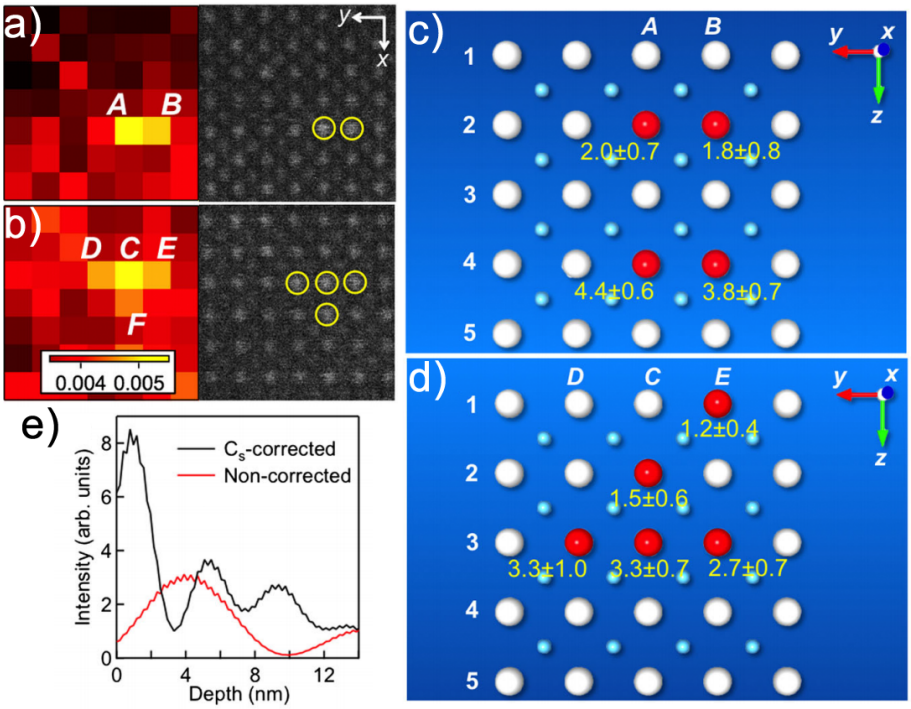

Figure 5.3: (a, b) Sr intensity maps (left) and HAADF STEM images (right) of two regions containing dopant atoms, where dopant columns are labelled A-F. (c, d) Schematics showing the dopant atom configurations from (a, b), respectively, with dopant depth positions and uncertainties indicated by yellow labels. The most probable dopant positions are shown in red. (e) Probe channeling characteristics for C_s-corrected and non-corrected probes. The probe is positioned above a Sr column in $SrTiO_3$ along [100]. Figure is adapted with permission from Ref. [46]. Copyrighted by the American Physical Society.

intensity differences between different atomic configurations are small, the experimental noise function can easily span multiple configurations, resulting in ambiguous determination of the actual depth position. For example, certain configurations of the Gd dopants from [46] had an uncertainty range that spanned multiple positions, even when the calculated precision was less than a unit cell (*e.g.* in Fig. 5.3(d), the dopant atom in the center is at position 1.5 ± 0.6). Additionally, due to how the positions are calculated, certain configurations are prone to generating erroneous position estimates.

In principle, reducing the experimental noise function will lead to improved identification of dopant atoms using quantitative STEM. This could be done, for example, through the development of higher brightness gun sources or more stable imaging environments. However, these approaches are costly, may involve major hardware upgrades, and face inherent limitations, such as beam damage.

Currently, ambiguous depth determination for certain atomic configurations, as well as sample thickness and dopant/host Z-difference constraints limit the accessibility of the technique to certain ideal samples. In order to relax these constraints and attempt to employ more widespread adoption of the technique, we need to improve the dopant contrast in STEM and reduce the uncertainty in the depth measurement. To that end, we demonstrate the usefulness of a new technique, variable-angle HAADF (VA-HAADF).

5.3 Angular Dependence of Electron Scattering

A key principle behind the development of HAADF STEM is the annular geometry of the detector: by changing the effective distance of the detector from the sample, or "camera length", only electrons scattered beyond a selected angular regime are collected [147]. Using a detector with sufficiently large inner angle [147, 148, 149, 150] is usually desirable; although the signal is much lower, since only a small percent of electrons are

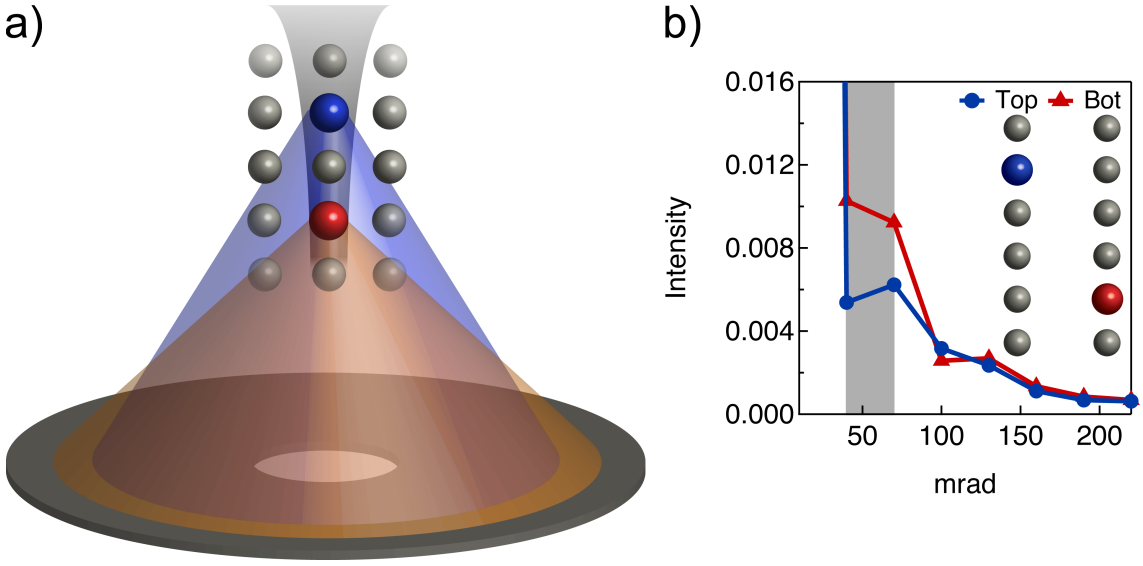

Figure 5.4: (a) Schematic showing how beam channeling along an atomic column can result in angle-dependent scattering in STEM. Atoms further down a column "see" a more focused probe and consequently scatter more to higher angles. (b) Simulated multislice results showing scattered intensity as a function of annular detector angle (in 30 mrad segments, as exemplified by the gray box). Figure reproduced from Ref. [45].

scattered to these higher angles, the resulting image is formed from incoherently scattered electrons, and are therefore not subject to contrast reversals. The choice of angular regimes has long been known to have a strong influence on the resulting image, and this concept has been advanced over the years to capture additional information. For example, the exact Z-number dependence of ADF imaging varies according to the detector inner angle [147, 176]. Annular bright field imaging takes advantage of this property by using a small collection angle to image light atoms which scatter less strongly [177, 178, 179], while segmented detectors [178] have been used to image microscopic electric fields based on anisotropic electron scattering [180].

VA-HAADF works on this same principle of using selective angular regimes for detecting changes in electron scattering strength, thereby offering an alternative route to enhancing contrast in STEM. For the case of impurity atoms in a matrix, the angular

dependence of the electron scattering depends on the dopant depth position. A simplified view, ignoring the depth dependent probe intensity oscillations [Fig. 5.3(e)], is shown in Figure 5.4(a). Dynamical scattering causes the incident beam (gray) to be "channelled" along an atomic column, resulting in atoms deeper in the sample to see a more focused probe. A dopant atom closer to the bottom of the sample (red) would scatter the incident electrons to higher angles (since more electrons are traveling closer to the nucleus in the focused probe) relative to a dopant atom nearer to the entrance surface (blue). Thus, the angular sensitivity of dopant depth scattering can be exploited by selecting certain angular ranges to more easily identify different dopant atom configurations.

In real materials, however, dynamical scattering effects are more complicated, and image simulations must be employed for quantitative analysis. Figure 5.4(b) shows multislice calculations of the scattered intensity for different detector angular ranges, in 30 mrad steps (width of gray box). The scattered intensity from two different dopant configurations, one with a dopant atom near the top (blue) and one near the bottom surface (red), are plotted, and show a significant intensity difference for the angular range between 40-100 mrad. Thus, a detector with angular resolution would be more sensitive to the dopant depth from the measured signal intensity.

The idea behind VA-HAADF is to use multiple detectors with different angular regimes to combine the depth information from dopant scattering in order to significantly reduce the uncertainty in the dopant depth position measurement. In this Chapter, we collect HAADF signals from two different detector configurations (different angular regions), and combine the information to uniquely identify certain dopant configurations that are indistinguishable using a single setting. Using simulations and experiments, we demonstrate significant improvements in 3D dopant imaging by using multiple collection angles. We show that the resulting calculations yield values closer to the correct, discretized positions, with lower uncertainty.

5.4 VA-HAADF Experimental Setup

5.4.1 Sample and Preparation

We studied $SrTiO_3$ films doped with Gd atoms (substitutional doping on Sr sites) at a nominal 4% concentration. Films were grown by hybrid molecular beam epitaxy (growth details in [10]). An undoped $SrTiO_3$ single crystal substrate was also used as a calibration sample to determine the experimental noise and to model the "error function" (more details below). TEM samples were prepared in plan-view geometry by mechanical wedge polishing at a 1° angle.

5.4.2 Microscopy Conditions

HAADF STEM images were taken on a FEI Titan operated at 300 kV (C_s=1.2 mm), with a 9.6 mrad convergence angle. The images were recorded using 512 × 512 pixels with a 50 μs dwell time, resulting in $\sim$ 160 atomic columns per image.

Two different detector angular regions were accessed by selecting separate camera lengths. Camera lengths of 100 and 130 mm, referred to as detector 1 and detector 2, respectively, were used in succession for each image. Centering and calibration of each detector was performed prior to the experiment, including accurate measurements of the inner and outer angles (60-390 mrad and 47-306 mrad for 100 and 130 mm camera lengths, respectively). Both detector inner angles are sufficiently large to be adequately described by the incoherent imaging model [181, 182, 183], which is important for retaining all the benefits of HAADF STEM. The contrast of the undoped columns is similar in both angular regimes [184], and therefore the changes in the ratio of intensity between Sr and Ti-O columns can be attributed to the presence of Gd dopants on Sr sites.

Image intensities were normalized to the incident probe intensity separately for each

detector configuration, according to:

$$\overline{I_{xy}} = \frac{I_{xy} - I_o}{I_p - I_o} \tag{5.1}$$

where $\overline{I_{xy}}$ is the normalized image intensity at position (x, y), I_{xy} is the measured intensity at position (x, y), I_o is the detector offset (blank beam intensity), and I_p is the incident probe intensity. The general quantification procedure is detailed in [69], although the present study used the FEI acquisition software as opposed to a digital signal analyzer. An extended summary of the procedure, as well as differences from [69] is given in Appendix D. To account for the detector non-uniformity [185], the incident probe intensity, I_p, is obtained by averaging the signal between 60-120 mrad and 47-141 mrad for detector 1 and detector 2, respectively.

Atomic column intensities (I_{Sr} and I_{Ti} for Sr and Ti-O columns, respectively), were extracted using a custom MATLAB script. The intensity within a small circular region, with radius 1/4 the length of a unit cell ($\sim$ 10 pixels), was averaged around each atomic column centroid position to obtain an integrated intensity value. These integrated intensities are less sensitive to defocus and coherence effects, and allow for more robust comparisons to simulations over peak intensities [186]. As noted in [46], due to the extreme thinness of the samples ($\sim$ 2 nm), the surface amorphous layers will contribute a significant portion of the measured signal. This signal is difficult to remove experimentally, so a constant background intensity, I_{B}=0.003, was subtracted from the experimental values for comparison with simulations, to account for the surface contribution. This value was determined by experimental fitting of the $SrTiO_3$ calibration sample, as seen in Fig. 5.5 for detector 2.

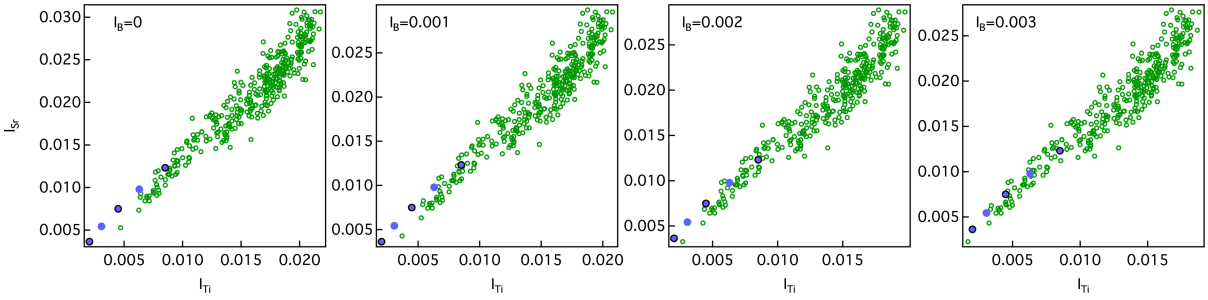

Figure 5.5: Experimental fitting of $SrTiO_3$ data (green open circles) to simulated data points (blue circles) in I_{Sr} vs. I_{Ti} space, with different subtracted background intensities, I_{B}, for detector 2.

5.4.3 Simulation Conditions

Frozen phonon image simulations of Gd-doped $SrTiO_3$ were carried out using the Kirkland program suite [38] for all possible dopant configurations involving zero, one, or two Gd dopants. An overview of different simulation methods are given in Appendix B. Two different collection angles were simulated, to match the experimentally determined detectors (60-390 mrad and 47-306 mrad). Simulated structures were all five unit cells thick, Ti terminated, and did not include the possibilities of Sr or Gd adatoms. The frozen phonon simulations used a 1024×1024 pixel mesh with a 15.62×15.62 Å supercell (4×4 unit cells). The sample thickness was purposefully chosen, and limited below 4 nm to avoid ambiguity caused by the probe intensity oscillations due to channelling along a zone axis, which would complicate unique identification of the dopant depth position. Five unit cells (~ 2 nm) was chosen as the thinnest region where large enough sampling data could be collected, while also limiting the total number of simulated dopant configurations needed (16). To further reduce computation times, simulations were calculated at 0 K, and thermal diffuse scattering effects due to finite temperature were included by using a calibrated intensity ratio, as described in more detail in Appendix D.

5.5 VA-HAADF of Gd-doped $SrTiO_3$

Figure 5.6(a) shows experimental (green points) and simulated (blue circles) intensities for Sr and Ti columns (I_{Sr} vs. I_{Ti}) in the undoped $SrTiO_3$ calibration sample. The experimental data is fit to the simulated points by subtracting a constant background intensity, $I_{\mathrm{B}} = 0.003$, over the shown thickness range, between three and six unit cells (Fig. 5.5). The same I_{B} was used for both detectors (left and right columns, respectively). The residual of the experimental data to a fit of the simulated points are shown Fig. 5.6(b). A Gaussian "error function" can be modeled to each set of residuals, which represents the random experimental variability and noise of each data set.

Figure 5.6(c) shows an extended portion of I_{Sr} vs. I_{Ti} space with simulated undoped $SrTiO_3$ (blue circles) and Gd-doped $SrTiO_3$ configurations (yellow regions). Exact dopant configurations have been calculated for the 5 u.c. case, as shown in yellow circles, while the approximate locations of the other thicknesses can be well estimated. Gd dopants strongly affect the Sr column intensities, as expected, while having little effect on Ti intensities. Therefore, the Ti intensities around each Sr column gives better indication of the local thickness and whether dopants are present.

The Guassian error function for each set of measurements, modeled after the residuals in Fig. 5.6(b), is overlaid (in blue) on the 5 u.c. $SrTiO_3$ simulation, but would also equally apply to any other simulation point. While this error function serves as a catch-all for any random errors, any other systematic sources of error could fall outside this error function, errors such as the probe and detector calibration, non-uniform surface amorphous regions, and detector non-uniformity. Calibration errors can be mostly mitigated by careful fitting to a calibrated data set, such as $SrTiO_3$ in the present case, but the presence of variable thickness surface layers could non-uniformly alter the intensities of certain columns in an unpredictable way. While surface amorphous layers are unavoidable and sure to exist, we

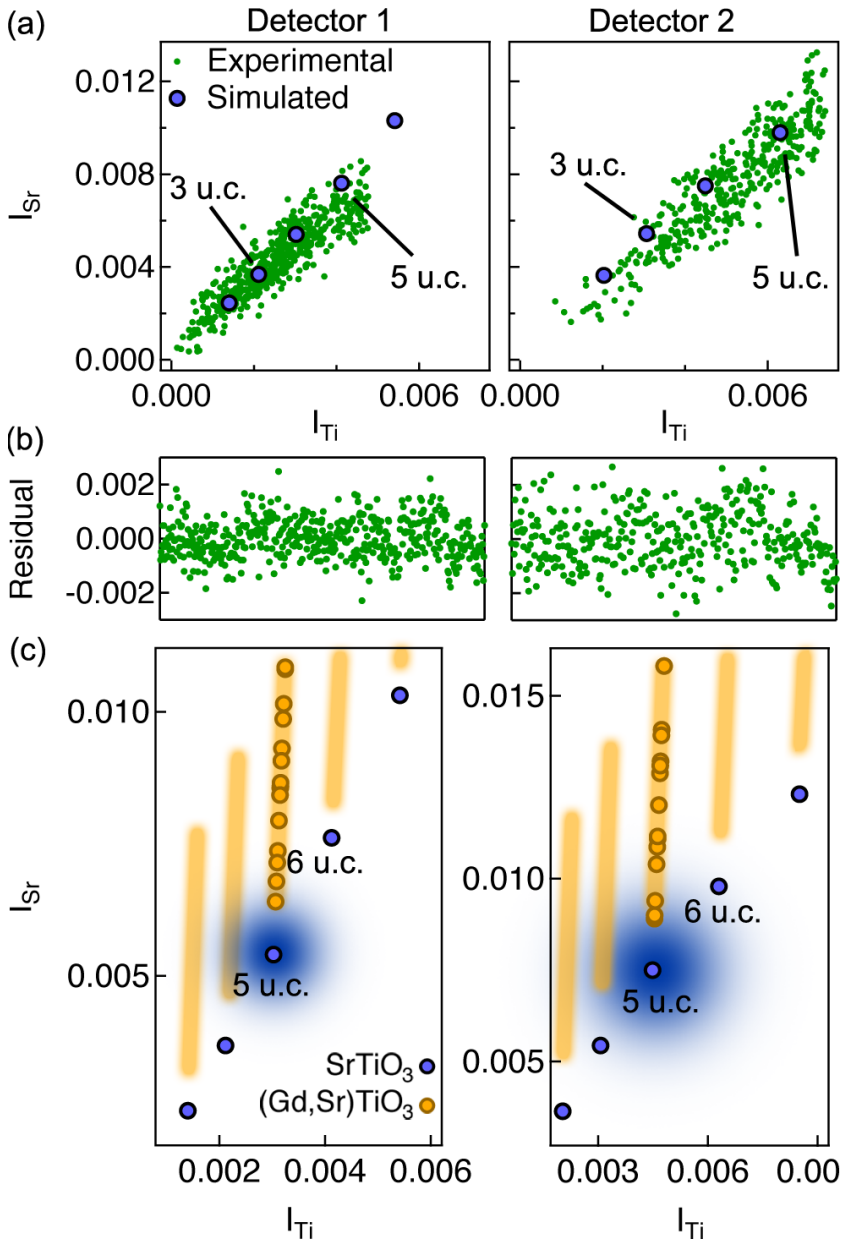

Figure 5.6: (a) Experimental and simulated I_{Sr} vs. I_{Ti} for the undoped $SrTiO_3$ of 3 to 6 u.c. thicknesses for detector 1 (left) and detector 2 (right). Experimental data points are after subtraction of a constant background, $I_{\mathrm{B}} = 0.003$. (b) Residual of experimental data with fit to simulated points. (c) I_{Sr} vs. I_{Ti} for simulated undoped and Gd-doped $SrTiO_3$ for detector 1 (left) and detector 2 (right). Individual configurations for 5 u.c. thick samples are shown for the Gd-doped $SrTiO_3$ while rectangular bars mark the general areas in other regions where doped configurations would appear. A 2D Gaussian, with standard deviation calculated from the residual of the data in (b), is superimposed on the undoped 5 u.c. position. Figure partially reproduced from Ref. [45].

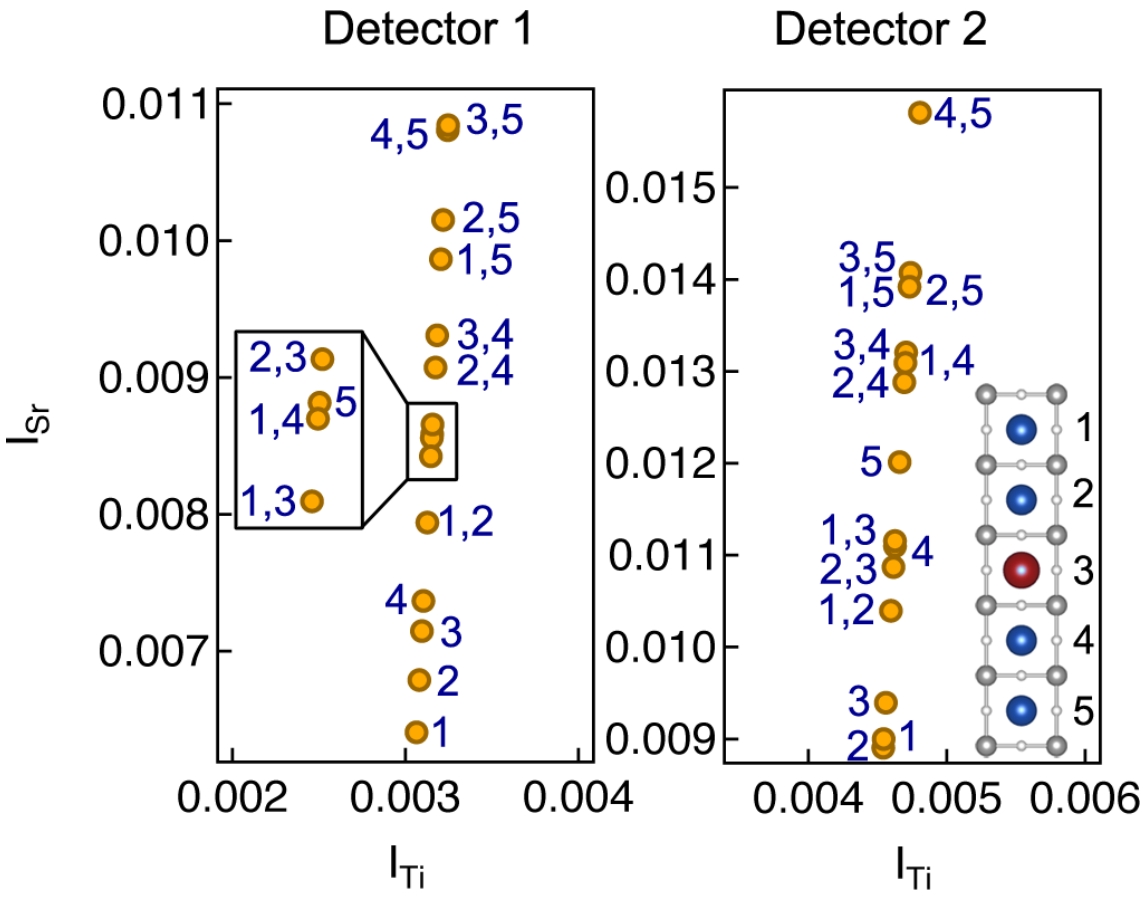

Figure 5.7: Magnified region of simulated I_{Sr} vs. I_{Ti} for 5 unit cell thickness for detector 1 (left) and detector 2 (right). Individual dopant configurations are labeled according to the position(s) of the dopant(s). The dopant positions are shown in the inset. Figure reproduced from Ref. [45].

currently do not have any way to estimate how much variability in thickness there might be. However, since we only focus on one particular thickness (5 u.c.), which is fit to a calibrated data set ($SrTiO_3$), we do not expect the variability in the amorphous layer to be significant compared to the random variability in the measurement, as encapsulated by the Gaussian error function.

In the current study, we focus only on sample thicknesses of 5 u.c., and include simulations of all possible dopant configurations containing zero, one, or two Gd dopants per Sr column. Columns containing three or more dopants are highly unlikely for this

thickness and nominal dopant concentration (4 at. %) [46]. This thickness region is magnified in Fig. 5.7, which shows all 15 *doped* configurations (5 single, 10 double) for each detector. The labels in blue denote the position of the Gd dopant along the atomic column, with 1 indicating the top surface and 5 the bottom surface, as shown in the inset on the right. A single number represents one dopant, while two numbers indicate two dopants in the column.

From Fig. 5.7, we can identify significant qualitative differences between the two detectors. For instance, the dopant configuration *4,5* and *3,5* using detector 1 have virtually the same intensities, and would be virtually indistinguishable, while they have a large intensity separation with detector 2. Several other such examples exist, where one configuration would be much more difficult to distinguish using a particular detector, such as single-dopant configurations *4*, *5*, and the double-dopant configuration *2,5*. It is important to note that neither detector is universally better for all configurations. Therefore combining the information from two or more detectors is key to improving the accuracy and precision of quantitative intensity measurements for dopant depth calculations.

5.6 VA-HAADF Calculations

The general procedure used here for quantitative determination of the dopant depth can be separated into two steps: first, determine the number of dopants in the column, and second, determine the location of the dopant(s). In both steps, we calculate the probability that the column contains x dopants or is located at y based on the experimentally determined error function. The only difference between the two steps lies in which configurational probabilities contribute to the final probabilities. The basic principle of calculating configurational probabilities, based on an error function, is first outlined

below.

Figure 5.8 shows a general schematic of a simplified calculation. Consider an experimental data point (green) in I_{Sr} vs. I_{Ti} space, and three simulated points (yellow) representing three possible dopant configurations, as shown in Fig. 5.8(a). An experimental Gaussian error function (blue) is overlaid over each simulated point (it can alternatively be thought to occur only on the experimental point). The probability of the experimental data point corresponding to a particular calculated configuration, i, is given by:

$$p_i = \frac{norm_i(t)}{\sum_n norm_n(t)} \tag{5.2}$$

where t is the distance between the experimental and simulated point (black lines), normalized to the standard deviation of the Gaussian error function (blue), and $norm_i(t)$ represents the value of the Gaussian probability distribution function for a given distance t. The subscript, i, represents an experimental point, while n represents each dopant configuration considered. The experimental Gaussian error function is modeled as a normal distribution, with mean, μ, at the simulated intensity value for each configuration, and standard deviation, σ, determined experimentally from the calibration sample [Fig. 5.6(b)]. 2D projections of the error function for each simulated position is shown in Fig. 5.8(b), with μ, σ, and t_i indicated. The values for $norm_i(t)$ can be found using any statistical software. The calculation of the configurational probability, p_i, for each simulated position, is shown schematically in Fig. 5.8(c) for this simple case.

5.7 Determining the Number of Dopants

The calculation to determine the number of dopants in a column is similar to the example given above, in that we are interested in the most probable configuration of an

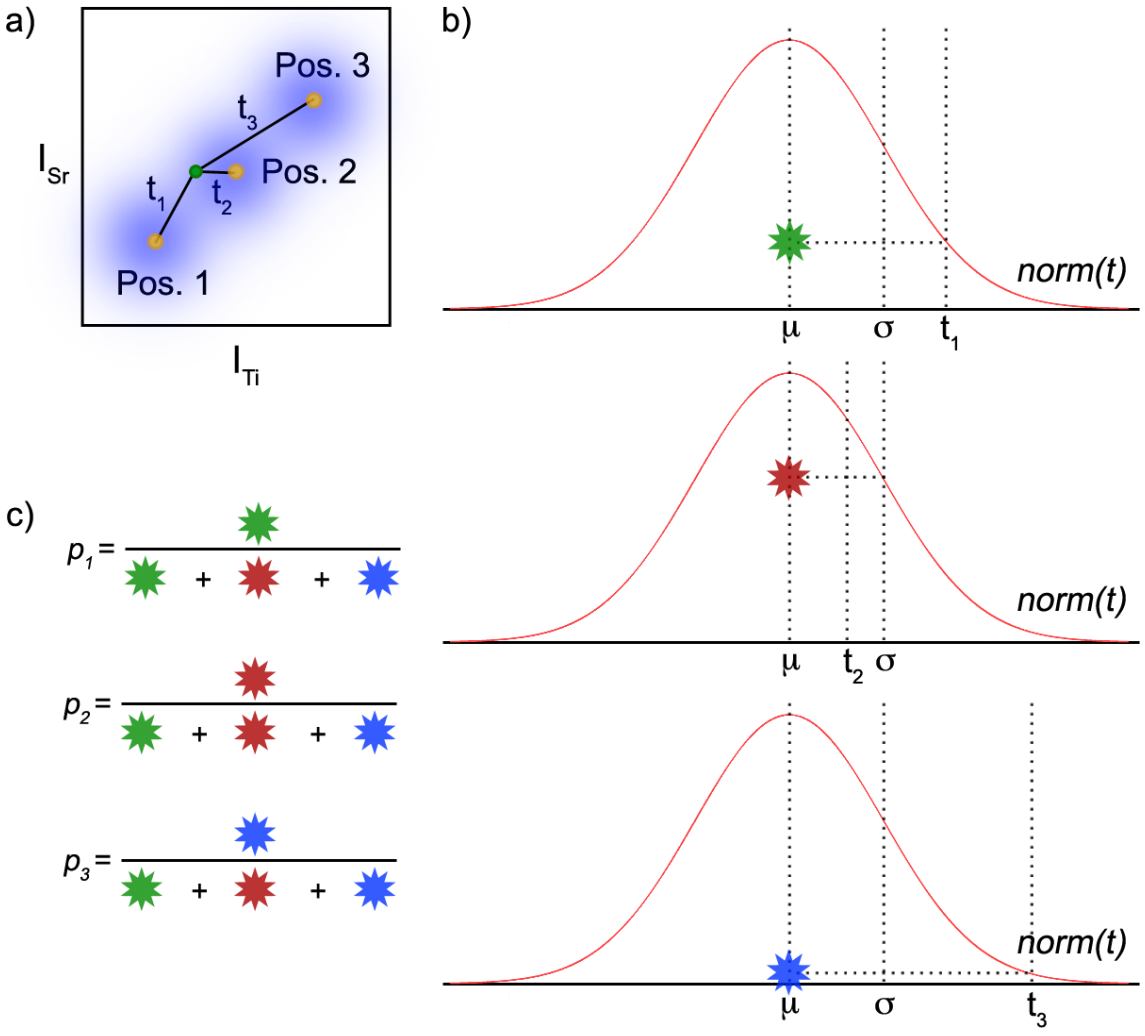

Figure 5.8: (a) Experimental (green) and simulated (yellow) data points in I_{Sr} vs. I_{Ti} space, with overlaying Gaussian error function (blue). The distances between the experimental and simulated points, normalized to the error function, are labelled by t_i. (b) 2D projection of the error function for each t_i. Error function is modeled as a normal distribution with mean, μ and standard deviation, σ. The value of $norm_i(t)$ for each t_i is indicated by colored stars. (c) Calculation of p_i, as given by Eqn. 5.2, for the example data shown in (a).

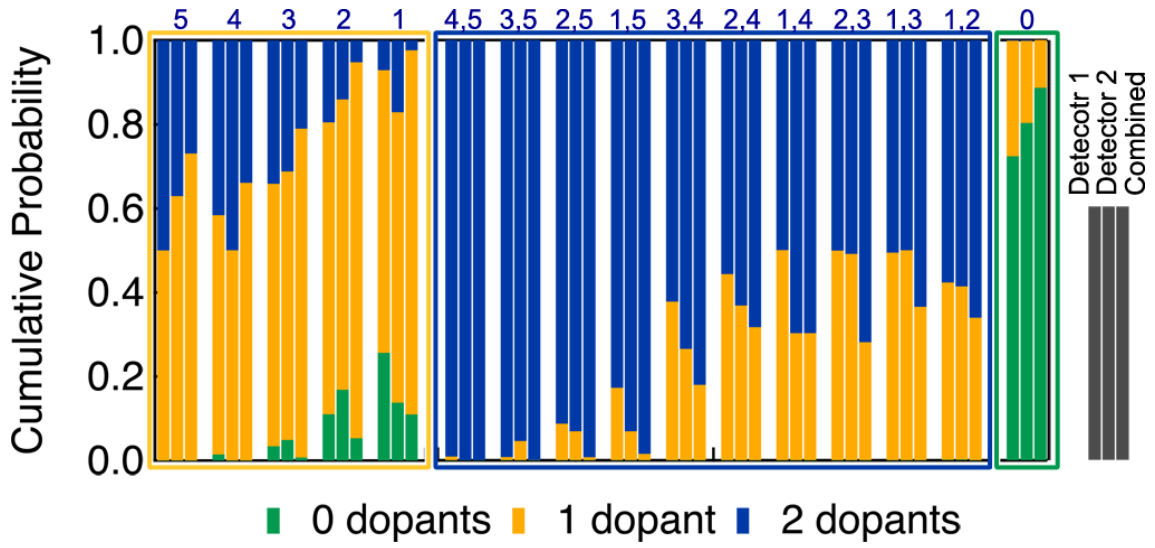

Figure 5.9: Probabilities of detecting 0, 1, or 2 dopants in each dopant configuration, given the experimental error function determined from Fig. 5.6(b). Each group of three bars represents (from left to right) the probabilities for detector 1, detector 2, and combining the information from both detectors. Figure reproduced from Ref. [45].

experimental data point between three simulated configurations: the closest (in terms of normalized distance, t) zero, single, or doubly doped case. Only the *closest* simulated position for each of the cases are used, and the resulting configurational probabilities are calculated similar to Fig. 5.8(c) to give probabilities of having zero, one or two dopants in each column. A more detailed example calculation is given in Table E.1.

The configurational probabilities can be calculated for each detector separately, but we can also calculated a *combined* probability incorporating the information from both detectors simultaneously, by treating each one as an independent measurement. Treating each measurement as independent is valid if we assume the spread around each discrete configuration (error function) is due to *random* noise. The calculation now becomes a compound probability of two independent events: for the example illustrated in Fig. 5.8, $norm_i(t)$ of each detector would be multiplied together to give a compound $norm_i^c(t)$ for the combined detector calculation.

Figure 5.9 illustrates the results of the calculations, detailed above, for having zero, one, or two dopants for each simulated configuration, after incorporating the experimental error function at each simulated point. Each group of three bars represents a certain dopant configuration, labelled in the same notation as in Fig. 5.7, while the bars represent, from left to right, the calculation for detector 1, detector 2, and using the combined information. For each detector and configuration, the probabilities of having zero, one, and two dopants are indicated by the color of the bar, with the length indicating the degree, up to a cumulative probability of 1. The calculations were carried out assuming the experimental point was located at the position of the labeled configuration.

From Fig. 5.9, we see that a column containing two dopants in positions *2,3* or *1,3* would show a nearly even probability split between having 1 or 2 dopants, given the experimental error function, using either detector. For columns with one dopant, configurations *5* or *4* would show nearly an even probability split if only one detector (1 or 2, depending on which case) is used. While the number of dopant atoms in most configurations can be accurately determined with a single detector setting, to reasonable certainty, certain configurations cannot, as shown by Fig. 5.9. However, if we consider the probabilities from using the combined detector information (rightmost column), we see a dramatic improvement in the accuracy of the technique; the probability of calculating the correct number of dopant atoms is greatly increased for each dopant configuration.

Table 5.1 summarizes the results for the four dopant configurations discussed above. While one detector might be better for a certain configuration (*i.e.* detector 2 for single dopant configuration *5*), using combined probabilities results in systematic improvements for all configurations. Figure 5.9 shows that the correct number of dopants can be identified for every configuration, to a reasonable confidence level, when the combined probabilities from both detectors are used.

Probability of Correct Number of Dopants

Dopant Position(s)	Detector 1	Detector 2	Combined	Improvement
5	50.0%	62.9%	73.1%	16%
4	57.0%	50.1%	66.1%	16%
2,3	50.1%	50.1%	71.9%	44%
1,3	50.6%	50.0%	63.5%	25%

Table 5.1: Probabilities of determining the correct number of dopants for select dopant configurations, using detector 1, detector 2, and the combined information from both detectors. The improvement is the percent increase of the combined detector over the best performing single detector. Table reproduced from Ref. [45].

5.8 Determining the Depth of Dopants

After determining the number of dopants in a column, we determine the depth position of the dopant(s) by calculating the expectation value of the dopant position, according to:

$$\mu = \sum_i z_i p_i \tag{5.3}$$

where z represents the atom position and p is given from Eqn. 5.2. Here, however, the subscript, i, refers to the subset of configurations matching the determined dopant number. For example, if we determined we had 1 dopant in the column, z_i and p_i would be limited to the 5 single dopant configurations, while if there were 2 dopants, z_i and p_i would be the subset of the 10 doubly doped configurations. The uncertainty of the position is similarly calculated as:

$$\sigma = \sqrt{\sum_i p_i (z_i - \mu)^2} \tag{5.4}$$

Similar to determining the number of dopants in a column, the combined detector information is treated as a compound probability of independent events, and the respective values of $norm_i^c(t)$ for both detectors are multiplied together in Eqn. 5.2, with all subsequent calculations the same. An example calculation for the dopant depth is given in Table E.2 of Appendix E.

Just as we calculated the number of dopants in a column (Fig. 5.9), we also calculate the dopant position and uncertainty for an experimental point that lies at each simulated position, incorporating the experimental error function. By knowing in advance the location of the dopant, we are able to see how the uncertainty and accuracy is affected by the different detector settings for the different dopant configurations. Figure 5.10 visually depicts the results from two cases, a single (a) and doubly doped (b) column, respectively. The positions (points) and uncertainties (bars) for each configuration are indicated next to the structural model, in yellow, for both the individual detectors as well as for the combined detector information.

For the single doped column in Fig. 5.10(a), we see that using detector 1, the closest calculated position is incorrect, while the uncertainty range spans three different atomic positions. Detector 2, meanwhile, gives the correct calculated position with a smaller uncertainty that does not overlap any other nearby positions for the same case. In other dopant configurations, however, the reverse may be true: detector 1 could give the correct position and/or smaller uncertainties. In Fig. 5.10(b), we see that once again, detector 2 has a smaller uncertainty than detector 1, although this time, the results from both detectors span multiple atomic positions. The closest calculated position using detector 1 is also incorrect.

The third column in Fig. 5.10 shows the results from treating each detector as an independent measurement and combining their probabilites together. We see a significant reduction in the uncertainty for both configurations, as well as more accurate measure-

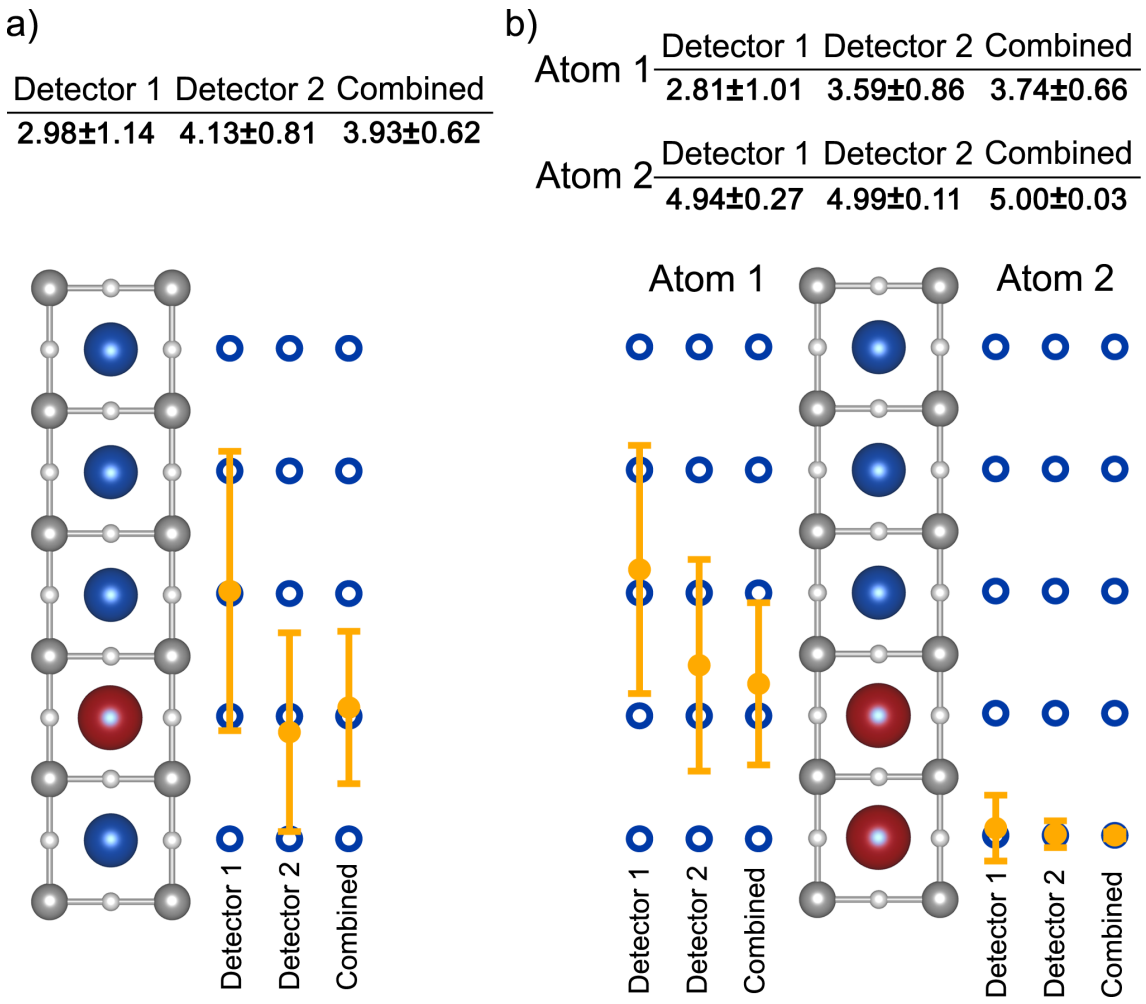

Figure 5.10: Calculated positions and uncertainties for (a) a single dopant located at position *4* and (b) two dopants located at positions *4* and *5*. From left to right, filled yellow points and error bars represent the position and uncertainty of detector 1, detector 2, and the combined detector information, respectively. For (b), both atom positions and uncertainties are given and plotted separately. Figure reproduced from Ref. [45].

Performance Comparisons of Individual and Combined Detectors

	1 Dopant				2 Dopants			
	Detector 1	Detector 2	Combined	Improvement	Detector 1	Detector 2	Combined	Improvement
Config. Prob.	38.2%	45.1%	57.4%	27%	22.8%	31.4%	44.6%	42%
Uncertainty	1.06	0.78	0.68	13%	0.73	0.61	0.54	11%
Avg. Error	0.67	0.48	0.35	27%	0.47	0.44	0.33	25%
% Correct	35.7%	44.3%	52.6%	19%	51.0%	55.6%	63.5%	14%
% In Range	67.8%	58.4%	70.3%	4%	69.5%	62.7%	71.1%	2%

Table 5.2: Performance metrics for detector 1, detector 2, the combined detectors, and the improvement of the combined detector over the best performing single detector, grouped by number of dopants in the column. Row 1 indicates the configurational probability of the actual dopant position. Row 2 indicates the uncertainty range (standard deviation) of the calculated position. Row 3 indicates the distance between the calculated position and the actual position. Row 4 indicates the percent of data points (out of 100,000 simulated points) that, when rounded to the nearest position, are correctly identified. Row 5 indicates the percent of data points that are within the uncertainty range of the calculated position. Table reproduced from Ref. [45].

ments.

5.8.1 Performance Metrics

There are many possible metrics to judge how well each detector performs. We consider the following:

- Configurational probability - the calculated probability of the *actual* position of the dopant, with a higher value being better
- Uncertainty - the average uncertainty, or standard deviation (Eqn. 5.4) of the calculated position, with a lower value being better
- Average error - the difference between the calculated position of the dopant and the *actual* position, with a lower value being better

These metrics are summed up in the first three rows of Table 5.2, as an overall *average* across all 15 dopant configurations, grouped separately for single and doubly doped atomic columns. The improvement column in Table 5.2 indicates the percent increase from using the combined detector information over the best performing single detector for that particular metric. We see that the combined detector probabilities results in a substantial improvement across all three performance metrics mentioned above. The last two rows involve Monte Carlo-type simulations and are discussed below.

5.8.2 Additional Simulations

To this point, all the experimental data points used for the calculations have been placed at the simulated positions (Fig. 5.7). Real measured data points will not just be located at these discrete positions, however, but could lie anywhere in I_{Sr} vs. I_{Ti} space. To simulate this experimental scatter more realistically, we generated 100,000 data points around each simulated location, using the experimental error function to determine the data point location. We then perform the same calculations for determining the expected atom position and uncertainty at each of these generated data points. From these calculations, we can introduce two additional performance metrics:

- % Correct - the percentage of simulated data points (generated based on the experimental error function) around each dopant configuration which results in a calculated position that matches the actual position (higher percentage is better), and

- % In range - the percentage of simulated data points (generated based on the experimental error function) around each dopant configuration which results in a calculated position that lies within the uncertainty range of the actual position (higher percentage is better).

These two metrics are summarized in the bottom two rows of Table 5.2, as an average over all 15 dopant configurations, for the individual and combined detector settings. Results from each individual dopant configuration are listed in Table E.2 of Appendix E.

From Table 5.2, we see that the improvement in the number of correctly determined simulated data points using the combined detector settings is significant: 19% for 1 dopant and 14% for 2 dopants. The improvement from the data points that lie within the uncertainty range of the actual position is much more modest ($\sim$ 3%), but this is because the uncertainty range is being simultaneously lowered. Nonetheless, simultaneously reducing both the uncertainty range and the average error results in a better likelihood of unambiguously determining a single most likely dopant configuration. At the same time, the calculated result is more likely to be correct.

Finally, we note that while we observe a simultaneous improvement in both the overall precision and accuracy of dopant depth determination by using the combined detector probabilities, Table 5.2 only summarizes the results averaged over all possible dopant configurations, and individual configurations can vary in terms of visibility and ease of determination. For example, the percentage of simulated data points correctly identified as the actual dopant position can vary from near perfect (99.9% for the *4,5* configuration using the combined detector) to undetectable (0% for configuration *1* using detector 2), as tabulated in Table E.2. These calculations help provide a realistic idea of which configurations can be most successfully resolved, and by using which detector settings. Therefore, once an experimental dopant is measured and its position calculated using the analysis detailed above, Table E.2 can be used to determine a confidence level for that calculation.

5.9 Experimental HAADF

The experimental data shown in Fig. 5.6(a) was analyzed and filtered using custom MATLAB scripts to find doped atomic columns in regions appropriate for the current study: 5 u.c. thickness and local uniformity. Figure 5.11 shows HAADF images from two such regions in the Gd-doped $SrTiO_3$ sample. Each region was imaged using two different detector settings in succession ($\sim$ 36 s apart), and aligned by eye based on common features, such as thickness variations or edge features. The lateral offset between the images from an eye-based alignment matched well with drift estimates based on the drift present in each image, as well as prior drift tracking using multiple image acquisition. Due to contrast differences between the different detector settings, not every bright Gd-containing column in one detector setting will result in an equally bright column in the other setting.

The white squares/triangles in Fig. 5.11(a) indicate the two Gd-containing columns in each image that are analyzed here to determine the effectiveness of using multiple detectors. These atomic columns are plotted in I_{Sr} vs. I_{Ti} space for the two detectors in Figure 5.11(b), using corresponding black squares/triangles. The simulated dopant configurations are also shown and labeled, while a dashed line indicates a linear fit to the undoped $SrTiO_3$. We can see that qualitatively, while the doped column marked by the triangle appears to be at position *4* using detector 1, it seems much more likely to be at position *3* when taking into account detector 2. Similarly, the dopant marked by the square is also close to positions *3* and *4* using detector 1, but is more likely to be located at *4* when taking both detectors into account.

The calculation for the number of dopants and dopant depth position for both regions in Fig. 5.11 is given in Table 5.3. The left side of the Table shows the calculated probabilities of the possible number of dopants using each detector, and with the combined

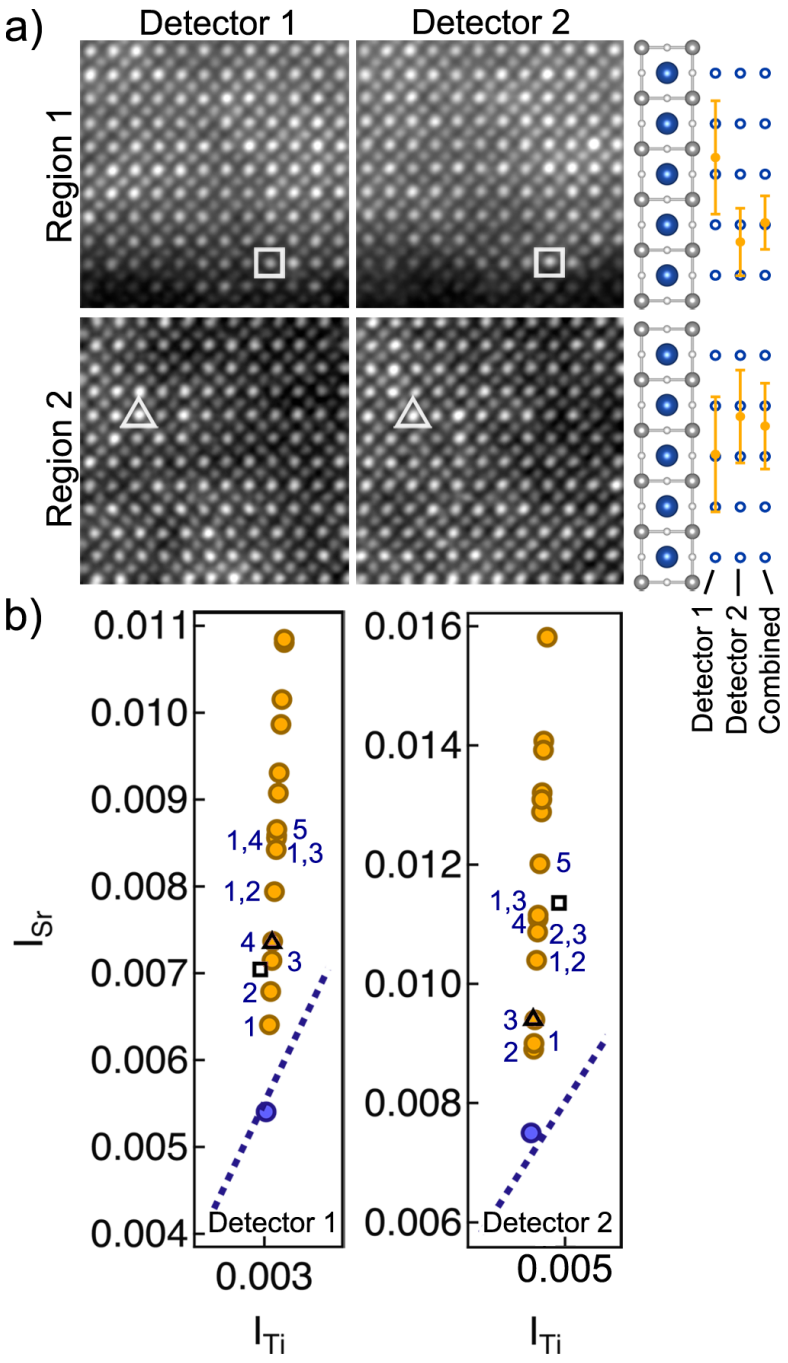

Figure 5.11: (a) HAADF STEM images of two regions containing dopant atoms in Gd-doped $SrTiO_3$ for detector 1 (left) and detector 2 (right). White squares/triangles indicate the doped column of interest. A low band pass filter was applied to the images. The quantitative analysis was performed on the unfiltered, raw data. (b) Simulated I_{Sr} vs. I_{Ti} dopant configurations compared to experimental values shown in (a). Selected dopant configurations are labeled for each detector. Figure reproduced from Ref. [45].

Summary of Probabilities for Experimental Dopant Number and Positions

# Dopants	Detector 1	Detector 2	Combined	Detector 1		Detector 2		Combined	
				Position	Probability	Position	Probability	Position	Probability
0	5.1%	0%	0%	5	0.0279	5	0.4179	5	0.0742
1	64.9%	49.5%	78.7%	4	0.2491	4	0.5311	4	0.8429
2	30.1%	50.5%	21.3%	3	0.2734	3	0.0340	3	0.0592
				2	0.2607	2	0.0071	2	0.0118
				1	0.1889	1	0.0099	1	0.0119
Region 1				**2.67±1.12**		**4.34±0.67**		**3.96±0.53**	
0	1.5%	4.8%	0.2%	5	0.0692	5	0.0026	5	0.0008
1	57.3%	63.8%	73.1%	4	0.2978	4	0.0441	4	0.0605
2	41.1%	31.3%	26.8%	3	0.2861	3	0.3489	3	0.4599
				2	0.2202	2	0.2929	2	0.2970
				1	0.1267	1	0.3115	1	0.1818
Region 2				**2.96±1.14**		**2.21±0.92**		**2.40±0.85**	

Table 5.3: Calculated probabilities for the number and location of dopants for the two atomic columns marked by squares (region 1) and triangles (region 2) in Fig. 5.11. Table reproduced from Ref. [45].

detector information, while the right side shows the individual probabilities of where the dopant is located in the column, *given* the number of dopants that had been previously determined. The expected value and uncertainty is calculated in both regions for each detector, and is graphically plotted on the right side of Fig. 5.11(a).

For the doped column in region 1 (square), we see that detector 2 alone would not have been able to distinguish between 1 or 2 dopants, while the probability from the combined detectors is much more convincing, indicating a single dopant atom with 78.7% probability. Meanwhile, detector 1 alone would have calculated an incorrect position (assuming the correct position is *4*, which seems most likely). Both detectors, when analyzed individually, also had large uncertainties that spanned multiple dopant positions. By using the combined detector information, however, the uncertainty in the probability measurements is significantly reduced, and only one position falls within the uncertainty range. According to Table E.2, a single dopant in this position has a 72.7% chance of yielding a calculation within the correct uncertainty range.

The results from the analysis of the column in region 2 is similar, with reduced uncertainties using the combined detector information, although the final result from both detectors still yields two possible dopant positions (*2* or *3*). From visual inspection of Fig. 5.11(b), however, position *3* seems more likely.

5.10 Summary and Conclusions

To summarize, we have shown significant improvements in precision *and* accuracy in the 3D determination of dopant depth information by using variable-angle HAADF imaging combined with quantitative STEM. The use of variable angles has been shown to improve both the accuracy and precision of the number of dopants, as well as their position, the latter of which is a conditional probability, calculated once the number of

dopants is determined. We have demonstrated this improvement using both simulations and experimental data. Using multislice simulations, we showed that the difference in atomic scattering by dopant atoms at different depths can be exploited by selecting different angular regions on the same detector. While one particular detector is not unilaterally better than the other, the acquisition of multiple detector data (angular regions) and the use of compound probabilities will significantly improve dopant visibility and quantification.

In general, configurations that are ambiguous or difficult to determine in one detector regime can be resolved in the other. For example, given the experimental noise of the present study, the probability of determining the correct number of dopants was $> 63\%$ for all sixteen possible configurations (including zero dopants) when using both detector information, while only 18/32 (56%) configurations met that requirement for a single detector. In addition, the calculated position is $\sim 17\%$ more likely to be the actual position, since calculated positions from a single detector can be erroneous, even when the uncertainty is small.

5.10.1 Outlook

The present study only used two angular regimes due to practical experimental constraints, but it was sufficient to prove the usefulness of VA-HAADF, even with the angular regimes not being specifically optimized for the experiment. Going forward, we propose that the method can and should be extended to include additional angular ranges, which is limited only by the detector hardware limitations, and to remain within the HAADF imaging regime to retain the analytical benefits of HAADF. As shown in Fig. 5.7, different angular ranges can have dramatic effects on the scattered intensities of a specific atomic configuration. Furthermore, the development of VA-HAADF using a parallel ac-

quisition mode would provide many additional benefits, such as minimization of drift between acquisition that makes locating the same area difficult in the absence of apparent features, avoiding beam damage caused by multiple exposures from serial acquisition, and avoiding changing the sample in subtle ways between acquisitions, such as changes in the amorphous layers or surface/impurity atom hopping. To that end, the development and implementation of new hardware, such as segmented [178, 187, 188, 189] or pixelated [190, 191] HAADF detectors is paramount. Such detectors would be necessary to implement VA-HAADF for any number of detectors and angular ranges with parallel input, but would still need to have the response characteristics required for quantitative HAADF-STEM [69]. We highlight again that VA-HAADF provides a new way to obtain complementary information about the structure of a material, which is useful not only for dopant depth identification, but would also serve to generally improve STEM image contrast and improve interpretability for the analysis of strain, defects, and enhanced structural information.

Chapter 6

Summary and Outlook

Deciphering the relationship between the structure and properties of a material is a fundamental tenet of materials science. Through characterization, we can analyze a material's atomic structure and elemental composition, and track how structural changes affects the macroscopic properties, and ultimately, the performance of the material. In this dissertation, I used new methods in scanning transmission electron microscopy (STEM) to locally characterize oxygen octahedral tilts in complex oxide thin films at the atomic level, a long-sought goal in condensed matter physics. While oxygen octahedral are notoriously difficult to characterize, and are not directly observable in HAADF STEM, I used a combination of real-space imaging and reciprocal-space diffraction to characterize the oxygen octahedral tilts in thin perovskite films grown by molecular beam epitaxy. The effect of octahedral tilts on the structure and properties in three separate materials systems were studied in this dissertation.

While determining structure-properties relationships is a central goal of materials scientists, characterization techniques are the tools to examine the structure of those materials. Recent advances in theory and hardware of transmission electron microscopy have made the TEM a widely popular tool for atomic structure characterization, with quantitative studies now routine. In this dissertation, I also developed a new procedure for improving image contrast in quantitative STEM by using multiple detectors, and

applied it to increase the precision and accuracy of determining the depth of dopant atoms from a 2D image.

The goals and questions addressed from these four main studies are listed below.

1. $SrTiO_3$ quantum wells grown between $GdTiO_3$ and $SmTiO_3$, and how the metal-insulator transition is related to the quantum well thickness.

2. $GdTiO_3$ quantum wells grown between $SrTiO_3$, and how the magnetic properties are affected by the quantum well thickness.

3. $NdNiO_3$ thin films strained in tension and compression, and what drives the metal-insulator transition as a function of temperature.

4. Gd-doped $SrTiO_3$, and improvement of the precision and accuracy of dopant depth determination using quantitative STEM.

I now summarize the individual projects that have been covered in this thesis, their results and possible future outlook. In Chapter 1, I introduced the multifaceted perovskite system, which contains an incredibly diverse set of properties and structural variations. Its chemical flexibility and ability to accommodate nearly all the elements in the periodic table makes it one of the most studied compounds in materials science and solid state chemistry. Among perovskite oxide subgroup, small distortions of the prototypic cubic structure can lead to significant effects on the electrical and magnetic properties, due to strong electron-lattice coupling. In particular, octahedral tilts and rotations are the most common type of distortion that occurs, and corner connectivity requirements offer researchers exciting possibilities to tailor the materials' properties using epitaxial constraints. While these tilts are difficult to measure on a local level, we outline an approach using new transmission electron microscopy methods to obtain local atomic-level

information on octahedral tilts. Such new characterization techniques are critical for understanding the underlying physics of complex oxide interfaces, and would help promote new ways to create functional materials systems through materials selection and design.

In Chapter 2, we studied the role of extreme electron density on the electrical and structural properties of $SrTiO_3$ quantum wells. $SrTiO_3$, embedded between the rare-earth compounds $GdTiO_3$ and $SmTiO_3$, contain a confined, high-density ($\sim 6 \times 10^{14}$ cm^{-2}) two-dimensional electron gas (2DEG). As the thickness of the $SrTiO_3$ quantum well is reduced, and the 2DEG is shared between fewer and fewer layers of TiO_2, different electrical properties emerge from the quantum wells grown between $GdTiO_3$ and $SmTiO_3$. Quantum wells embedded in $GdTiO_3$ show a metal-insulator transition when the $SrTiO_3$ thickness is reduced to two SrO layers and below, while quantum wells embedded in $SmTiO_3$ remain metallic even at a single SrO layer. Using HAADF STEM to measure Sr-column displacements in the quantum wells, we characterized a deviation angle, θ, which represents a symmetry-lowering distortion from the normally cubic bulk $SrTiO_3$ structure. We found that a structural distortion was present in the quantum wells that became insulating, but was absent or very weak in all quantum wells that were metallic, regardless of whether embedded in $GdTiO_3$ or $SmTiO_3$. These results indicate the importance of the "orthorhombic-like" distortion in promoting the insulating state. The electron-electron interactions in the quantum wells should be similar for the same thickness $SrTiO_3$, regardless of the surrounding material, which points to more complex physics, such as orbital order, influencing the structure in the quantum wells.

In Chapter 3, we used the same techniques from Chapter 2 to study the structure and magnetic behavior of ferrimagnetic $GdTiO_3$ thin films sandwiched between cubic $SrTiO_3$. Specifically, we relate the cation displacements measured in STEM to the oxygen octahedral tilts, observable by position averaged convergent beam electron diffraction (PACBED), and attempted to tailor the structure of bulk $GdTiO_3$ by interfacing it with

$SrTiO_3$. We saw that by decreasing the $GdTiO_3$ film thickness, $GdFeO_3$-type structural distortions were reduced, concomitant with a reduction in the Curie temperature, until the films became non-ferrimagnetic. Comparing the structure of the $GdTiO_3$ films to the structure of the bulk rare-earth series, we saw that ferrimagnetism persisted in the films to smaller deviations from the cubic perovskite structure than expected. These results indicate that the ferrimagnetic ground state only depends on the amount of the $GdFeO_3$-type distortion to second order, and is controlled by the narrow bandwidth, exchange and orbital ordering model.

In Chapter 4, we explored the different electrical behavior in strained $NdNiO_3$ films, and their relationship with the lattice symmetry as a function of temperature and strain, to arrive at new insights into the nature of the MIT in the rare-earth nickelates. Bulk $NdNiO_3$ undergoes a temperature-driven metal-insulator transition, which can be controlled by epitaxial strain. In tensile strained films, the temperature of the MIT is lowered as the strain increases, until films become insulating at all temperatures for large tensile strains, whereas compressively strained films, above a minimum thickness, remain metallic at all temperatures. Using low-angle position averaged convergent beam electron diffraction in a scanning transmission microscope, we characterize the structure of compressive and tensile strained $NdNiO_3$ films above and below the MIT temperature. We find that even at room temperature, the epitaxial strain affects the film space group symmetry and octahedral rotations, to be different than those of bulk orthorhombic $NdNiO_3$. We also show that the MIT, which only occur in the tensile strained films, is associated with a symmetry-lowering structural distortion. Compressively strained films, which do not undergo an MIT, do not show a symmetry change at low temperatures. From space group symmetry analysis, we show that the present results support the charge-disproportionation model for explaining the MIT in rare earth nickelates, and present a simple geometric argument to explain the metallic behavior of compressively strained

$NdNiO_3$ films. The results could also provide additional insight into the non-Fermi liquid phase observed in these films.

In Chapter 5, I discuss a new technique for improving general contrast in transmission electron microscopy, variable-angle high-angle annular dark-field (VA-HAADF) imaging. Here, we analyzed Gd-doped $SrTiO_3$ films, where the Sr columns contained from zero to two Gd dopant atoms, and imaged them in HAADF mode using two different detector collection angles. We showed that VA-HAADF significantly increased the precision and accuracy of 3D dopant depth determination, from both image simulations and experimental results. By using compound probabilities of the combined information from multiple detectors, calculations of the dopant depth position is less prone to error, and the uncertainty in the dopant depth is significantly reduced. Certain atomic configurations that are indistinguishable with a single detector setting can be uniquely identified using VA-HAADF. While developed in this dissertation for precise and accurate determination of three-dimensional dopant atom configurations using a single quantitative zone-axis STEM image, VA-HAADF can be extended to wider general applications where enhanced STEM contrast and atom visibility is needed.

The work in this dissertation have resulted in several important findings about the driving forces behind metal-insulator transitions in oxides. Many unanswered questions still remain, however, such as the different electrical behavior between $SrTiO_3$ quantum wells sandwiched between $GdTiO_3$ and $SmTiO_3$. Such questions are beyond our present capability to answer, and underscore the rich complexity in these systems. By correlating cation displacements with octahedral tilts, however, we have enabled new ways for researchers to locally quantify these difficult to observe tilt patterns in the future. In addition, our use of LA-PACBED to determine structural transitions in the $NdNiO_3$ system offers a demonstration of the capabilities of STEM diffraction to extract difficult to determine structural information, particularly in experimentally unstable conditions,

such as those from using a liquid nitrogen cryo holder. Newer electron sources should also improve the gun brightness, and thus allow us to further decrease of the convergence angle (less disc overlap and potentially more information) without a loss in spatial resolution.

Finally, I would like to highlight the successful implementation of VA-HAADF in improving the depth resolution of dopants from the last study. Although the demonstration in the current thesis contains many experimental inefficiencies (such as serial acquisition and a single HAADF detector), we have provided clear proof-of-concept of the many advantages the technique can provide. While parallel improvements in STEM hardware, such as brighter guns and more stable holders, can also provide a similar increase in image contrast, such improvements are becoming incrementally more difficult, while new detector designs have been mostly untapped. As such, we reiterate the importance of the development of hardware to take advantage of the angular dependence of electron scattering for detector manufacturers. Future capabilities from improved detectors could include vacancy imaging, improved knowledge on chemical composition, or enhanced strain contrast. Meanwhile, the VA-HAADF technique can be incorporated into existing systems, and introduces a new avenue for continuing STEM contrast improvement and pushing the boundaries of quantitative STEM.

Appendix A

PACBED Formation

Position averaged convergent beam electron diffraction (PACBED) patterns are formed by incoherently summing CBED patterns over many different probe positions within the unit cell (experimentally by scanning the beam during diffraction pattern acquisition). This incoherent averaging destroys the fine detail present in the coherent interference of the original pattern, but benefits from better count rates (lower noise) and reduced sensitivity to instability (specimen drift).

The formation of CBED patterns is well understood and can be readily simulated following numerous approaches [192, 38]. The basic image formation process is described below.

Starting from the Schrödinger equation for fast electrons (using the relativistic mass and wavelength of electron):

$$\frac{\partial\psi(x,y,z)}{\partial z} = [\frac{i\lambda}{4\pi}\nabla^2_{xy} + i\sigma V(x,y,z)]\psi(x,y,z) \tag{A.1}$$

where $\psi(x,y,z)$ represents the electron wavefunction that varies slowly with z (distance into the sample), λ is the relativistic wavelength of the incident electron, σ is the interaction parameter (describes degree of interaction between electron and potential, decreases with increasing electron energy), and $V(x,y,z)$ is the specimen potential.

Following the multislice formulation [38], the formal operator solution can be written as:

$$\psi(x, y, z + \Delta z) = exp[\frac{i\lambda}{4\pi}\Delta z \nabla^2_{xy} + i\sigma v_{\Delta z}(x, y, z)]\psi(x, y, z) \tag{A.2}$$

where $v_{\Delta z}(x, y, z)$ is the projected potential of the specimen between z and $z + \Delta z$.

Equation A.2 can be rewritten in discretized form (conducive for computer computation) by taking the Fourier transform:

$$\Psi(\mathbf{g}, z + \Delta z) = \sum_{\mathbf{h}} \mathbf{S}_{\mathbf{g},\mathbf{h}}(z)\Psi(\mathbf{h}, z)) \tag{A.3}$$

where Ψ represents the reciprocal space wavefunction, $\mathbf{g}, \mathbf{h}$ are reciprocal lattice vectors of the sampling mesh used in the computer calculation, and $\mathbf{S}$ is the Fourier transform of the exponential term in equation A.2, now represented as the so-called scattering matrix [193, 192].

The incident wavefunction of the electron probe can be represented as a plane wave, or in reciprocal space:

$$\Psi(\mathbf{h}, z = 0) = A(\mathbf{h})exp[-i\chi(\mathbf{h})]exp[-2\pi i \mathbf{h} \cdot \mathbf{R}] \tag{A.4}$$

where $\mathbf{R}$ is the position of the probe, $A(\mathbf{h})$ is the aperture function (1 inside the aperture, 0 outside) and $\chi(\mathbf{h})$ is the aberration function of the objective (probe-forming) lens.

Using equations A.3 and A.4, the intensity, I, of the CBED pattern for a certain probe position $\mathbf{R}$ is:

$$\begin{aligned} &I(\mathbf{q}_l + \mathbf{G}, \mathbf{R}, t) \\ &= \left| \sum_{\mathbf{H}} S_{\mathbf{G},\mathbf{H}}(\boldsymbol{q}_l, t) T(\mathbf{q}_l + \mathbf{H}) exp[-2\pi i(\mathbf{q}_l + \mathbf{H}) \cdot \mathbf{R}] \right|^2 \end{aligned} \tag{A.5}$$

where $\boldsymbol{q}_l$ represents a vector in the first Brillouin zone, $\boldsymbol{G}$ and $\boldsymbol{H}$ represent non-zero reciprocal lattice vectors (Fourier transform of $\mathbf{g}$ and $\mathbf{h}$ respectively), and $T() = A()exp[-i\chi()]$, the complex amplitude of the incoming probe.

By integrating equation A.5 over all positions in the unit cell, the average intensity, $\bar{I}$, in the PACBED pattern can by calculated by:

$$\begin{aligned} &\bar{I}(\mathbf{q}_l + \mathbf{G}, t) \\ &= \frac{1}{A_c} \int_{A_c} I(\mathbf{q}_l + \mathbf{G}, \mathbf{R}, t) d\mathbf{R} \\ &= \sum_{\mathbf{H}} |S_{\mathbf{G},\boldsymbol{H}}(\boldsymbol{q}_l, t) T(\mathbf{q}_l + \mathbf{H})|^2 \end{aligned} \tag{A.6}$$

where A_c represents the area of the unit cell.

An important feature from this equation is that the features in PACBED patterns are independent of the probe-forming lens aberration as well as spatial coherence, or finite effective source size. Equation A.6 models the propagation of waves through the sample, and only describes the elastic contribution to the PACBED pattern. Inelastic scattering can be included in Bloch wave simulations as an absorption effect by adding an imaginary component to the crystal potential [193, 194]. In multislice implementations, diffuse thermal scattering can be accounted for by using the frozen phonon model. For a description of the different simulation methods, see Appendix B. In practice, thermal scattering results in the addition of an inelastic background across the diffraction pattern. This background contribution has some partial structure, which is most familiarly seen in Kikuchi patterns. However, most of the useful identifiable features in PACBED patterns are dominated by elastic scattering.

Although PACBED patterns are independent of lens aberrations, the convergence angle plays a critical role in the formation of the patterns. Larger convergence angles

(∼20 mrad) result in larger diffraction discs, which causes disc overlaps that wash out the features of interest [40]. Due to this limit in the convergence angle, PACBED is best suited for non-aberration corrected STEM. In practice, PACBED patterns can be taken by rapidly scanning the STEM probe in the TEM while acquiring the diffraction pattern using the CCD camera with a long exposure time (several seconds).

Appendix B

Simulation Approaches

The two most popular methods for simulating TEM images and diffraction patterns are Bloch wave and multislice methods. Both methods incorporate dynamical (multiple) scattering.

B.1 Bloch Waves

The Bloch wave method, as formalized by Bethe [195], involves Fourier expanding the crystal potential and electron wavefunction to components (Bloch waves) that match the underlying specimen lattice periodicity. By applying the appropriate boundary conditions and solving for the eigenvalues of the Bloch wave coefficients, the exit wavefunction can be obtained by the linear superposition of the different Bloch waves.

While Bloch wave solutions can provide valuable insight on the imaging process, contain information about all thicknesses in the same calculation, and can be solved by hand for a small number of Fourier components, N (a.k.a. beams or Bloch waves), the computer memory requirements scale as N^2 while computer time scales as N^3 [38]. Real specimens requiring large N quickly makes solving the matrix solutions impractical, even for a computer.

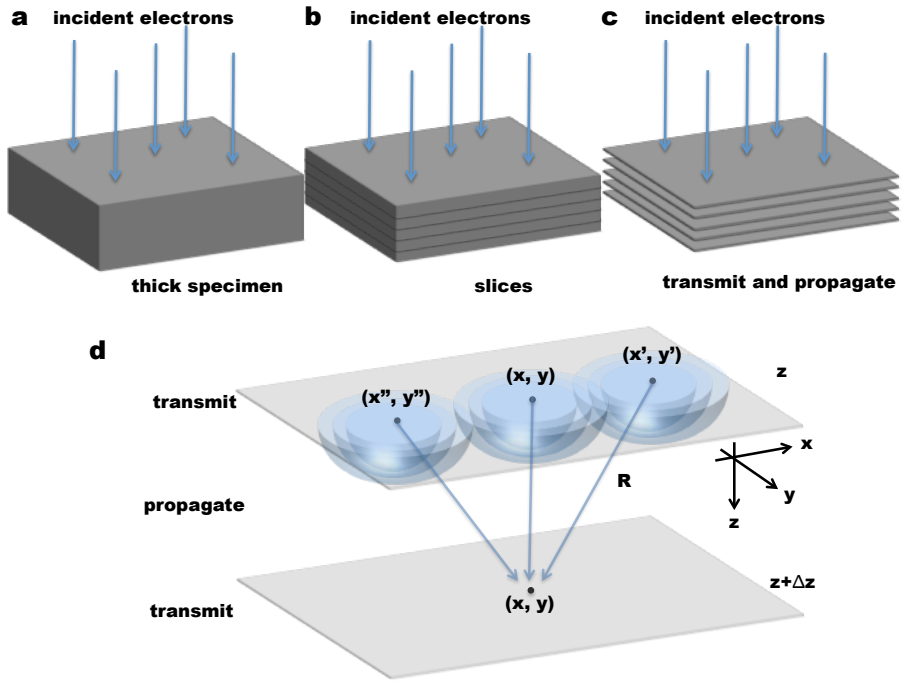

Figure B.1: Decomposition of a thick specimen by the multislice method. (a) Original thick specimen, (b) specimen divided into thin slices, where (c) each slice is treated as a transmission step followed by a propagator (vacuum between slices). (d) Optics interpretation of the multislice propagator. The wavefunction in the x, y plane at height z propagates to the x, y plane at $z + \Delta z$. Each point on the wavefront at z emits a spherically outgoing wave, all of which combine at each point in the x, y plane at $z + \Delta z$.

B.2 Multislice

The multislice method, first developed by Cowley and Moodie [196], is graphically represented in Figure B.1. The original specimen is divided into thin, two-dimensional slices along the electron beam direction, Fig. B.1(a-c). The incident electron beam in an x, y plane is alternately transmitted through a slice and propagates along z, through vacuum, to the next slice (by Fresnel diffraction). Each slice is represented by a transmission function (projected atomic potential from z to $z + \Delta z$), and is thin enough to be considered a simple phase object. Additionally, each slice along the beam direction does not have to be the same thickness or follow the periodicity of the original specimen,

allowing the simulation of amorphous and defect structures. The propagator function $p(x, y, \Delta z)$ can be associated with Fresnel diffraction over the distance Δz. Figure B.1(d) shows the classical optic interpretation of this propagation. Every point on a wavefront (position z) generates an outgoing spherical wave, which propagates to the position of the next wavefront ($z + \Delta z$) and interferes with one another.

The multislice method makes use of the Fast Fourier Transform (FFT) algorithm, which greatly increases its efficiency. Storage requirements for the multislice method scales as N, while the computer time scales as $Nlog_2N$ [38], making it usually much more efficient for calculating dynamical images and diffraction patterns.

B.3 Frozen Phonon

In actual experiments, usually conducted at room temperature, thermal energy causes the atoms in the specimen to slightly vibrate from their equilibrium positions. These vibrations are quantized as phonons, and lead to a diffuse background intensity in the diffraction pattern between the normal allowed diffraction positions (reciprocal lattice points). This is referred to as thermal diffuse scattering (TDS).

Typical electrons in a TEM travel at relativistic speeds ($\sim 1.5 \times 10^{10}$ cm/s) and take only about 0.7×10^{-16} s to travel through a typical thickness sample [38]. This is a much smaller time than the period of oscillation of each atom due to thermal vibrations (typical phonon frequencies are $\sim 10^{12} - 10^{13}$ Hz). Hence, each imaging electron can be approximated as seeing a different configuration of atoms, each atom slightly displaced due to TDS. Because the atoms in each configuration are not correlated in their movement, an incoherent time average over all atomic configurations can be done to model the effect of TDS in the image. This can be incorporated into multislice simulations by randomly offsetting the position of each atom using a Gaussian distribution, and is

known as a frozen phonon simulation.

Due to this Monte Carlo style integration, the frozen phonon model is computationaly demanding, but is generally considered the most theoretically realistic [192, 197]. Despite only modeling elastically scattered electrons, Van Dyck has shown that it is equivalent to a full quantum-mechanical treatment of the inelastic phonon scattering process [198].

B.4 Simulation of Non-orthogonal Structures

A caveat of using FFT is that the structure being transformed must have orthogonal axes. While this is the case for $[100]_O$ $GdTiO_3$ (and all P*bnm* space groups), it is not the case for $[110]_O$, due to the different **a** and **b** unit cell parameters [forms 86.93° angle between [110] and $[\bar{1}10]$, Figure B.2(a)]. Figure B.2(a, b) illustrates the transformation matrixes needed to orient the orthorhombic *c*-direction along $[110]_O$ as well as the geometry to derive the equations given in B.1. From B.1, the transformation from the original black axes to the desired red axes can be carried out through a 2-step matrix multiplication, given by equation B.2. The second transformation matrix in B.2, to go from the **a** to **a'** axes can be obtained through inspection.

$$\begin{aligned} a'' &= |z|\,a' - \tfrac{|y|}{|c'|} & |x| &= |a'|\,cos\beta \\ |y| &= \tfrac{x}{sin\beta} = |a'|\,cot\alpha & |z| &= \tfrac{|a'|}{cos\alpha} \end{aligned} \tag{B.1}$$

$$\begin{pmatrix} a'' \\ b'' \\ c'' \end{pmatrix} = \begin{pmatrix} \frac{1}{cos\alpha} & 0 & -\frac{|a'|}{|c'|}tan\alpha \\ 0 & 1 & 0 \\ 0 & 0 & 1 \end{pmatrix} \begin{pmatrix} -1 & 1 & 0 \\ 0 & 0 & 1 \\ 1 & 1 & 0 \end{pmatrix} \begin{pmatrix} a \\ b \\ c \end{pmatrix} \tag{B.2}$$

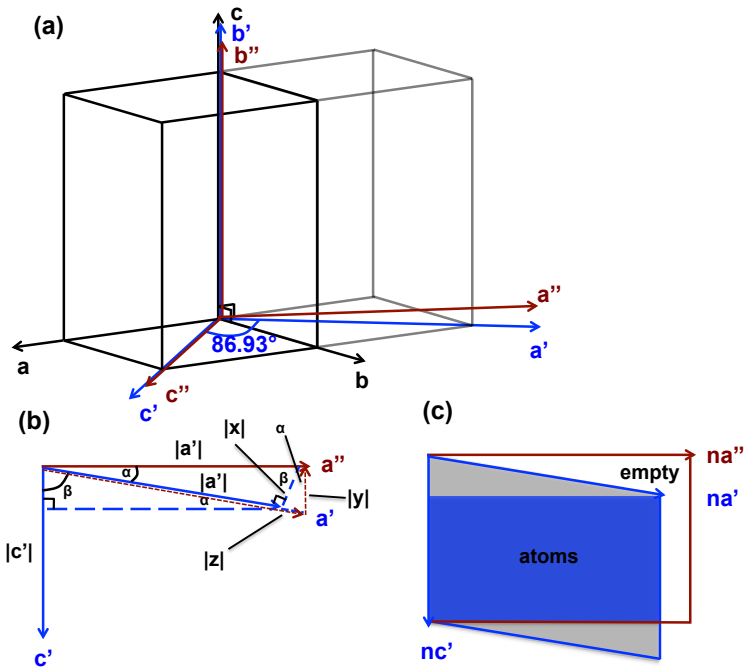

Figure B.2: (a) Diagram of orthorhombic unit cell showing the original axes (black), intermediate axes with $[110]_O$ as c-direction (blue, prime), and final orthogonal axes (red, double-prime). (b) Geometry of axes transformation from blue (prime) to red (double-prime). β angle corresponds to 86.93° shown in (a). (c) Creation of supercell followed by matrix transformation results in empty space (white area) under final axes coordinates. Supercell needs to be subsequently limited (blue region for orthogonality) to the grey area. Angles have been exaggerated for illustration purposes.

While these transformations create the necessary orthogonal conditions, the unit cell is no longer translatable under these new coordinate axes. Using the original unit cell would result in larger and larger errors as the thickness or repeat number increases. Therefore, a supercell of many unit cells must be created prior to transformation. After transformation, this supercell contains empty space along the edges, as illustrated by the *ac* plane shown in Figure B.2(c). Only the areas marked in grey contain atoms, so the supercell needs to be cut to within the marked blue region. All $[110]_O$ PACBED patterns in this thesis were calculated this way. This process results in the inability to quickly generate a large thickness series of PACBED patterns along $[110]_O$, as each thickness must created as a superstructure manually, and calculated wavefunctions cannot be saved between thickness slices.

Appendix C

Generating Structures for PACBED

C.1 Introduction

Position averaged convergent beam electron diffraction (PACBED) is a scanning transmission electron microscopy (STEM) technique used to determine TEM specimen thickness and tilts [40] as well as local structural information [127, 16, 72]. PACBED formation is well understood and can be simulated using a number of available software. In this thesis, we use the Kirkland program suite [38].

Many of the physical properties exhibited by ABO_3 perovskite oxides are resultant from distortions or rotations of the BO_6 octahedra. A great deal of effort has been placed into characterizing these rotations [34, 17, 32, 199], but accurate knowledge of octahedral rotations, especially at the local level, remains challenging. Previous experiments [16, 72] have successfully utilized PACBED in characterizing local octahedral tilts, by comparing experimental patterns with a series of simulated structures. Generating such structures is the focus of this Chapter.

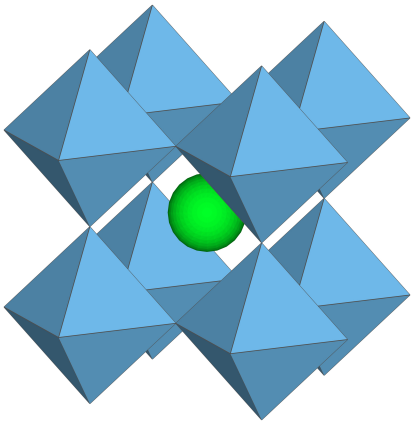

Figure C.1: Ideal perovskite unit cell is composed of corner connected octahedra.

C.2 Octahedral tilts

The ABO_3 perovskite unit cell is composed of corner connected BO_6 octahedra; the ideal unit cell structure is shown in Fig. C.1. Most perovskites, however, feature one of three main distortions: displacements of the cations, distortions of the octahedra, and most commonly, tilting of the corner-connected octahedra. A common classification of the different tilt types in perovskites is the Glazer notation [22], which classifies structures according to the octahedral rotation around its three tetrad axes (see Fig. C.2.) Due to corner-connectivity constraints, tilting of one octahedron in a unit cell will determine the tilts of the other octahedra in the crystal.

C.2.1 Generating structures with octahedral tilts

A custom MATLAB code was written to generate the most common tilt type (orthorhombic $a^+b^-b^-$), although it can also be easily tailored to generate any other rotation type. In general, an octahedron tilting about one of its cartesian axes will expand the unit cell along the perpendicular axes (and the parallel one, depending on if it's an in-phase

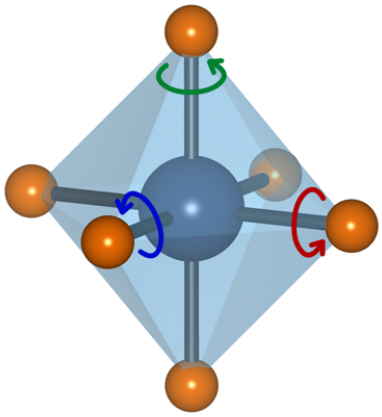

Figure C.2: Each octahedral tilt can be classified as a combination of rotations around its three tetrad axes.

or out-of-phase tilt). For a general 3-tilt system, an expanded unit cell of $2 \times 2 \times 2$ is sufficient to fully describe the unit cell (although a smaller unit cell may exist, finding the primitive cell is not necessary). The MATLAB code takes three unit cell parameters and input tilts ($c, b, a, \gamma, \beta, \alpha$ respectively), and generates atomic positions in a number of formats (for visualization in VESTA and as input files for Kirkland multislice simulations). Input unit cell parameters should reflect the expanded output unit cell (*i.e.* double the unit cell of the untilted primitive cell). This output format is similar to the program POTATO used by Woodward [2], except POTATO uses tilt angles and B-O bond distances as input, while unit cell parameters are more appropriate for our purposes, due to epitaxial constraints in our films.

The following describes the procedure for generating a tilted structure, given input tilt parameters α, β, γ:

- Starting coordinates for initial untilted octahedra are

$$\begin{pmatrix} 0 & 1 & 0 \\ 1 & 0 & 0 \\ 0 & 0 & 1 \\ 0 & -1 & 0 \\ -1 & 0 & 0 \\ 0 & 0 & -1 \end{pmatrix} \tag{C.1}$$

  representing the six oxygens in Fig. C.2. Positions are given as fractional coordinates, with origin at the B-cation center. Unit length represents half of the pseudocubic unit cell length.

- Initial octahedron is replicated eight times, one for each octahedron in the expanded unit cell. Each octahedron is the same at this point, except with a different B-cation coordinate shift (*e.g.* $(\frac{1}{4}, \frac{1}{4}, \frac{1}{4})$, $(\frac{1}{4}, \frac{3}{4}, \frac{3}{4})$, etc).

- The first tilt, rotation γ about c, is applied to all octahedra by matrix addition. Depending on the octahedra cell position (shift coordinate), either a clockwise (CW) or counter-clockwise (CCW) tilt is applied.

$$CW_c = \begin{pmatrix} u_1 & 0 & 0 \\ 0 & -v_1 & 0 \\ 0 & 0 & 0 \\ -u_1 & 0 & 0 \\ 0 & v_1 & 0 \\ 0 & 0 & 0 \end{pmatrix} \quad CCW_c = \begin{pmatrix} -u_1 & 0 & 0 \\ 0 & v_1 & 0 \\ 0 & 0 & 0 \\ u_1 & 0 & 0 \\ 0 & -v_1 & 0 \\ 0 & 0 & 0 \end{pmatrix} \tag{C.2}$$

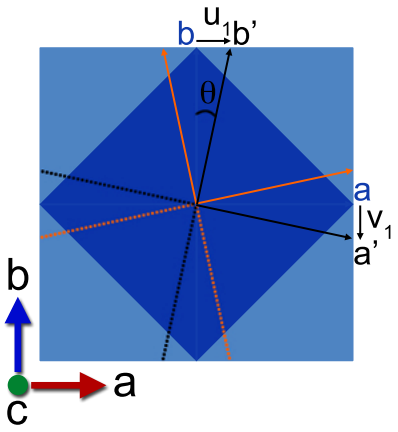

Figure C.3: Octahedral rotation around c-axis. Black and orange lines denote CW and CCW rotation, respectively. u_1 and v_1 are related to the tilt degree and unit cell parameters.

Figure C.3 illustrates the rotation made by the octahedra around the c-axis, with the black and orange lines showing a CW and CCW rotation, respectively. The values u_1 and v_1 are determined by θ (γ) according to:

$$\theta = \tan^{-1}\frac{u_1}{|b|} = \tan^{-1}\frac{v_1}{|a|} \tag{C.3}$$

Note: all three tilts are independent, and therefore CW or CCW tilts on any single octahedron is arbitrary. However once one octahedron has been tilted, all remaining octahedron must tilt according to the tilt system ($a^+b^-b^-$ in this case). Table C.1 shows each octahedron in the expanded unit cell and its corresponding coordinate shift and tilt direction (we have chosen CW CW CW for octahedra 1 in this case).

- After the first tilt, a coordinate transformation, X, is applied to each octahedron by matrix multiplication to keep the axes colinear to each B-O bond. Either a CW

Table C.1: Tilts of octahedra

Octahedra	Shift	γ	α	β
1	$\frac{1}{4}, \frac{1}{4}, \frac{3}{4}$	CW	CW	CW
2	$\frac{3}{4}, \frac{1}{4}, \frac{3}{4}$	CCW	CCW	CCW
3	$\frac{3}{4}, \frac{3}{4}, \frac{3}{4}$	CW	CW	CW
4	$\frac{1}{4}, \frac{3}{4}, \frac{3}{4}$	CCW	CCW	CCW
5	$\frac{1}{4}, \frac{1}{4}, \frac{1}{4}$	CW	CCW	CCW
6	$\frac{3}{4}, \frac{1}{4}, \frac{1}{4}$	CCW	CW	CW
7	$\frac{3}{4}, \frac{3}{4}, \frac{1}{4}$	CW	CCW	CCW
8	$\frac{1}{4}, \frac{3}{4}, \frac{1}{4}$	CCW	CW	CW

or CCW operation is performed to match the tilt direction of the previous step. The X matrices are:

$$X^{CW} = \begin{pmatrix} 1 & -v_1 & 0 \\ u_1 & 1 & 0 \\ 0 & 0 & 1 \end{pmatrix} X^{CCW} = \begin{pmatrix} 1 & v_1 & 0 \\ -u_1 & 1 & 0 \\ 0 & 0 & 1 \end{pmatrix} \tag{C.4}$$

Following the coordinate transformation, the octahedral positions should all resemble their original inputs (only 0, 1, and -1). Note: all matrix multiplications refer to post multiplication.

- A second tilt is applied via matrix addition for rotation around the a-axis:

$$CW_a = \begin{pmatrix} 0 & 0 & -w_2 \\ 0 & 0 & 0 \\ 0 & v_2 & 0 \\ 0 & 0 & w_2 \\ 0 & 0 & 0 \\ 0 & -v_2 & 0 \end{pmatrix} \quad CCW_a = -CW_a \tag{C.5}$$

v_2 and w_2 are related to θ (β) by:

$$\theta = \tan^{-1} \frac{v_2}{|c|} = \tan^{-1} \frac{w_2}{|b|} \tag{C.6}$$

Note: it might be more appropriate to use $|b'|$ instead of $|b|$ in the equation above, since $|b'|$ is slightly longer (see Fig. C.3, $|b'| = \sqrt{|b'|^2 + v_1^2}$). This occurs since we are keeping the unit cell parameters constant, and therefore the B-O bond distances will vary as the octahedra rotates. Subsequent tilts will similarly lengthen the coordinate axes along the two perpendicular directions. For equal tilts around all three axes, and cubic unit cell parameters, it becomes apparent that the octahedral bond lengths will distort asymmetrically depending on the order of the axes we choose to rotate around. The cause of this effect was pointed out by Glazer [22], who noted that the separate tilt operations do not belong to an Abelian group, and therefore the tilt order affects the final atomic arrangement. However for small tilt angles ($< 15°$), this sequence dependence is only a second-order effect [22]. Indeed, tests incorporating elongated axes with structures up to $\sim 7°$ tilts show negligible

(sub-picometer) differences in final atomic positions. Therefore for ease, we use initial lattice parameters, $|a|, |b|, |c|$, for u, v, w calculations.

- A second coordinate transformation, Y, is applied via matrix multiplication. CW and CCW matrices for Y are:

$$Y^{CW} = \begin{pmatrix} 1 & 0 & 0 \\ 0 & 1 & -w_2 \\ 0 & v_2 & 1 \end{pmatrix} Y^{CCW} = \begin{pmatrix} 1 & 0 & 0 \\ 0 & 1 & w_2 \\ 0 & -v_2 & 1 \end{pmatrix} \tag{C.7}$$

  Following the coordinate transformation, the octahedral positions should all resemble their original inputs (only 0, 1, and -1).

- The third tilt, rotation around the b-axis, is applied via matrix addition, according to:

$$CW_b = \begin{pmatrix} 0 & 0 & 0 \\ 0 & 0 & w_3 \\ -u_3 & 0 & 0 \\ 0 & 0 & 0 \\ 0 & 0 & -w_3 \\ u_3 & 0 & 0 \end{pmatrix} CCW_b = -CW_b \tag{C.8}$$

  with

$$\theta = \tan^{-1} \frac{u_3}{|c|} = \tan^{-1} \frac{w_3}{|a|} \tag{C.9}$$

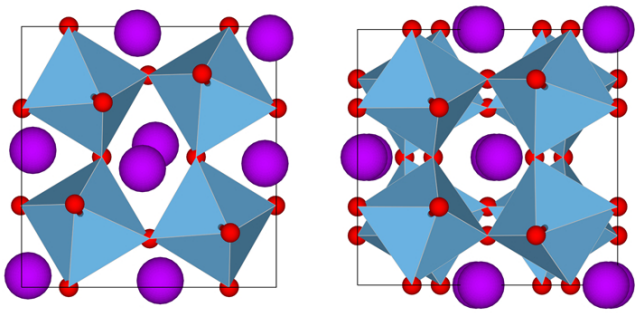

Figure C.4: Structure corresponding to $7.5^{+}6.5^{-}6.5^{-}$ with $a = c = 7.72, b = 7.88$ along in-phase (left) and out-of-phase (right) directions.

- Atomic positions are transformed back to the original coordinate system by multiplying with $\mathrm{Y}^{-1}\mathrm{X}^{-1}$.

- Atomic positions are divided by four (each B-O bond distance is $\frac{1}{4}$ the length of the expanded unit cell) and each octahedron is shifted (see Table C.1) to create the final structure. Figure C.4 shows an example structure created with α=6.5 and γ=7.5 along the in-phase (c) and out-of-phase (a, b) axes.

C.2.2 Approximations, Constraints and Errors

In the previous section, we assume octahedra maintain 90° inner angles during rotation. Since unit cell parameters are constrained due to substrate coherency (confirmed by out-of-plane x-ray measurements), internal B-O bond angles vary according to tilt type and degree. So far, all the atomic coordinates have been transformed to fit inside an expanded cell composed of the original cubic cell. The Fast Fourier Transform algorithm used in the Kirkland program suite [38] requires orthogonal axes, which fixes the angles between the cell axes, while the rest of the cell parameters are set by the film growth. A result of this constraint for Pbnm structures along $[110]_{\mathrm{O}}$ is detailed at the end of Appendix B, and also causes octahedra along the a-axis to not properly

line up, as illustrated in Fig. C.5. This error arises since in the $a^+b^-b^-$ tilt system, the two out-of-phase axes (a and b in this case) in the pseudocubic unit cell are inclined to one another, according to the rules formulated by Glazer [22]. Indeed, if the cartesian coordinates in Fig. C.5 are transformed so that the a-axis rotates by angle θ, such that $\theta = \tan^{-1}\frac{\Delta}{0.5}$ (red line in Fig. C.5), no mismatches in the octahedra coordinates occur. This is represented mathematically as pre-multiplying the final coordinates by:

$$\begin{pmatrix} 1 & \tan\theta & 0 \\ 0 & 1 & 0 \\ 0 & 0 & 1 \end{pmatrix} \tag{C.10}$$

To incorporate this angle into multislice simulations, one would need to create a supercell of the desired dimensions and then transform back to cartesian coordinates. While the supercell would be translatable along c, the in-phase axis, imaging the crystal along an out-of-phase axis would require a separate supercell for each sample thickness, impractical for a large range of thicknesses [see Fig. B.2(c)]. Therefore, an approximate structure is used, with orthogonal pseudocubic cells. The mismatch at the octahedra corners along a are resolved by using the average position. The estimated positional errors associated with this approximation is small, on the order of a couple picometers for the example in Fig. C.4 ($\sim$ $GdTiO_3$ bulk-level distortions, the largest needed for practical purposes). The angle between a and b for this structure is 2.85°.

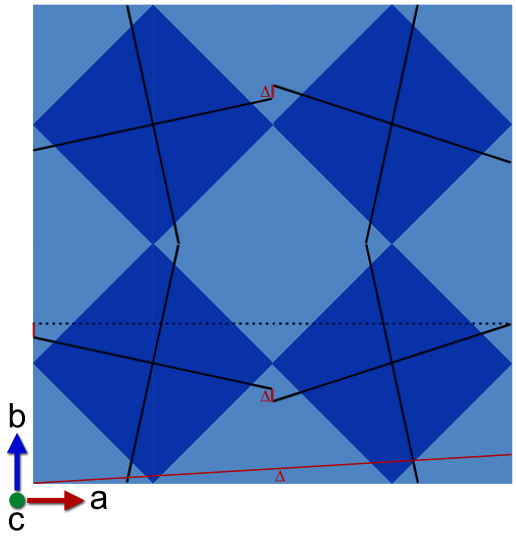

Figure C.5: Tilted octahedra (black lines) along the a-axis are offset (red lines) by distance Δ.

Appendix D

Quantitative STEM Procedure

In the following section, I outline the procedure used for the quantitative STEM analysis as described in Chapter 5. This procedure was first developed by Prof. James LeBeau [69], and have been subsequently edited for improved speed and ease of use. I first summarize the differences in the original procedure to those used here, and then provide a more detailed outline of the current quantitative STEM procedure.

D.1 Differences From Original Procedure

There are two main differences between the procedure used in [69] and the one used in this dissertation. The first difference is that the FEI imaging software is used for the image acquisition in the present study, as opposed to the National Instruments LabVIEW SignalExpress software. LabVIEW SignalExpress was originally used to record the data from an external dynamic signal analyzer (DSA), connected to the secondary parallel output of the ADF detector. The DSA benefits from 24-bit resolution, as opposed to 16-bit resolution of the native FEI software, allowing for much greater dynamic range (16.8 million shades of gray compared to 65,536). However, the image acquisition process is longer and more complicated, and requires more post-processing.

For the present studies, where serial image acquisitions were needed, along with small

microscope adjustments in between each acquisition, the speed and ease of the FEI software made it much more appealing. Test experiments by Jinwoo Hwang showed that the difference between using the reduced bit-depth data (FEI software) was many times lower ($10 - 1000\times$ lower) than the experimental error function, making the reduction in dynamic range negligible in the final quantitative analysis. Other groups [200] have also successfully used the 16-bit data from the native FEI software for their quantitative analysis, while achieving a good match with image simulations.

The other main difference in the present study involves the methodology in calculating the simulated HAADF images. For past studies [69], where the local maximum or centroid intensity is used, and structures are homogenous, the speed of image simulations could be greatly increased by only calculating a 1-dimensional line intensity profile, with relatively few pixels in between. For example, to compare the experimental intensities of Sr and Ti columns in $SrTiO_3$ with simulated values, only a simple line profile, as shown in Figure D.1(a), is needed to extract the necessary column intensities. This intensity can be plotted as a function of thickness, as shown in Figure D.1(b), so that only 1 image simulation is needed for an entire thickness range. This type of calculation has the additional benefit of reusing the exit wave function at each thickness slice as the starting wave function for the next thickness slice, greatly reducing computation times.

For the current dopant studies however, several new requirements are needed. Since we are now averaging over an area around each column rather than extracting a single intensity value, a 2-dimensional image needs to be simulated in order to obtain a radial average, greatly increasing the number of pixels needed in the simulation. Furthermore, because a dopant atom destroys the translational symmetry of the structure, a supercell input structure is required. Using a supercell has a large effect on the image simulation, since now the exit wave functions at the end of each thickness slice can no longer be reused. This means a unique structural model needs to be generated for each thickness

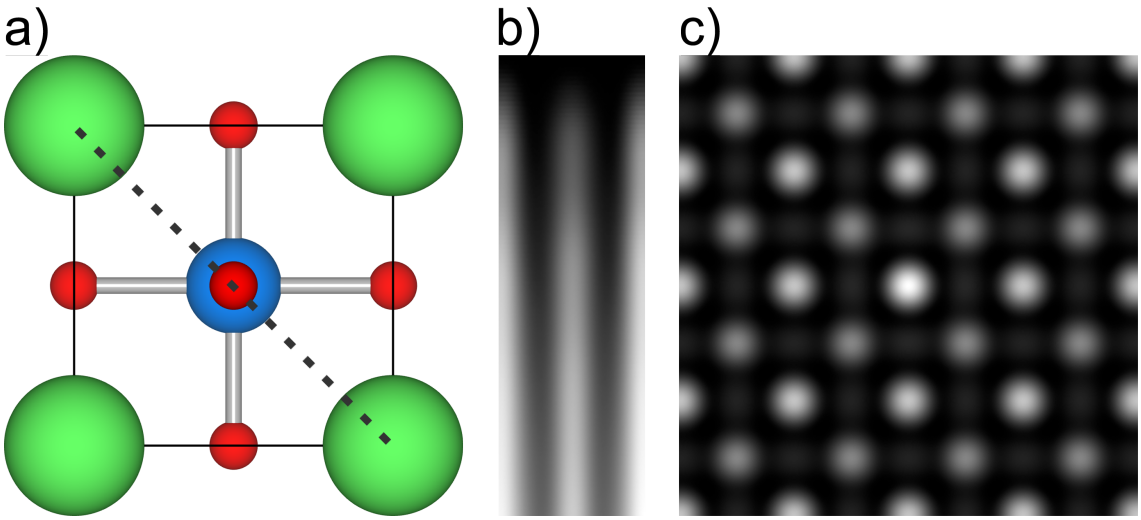

Figure D.1: (a) Unit cell of $SrTiO_3$ along [100]. (b) 1-dimensional line simulation of $SrTiO_3$ along the dotted line in (a), showing intensity (horizontal dimension) as a function of sample thickness (vertical dimension). (c) 2-dimensional image simulation of doped $SrTiO_3$ using an expanded 4×4 unit cell, with the dopant atom in the center. Sample thickness is 5 unit cells.

film and dopant position, such as the one shown in Fig. D.1(c). The result of these changes in the simulation requirements means that a simulation that once took a matter of hours for a whole thickness series will now take up to several weeks to complete. Even running multiple jobs on a network cluster is not efficient enough for the full scale calculations needed for the 3D dopant study of Chapter 5.

To save computation time, multislice calculations for all the structural dopant configurations were performed at 0 K, rather than using computationally expensive frozen phonon simulations at room temperature. The effect of thermal diffuse scattering (TDS) was accounted for afterwards, by multiplying the column intensities with a scaling factor, S:

$$S = \frac{I_{TDS}}{I_{noTDS}} \tag{D.1}$$

where I_{TDS} and I_{noTDS} are the averaged column intensities including TDS and not including TDS, respectively. The scaling factor S was calculated for an undoped $SrTiO_3$ sample at the same thickness (5 unit cells), using multislice simulations with and without TDS. While this calculation ignores the differences in the Debye-Waller factors between Sr and Gd, the effect would be very small, as the averaged column intensities are not sensitive to thermal vibrations [186].

D.2 Quantitative STEM Procedure

Below I outline the experimental method for quantitative STEM used for the dopant study in this thesis.

D.2.1 Experimental Parameters

The experimental parameters of the microscope are described in Chapter 5 and reiterated here. All images were acquired on a field-emission FEI Titan S/TEM microscope (C_s=1.2 mm), operated at 300 kV with a 9.6 mrad convergence angle. The gun lens was set to standard STEM imaging conditions (gun lens = 6, extraction voltage = 4400 V), and a spot size of 10 was used. Images were recorded using 512×512 pixels with a 50 μs dwell time. Camera lengths of 100 and 130 mm (corresponding to inner angles of $\sim$ 60 and 47 mrad) were used for each set of images.

D.2.2 ADF Detector Settings

Brightness and contrast settings on the FEI control software are first set to maximize the dynamic range of the detector without signal clipping. This is achieved by first using the deflection coils in STEM diffraction mode ("diffraction shift" in the software) to move

the zero-beam disc within the hole of the ADF detector. The approximate location of the hole in the ADF detector should be known. If not, the detector centering step can be done first. Also, using smaller camera lengths can be useful in this step (I generally use 100 mm). Then, while scanning over an empty region, the brightness is adjusted so that the *mean* intensity reads approximately 10. This value can be increased if it appears certain pixels are below the dark noise current (the minimum intensity values are not changing as brightness is increased). Next, the deflection coils are used to bring the zero-beam directly onto the detector, and the contrast controls are adjusted so that the *maximum* intensity values just saturate (reach approximately 65536).

D.2.3 ADF Detector Centering

The ADF detector must be well-centered along the optic axis for the scattered electrons to be detected uniformly over the detector. As detailed in [69], while the shadow of the detector can be observed on the viewing screen and CCD camera, this shadow does not accurately represent the edge of the detector. To locate the inner edge of the detector, in STEM diffraction mode, the zero-beam disc is used to trace the edge by using the deflection coils and observing an increase in detector signal.

Similar to the previous procedure, the zero-beam disc is first moved inside the hole of the detector (signal level should be around 10, or whichever value it was set to from the previous step). A circle the size of the zero-beam disc can be drawn on the viewing screen with the Gatan software. Using the deflection coils ("diffraction shift"), the beam is then moved around the detector until a small signal is observed (I usually use ~ 100). At each location with the same output signal, the beam location can be marked with a circle, until an image of the detector edge is built up, as shown in Figure D.2. A larger circle is drawn to show the approximate edge of the detector, and the center of the detector can

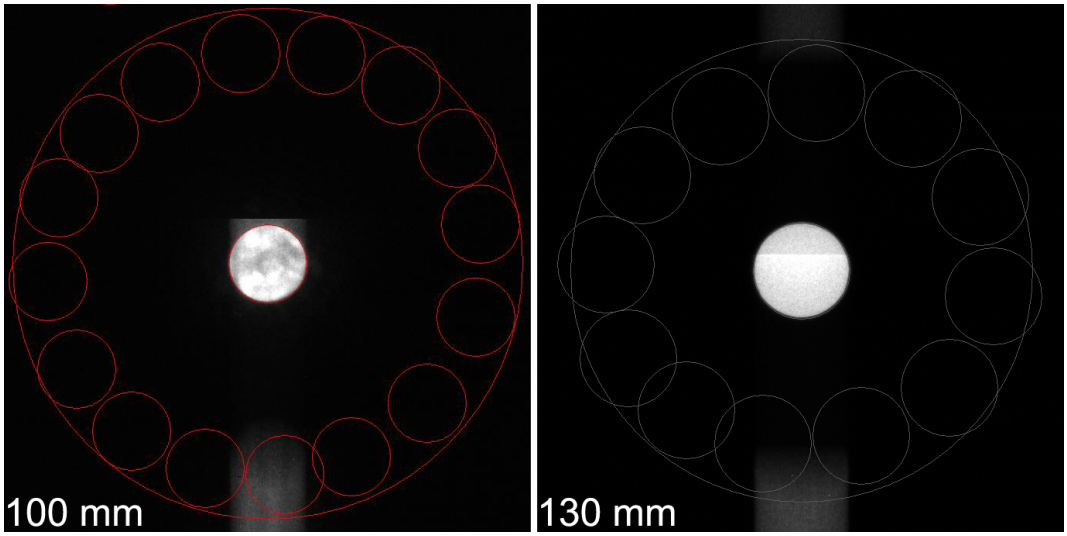

Figure D.2: Tracing the inner edge of the ADF detector using the zero-beam disc on the CCD camera, for 100 mm and 130 mm camera lengths. The approximate edge of the detector is shown by the large circle, while the center of the detector is marked with a smaller circle the size of the convergent beam.

be determined and similarly marked. Since the convergence angle of the probe is known (9.6 mrad in this case), the inner detector angle can be determined.

For VA-HAADF, this procedure is done twice, once for each camera length. The center of the detectors are slightly different for each camera length, due to differences in the projector lens settings, so the diffraction beam needs to be re-centered in between image acquisitions, anytime the camera length is changed. This can be easily done by keeping a copy of the detector center (Fig. D.2) on the CCD viewing screen for each camera length, and visually re-centering the diffraction pattern, or by observing the "user diffraction shift" values for each camera length (on the "system info" panel) when the diffracted beam is centered, and realigning the diffraction shift to those centered values whenever they are changed.

D.2.4 Image Intensity Normalization

After calibrating the detector settings and position, an image of the detector is needed to record its response. This can be achieved by switching out of diffraction mode, so that an image of the probe is now on the screen, and scanning this electron probe across the detector (scanning a region without a sample). A blanked image should also be taken at this time, as a noise floor calibration. For VA-HAADF, this procedure is done for both camera lengths.

After the detector image is taken, HAADF imaging can be carried out as usual, by switching back to diffraction mode and re-centering the zero-beam diffraction disc if any movement has occurred. For VA-HAADF, successive images are taken at different camera lengths, while adjusting the diffracted disc to the detector center every time the camera length is changed. Due to sample drift, swift setup of the imaging conditions between each successive acquisition will aid in correlating the two images together. Estimates of the sample drift between each image can be approximated by the distortion in each image caused by drift, or through a quick-acquisition image series.

Image intensities can then be normalized to the incident probe intensity during post-acquisition processing, according to:

$$\overline{I_{xy}} = \frac{I_{xy} - I_o}{I_p - I_o} \tag{D.2}$$

where $\overline{I_{xy}}$ is the normalized image intensity at position (x, y), I_{xy} is the measured intensity at position (x, y), I_o is the detector offset (blank beam intensity), and I_p is the incident probe intensity. To account for the detector non-uniformity [185], the incident probe intensity, I_p, is obtained by averaging the signal between 60-120 mrad (2× the inner angle) and 47-141 mrad (3× the inner angle) for detector 1 and detector 2, respectively. A detailed discussion of why this is necessary is described in [185], but this method

essentially uses an "effective" outer angle to counterbalance the lower detector sensitivity near the inner edge of the detector, where most of the scattered electrons are detected.

The post-acquisition processing is done using custom MATLAB scripts. Image intensities of the blanked beam images are averaged to obtain I_o, while elliptical regions of interest, corresponding to the desired inner and outer angles, are selected for each detector image and averaged to obtain I_p. Image intensities are then normalized to the incident beam by linear transformation, according to Eqn. D.2.

Appendix E

VA-HAADF: Additional Calculations and Tables

E.1 Dopant Number Calculation

Supplementary Table E.1 lists the dopant number calculations for the atom in region 1 using detector 1 from Fig. 5.11 of Chapter 5. The distance t is calculated between the listed experimental point and each simulated configuration, normalized by the standard deviation of the error function. The values for $norm_i(t)$ can be found using any statistical software. $\sum norm(t)$ is calculated separately for the 0, 1, and 2 dopant cases. Most probabilistic values of $norm(t)$ for 0, 1, or 2 dopants are listed in the next column. Values for p_i are calculated according to Eq. 5.2, using the corresponding $\sum norm(t)$, while the probabilities of having 0, 1, or 2 dopants in the column are calculated with Eq. 5.2 using values only from the most probabilistic column.

E.2 Dopant Position Calculation

The calculation for the position of the dopant marked by squares in Fig. 5.11 is given in Table E.2. The expected value is given as the sum of $z_i p_i$ while the uncertainty is the square root of the sum of the third column. The calculation for detector 2 is done

Table E.1: Values for calculating the individual configurational p_i and the probabilities of having 0, 1, or 2 dopants in the square column from Fig. 5.11. Table reproduced from Ref. [45].

	I_{Sr}	I_{Ti}	t	norm (t)	Σnorm(t)	most prob.	p_i	prob. config.
Experimental Position	0.00704	0.00295						
Simulated Positions								
5	0.00859	0.00315	2.151	0.0395			0.0279	
4	0.00737	0.00310	0.496	0.353			0.249	
3	0.00715	0.00309	0.245	0.387			0.273	
2	0.00679	0.00308	0.394	0.369			0.261	
1	0.00641	0.00306	0.894	0.267	1.416	0.387	0.189	0.649
4,5	0.0108	0.00324	5.228	4.64E-7			1.43E-6	
3,5	0.0108	0.00325	5.279	3.55E-7			1.10E-6	
2,5	0.0102	0.00322	4.320	3.53E-5			1.09E-4	
1,5	0.00986	0.00320	3.923	1.81E-4			5.60E-4	
3,4	0.00931	0.00318	3.154	0.00276			0.00852	
2,4	0.00907	0.00317	2.830	0.00727			0.0225	
1,4	0.00856	0.00315	2.120	0.0422			0.130	
2,3	0.00866	0.00316	2.254	0.0314			0.0972	
1,3	0.00842	0.00315	1.934	0.0614			0.190	
1,2	0.00794	0.00313	1.269	0.178	0.324	0.178	0.551	0.301
0	0.00540	0.00302	2.266	0.0306	0.0306	0.0306	1	0.0507

Table E.2: Calculation for the position of the dopant, from the atom column marked by squares in Fig. 5.11. Table reproduced from Ref. [45].

Atom Positions	$z_i * p_i$	$(z_i - \mu)^2 * p_i$
5	0.138	0.150
4	0.994	0.444
3	0.819	0.0310
2	0.522	0.115
1	0.190	0.525
Sum	2.66	1.27

the same way, while for the combined detector, respective values of $norm_i^c(t)$ for both detectors are multiplied together and all subsequent calculations remain the same.

Table E.3: Calculation results from 100,000 randomly scattered simulated points around each dopant configuration, grouped by number of dopants in the atomic column. Results are given for each individual detector as well as the combined setting. For each configuration: row 1 is the average calculated position and uncertainty for all data points around that configuration; row 2 is the percent of points with calculated positions that round to the actual dopant position; row 3 is the percentage of points with calculated positions that lie within the uncertainty range of the actual dopant position. Table reproduced from Ref. [45].

Pos.		Detector 1	Detector 2	Combined
5	Exp. Val.	4.30±0.78	4.50±0.56	4.74±0.35
	% Correct	50.9%	65.8%	81.8%
	In Range	75.5%	80.1%	84.9%
4	Exp. Val.	3.08±1.08	3.89±0.81	3.79±0.69
	% Correct	22.2%	48.0%	58.2%
	In Range	54.2%	65.8%	72.7%
3	Exp. Val.	2.86±1.09	2.36±0.93	2.46±0.84
	% Correct	48.3%	19.3%	30.2%
	In Range	84.3%	50.0%	58.6%
2	Exp. Val.	2.53±1.07	2.10±0.86	2.08±0.79
	% Correct	51.0%	88.5%	80.3%
	In Range	84.3%	96.2%	92.7%
1	Exp. Val.	2.23±1.02	2.14±0.87	1.94±0.79
	% Correct	6.0%	0%	12.5%
	In Range	40.9%	0%	42.5%

Pos.		Detector 1		Detector 2		Combined	
		Atom 1	Atom 2	Atom 1	Atom 2	Atom 1	Atom 2
4,5	Exp. Val.	2.76±0.93	4.83±0.32	3.37±0.75	4.95±0.15	3.48±0.64	4.99±0.06
	% Correct	0%	90.3%	54.7%	98.7%	62.2%	99.9%
	In Range	21.7%	95.5%	76.8%	99.7%	79.6%	99.9%
3,5	Exp. Val.	2.78±0.92	4.84±0.31	2.23±0.91	4.63±0.43	2.56±0.80	4.90±0.22
	% Correct	73.3%	91.3%	14.0%	74.5%	44.2%	95.8%
	In Range	93.2%	96.0%	43.3%	75.8%	73.1%	96.1%
2,5	Exp. Val.	2.37±0.93	4.56±0.52	2.17±0.89	4.59±0.45	2.23±0.84	4.73±0.34
	% Correct	62.3%	65.3%	87.6%	68.2%	81.3%	80.7%
	In Range	88.6%	78.7%	95.9%	69.6%	92.1%	81.4%
1,5	Exp. Val.	2.21±0.91	4.40±0.60	2.17±0.89	4.58±0.45	2.13±0.88	4.65±0.38
	% Correct	1.9%	49.8%	0.2%	68.1%	0.4%	70.9%
	In Range	11.5%	65.5%	1.6%	69.5%	11.8%	71.5%
3,4	Exp. Val.	1.92±0.82	4.01±0.71	1.97±0.82	4.30±0.53	1.91±0.78	4.25±0.45
	% Correct	6.8%	59.2%	2.0%	58.7%	1.0%	67.4%
	In Range	26.2%	77.3%	11.7%	62.2%	5.5%	69.1%
2,4	Exp. Val.	1.81±0.78	3.84±0.74	1.89±0.79	4.13±0.56	1.83±0.75	4.05±0.46
	% Correct	80.0%	57.2%	93.5%	65.5%	90.1%	74.3%
	In Range	90.8%	79.0%	96.5%	70.3%	95.0%	77.2%
1,4	Exp. Val.	1.60±0.68	3.48±0.78	1.94±0.81	4.24±0.54	1.69±0.73	3.98±0.43
	% Correct	39.7%	40.2%	3.3%	61.6%	23.3%	82.1%
	In Range	73.0%	67.0%	12.4%	65.5%	61.2%	85.0%
2,3	Exp. Val.	1.64±0.70	3.55±0.77	1.43±0.54	2.87±0.56	1.46±0.52	2.92±0.50
	% Correct	64.5%	50.7%	20.5%	77.6%	38.1%	78.5%
	In Range	77.9%	71.3%	28.4%	81.2%	43.1%	81.1%
1,3	Exp. Val.	1.55±0.65	3.39±0.78	1.48±0.57	3.02±0.57	1.44±0.53	2.98±0.52
	% Correct	47.1%	62.5%	68.5%	75.5%	67.3%	74.0%
	In Range	79.0%	81.1%	87.6%	80.7%	79.7%	77.3%
1,2	Exp. Val.	1.39±0.56	3.10±0.78	1.36±0.50	2.68±0.53	1.27±0.42	2.57±0.48
	% Correct	72.4%	5.2%	91.8%	27.4%	92.3%	45.8%
	In Range	93.0%	23.1%	98.1%	28.0%	94.9%	47.6%

Bibliography

[1] R. S. Francis S. Galasso and N. Kurti, *Structure, Properties and Preparation of Perovskite-Type Compounds*. International Series of Monographs in Solid State Physics. Pergamon, 1969.

[2] P. M. Woodward, *Octahedral tilting in perovskites. I. Geometrical considerations*, *Acta Crystallographica* **B53** (1997) 32–43.

[3] M. A. Peña, , and J. L. G. Fierro, *Chemical structures and performance of perovskite oxides*, *Chemical Reviews* **101** (2001), no. 7 1981–2018.

[4] A. von Hippel, *Ferroelectricity, domain structure, and phase transitions of barium titanate*, *Reviews of Modern Physics* **22** (1950), no. 3 221–237.

[5] A. Sleight, J. Gillson, and P. Bierstedt, *High-temperature superconductivity in the $BaPb_{1-x}Bi_xO_3$ systems*, *Solid State Communications* **17** (1975), no. 1 27 – 28.

[6] G. Jonker and J. V. Santen, *Ferromagnetic compounds of manganese with perovskite structure*, *Physica* **16** (1950), no. 3 337 – 349.

[7] Y. Moritomo, A. Asamitsu, H. Kuwahara, and Y. Tokura, *Giant magnetoresistance of manganese oxides with a layered perovskite structure*, *Nature* **380** (03, 1996) 141–144.

[8] C. R. Serrao, A. Sundaresan, and C. N. R. Rao, *Multiferroic nature of charge-ordered rare earth manganites*, *Journal of Physics: Condensed Matter* **19** (2007) 496217.

[9] H. D. Zhou and J. B. Goodenough, *Localized or itinerant TiO_3 electrons in $RTiO_3$ perovskites*, *Journal of Physics: Condensed Matter* **17** (2005), no. 46 7395.

[10] J. Son, J. M. LeBeau, S. J. Allen, and S. Stemmer, *Conductivity enhancement of ultrathin $LaNiO_3$ films in superlattices*, *Applied Physics Letters* **97** (2010) 202109.

[11] B. Jalan and S. Stemmer, *Large seebeck coefficients and thermoelectric power factor of La-doped $SrTiO_3$ thin films*, *Applied Physics Letters* **97** (2010), no. 4 042106.

[12] R. H. Mitchell, *Perovskites modern and ancient*, *Acta Crystallographica Section B* **58** (Dec, 2002) 1075.

[13] A. Vailionis, H. Boschker, W. Siemons, E. P. Houwman, D. H. A. Blank, G. Rijnders, and G. Koster, *Misfit strain accommodation in epitaxial ABO_3 perovskites: Lattice rotations and lattice modulations*, *Phys. Rev. B* **83** (Feb, 2011) 064101.

[14] A. J. Millis, P. B. Littlewood, and B. I. Shraiman, *Double exchange alone does not explain the resistivity of $La_{1-x}Sr_xMnO_3$*, *Phys. Rev. Lett.* **74** (Jun, 1995) 5144–5147.

[15] I. H. Inoue, O. Goto, H. Makino, N. E. Hussey, and M. Ishikawa, *Bandwidth control in a perovskite-type $3d^1$-correlated metal $Ca_{1-x}Sr_xVO_3$. I. Evolution of the electronic properties and effective mass*, *Phys. Rev. B* **58** (Aug, 1998) 4372–4383.

[16] H. Y. Hwang, Y. Iwasa, M. Kawasaki, B. Keimer, N. Nagaosa, and Y. Tokura, *Emergent phenomena at oxide interfaces*, *Nature Materials* **11** (February, 2012) 103–113.

[17] C. L. Jia, S. B. Mi, M. Faley, U. Poppe, J. Schubert, and K. Urban, *Oxygen octahedron reconstruction in the $SrTiO_3/LaAlO_3$ heterointerfaces investigated using aberration-corrected ultrahigh-resolution transmission electron microscopy*, *Phys. Rev. B* **79** (Feb, 2009) 081405.

[18] E. Dagotto, *When oxides meet face to face*, *Science* **318** (2007), no. 5853 1076–1077.

[19] A. Okazaki and Y. Suemune, *The crystal structures of $KMnF_3$, $KFeF_3$, $KCoF_3$, $KNiF_3$ and $KCuF_3$ above and below their Néel temperatures*, *Journal of the Physical Society of Japan* **16** (1961), no. 4 671–675.

[20] G. Shirane, H. Danner, and R. Pepinsky, *Neutron diffraction study of orthorhombic $BaTiO_3$*, *Phys. Rev.* **105** (Feb, 1957) 856–860.

[21] P. M. Woodward, *Octahedral tilting in perovskites. II. Structure stabilizing forces*, *Acta Crystallographica* **B53** (1997) 44–66.

[22] A. M. Glazer, *The classification of tilted octahedra in perovskites*, *Acta Crystallographica Section B* **28** (Nov, 1972) 3384–3392.

[23] E. Dagotto, *Complexity in strongly correlated electronic systems*, *Science* **309** (2005), no. 5732 257–262.

[24] J. M. Rondinelli, S. J. May, and J. W. Freeland, *Control of octahedral connectivity in perovskite oxide heterostructures: An emerging route to multifunctional materials discovery*, *MRS Bulletin* **37** (2012) 261–270.

[25] J. M. Rondinelli and N. A. Spaldin, *Substrate coherency driven octahedral rotations in perovskite oxide films*, *Phys. Rev. B* **82** (2010) 113402.

[26] A. Bhattacharya and S. J. May, *Magnetic oxide heterostructures*, *Annual Review of Materials Research* **44** (2014), no. 1 65–90.

[27] S. Stemmer and A. J. Millis, *Quantum confinement in oxide quantum wells*, *MRS Bulletin* **38** (12, 2013) 1032–1039.

[28] H. Y. Ohtomo, A.Hwang, *A high-mobility electron gas at the $LaAlO_3/SrTiO_3$ heterointerface.*, *Nature* **427** (2004), no. 6973 423.

[29] M. Huijben, G. Rijnders, D. H. A. Blank, S. Bals, S. V. Aert, J. Verbeeck, G. V. Tendeloo, A. Brinkman, and H. Hilgenkamp, *Electronically coupled complementary interfaces between perovskite band insulators*, *Nat Mater* **5** (07, 2006) 556–560.

[30] Editorial, *The interface is still the device*, *Nat Mater* **11** (02, 2012) 91–91.

[31] F. He, B. O. Wells, Z.-G. Ban, S. P. Alpay, S. Grenier, S. M. Shapiro, W. Si, A. Clark, and X. X. Xi, *Structural phase transition in epitaxial perovskite films*, *Phys. Rev. B* **70** (Dec, 2004) 235405.

[32] S. J. May, J.-W. Kim, J. M. Rondinelli, E. Karapetrova, N. A. Spaldin, A. Bhattacharya, and P. J. Ryan, *Quantifying octahedral rotations in strained perovskite oxide films*, *Phys. Rev. B* **82** (Jul, 2010) 014110.

[33] S. J. May, C. R. Smith, J.-W. Kim, E. Karapetrova, A. Bhattacharya, and P. J. Ryan, *Control of octahedral rotations in $(LaNiO_3)_n/(SrMnO_3)_m$ superlattices*, *Phys. Rev. B* **83** (Apr, 2011) 153411.

[34] D. I. Woodward and I. M. Reaney, *Electron diffraction of tilted perovskites*, *Acta Crystallographica Section B* **61** (Aug, 2005) 387–399.

[35] J. M. LeBeau, S. D. Findlay, L. J. Allen, and S. Stemmer, *Quantitative atomic resolution scanning transmission electron microscopy*, *Phys. Rev. Lett.* **100** (May, 2008) 206101.

[36] J. C. H. Spence, *High-Resolution Electron Microscopy*. Oxford University Press, third ed., 2003.

[37] D. B. Williams and C. B. Carter, *Transmission Electron Microscopy*. Springer, second ed., 2009.

[38] E. J. Kirkland, *Advanced Computing in Electron Microscopy*. Springer, 2 ed., 2010.

[39] S. Findlay, S. Azuma, N. Shibata, E. Okunishi, and Y. Ikuhara, *Direct oxygen imaging within a ceramic interface, with some observations upon the dark contrast at the grain boundary*, *Ultramicroscopy* **111** (2011), no. 4 285 – 289.

[40] J. M. LeBeau, S. D. Findlay, L. J. Allen, and S. Stemmer, *Position averaged convergent beam electron diffraction: Theory and applications*, *Ultramicroscopy* **110** (2010), no. 2 118 – 125.

[41] J. Y. Zhang, J. Hwang, S. Raghavan, and S. Stemmer, *Symmetry lowering in extreme-electron-density perovskite quantum wells*, *Phys. Rev. Lett.* **110** (Jun, 2013) 256401.

[42] J. Y. Zhang, C. A. Jackson, R. Chen, S. Raghavan, P. Moetakef, L. Balents, and S. Stemmer, *Correlation between metal-insulator transitions and structural distortions in high-electron-density $SrTiO_3$ quantum wells*, *Phys. Rev. B* **89** (Feb, 2014) 075140.

[43] J. Y. Zhang, C. A. Jackson, S. Raghavan, J. Hwang, and S. Stemmer, *Magnetism and local structure in low-dimensional mott insulating $GdTiO_3$*, *Phys. Rev. B* **88** (Sep, 2013) 121104.

[44] J. Y. Zhang, H. Kim, E. Mikheev, A. J. Hauser, and S. Stemmer, *Key role of lattice symmetry in the metal-insulator transition of $NdNiO_3$ films*, *Scientific Reports* **6** (04, 2016) 23652.

[45] J. Y. Zhang, J. Hwang, B. J. Isaac, and S. Stemmer, *Variable-angle high-angle annular dark-field imaging: application to three-dimensional dopant atom profiling*, *Scientific Reports* **5** (07, 2015) 12419 EP –.

[46] J. Hwang, J. Y. Zhang, A. J. D'Alfonso, L. J. Allen, and S. Stemmer, *Three-dimensional imaging of individual dopant atoms in $SrTiO_3$*, *Phys. Rev. Lett.* **111** (Dec, 2013) 266101.

[47] N. F. Mott, *The basis of the electron theory of metals, with special reference to the transition metals*, *Proceedings of the Physical Society. Section A* **62** (1949), no. 7 416.

[48] N. F. Mott, *Metal-insulator transition*, *Reviews of Modern Physics* **40** (1968), no. 4 677–683.

[49] M. Imada, A. Fujimori, and Y. Tokura, *Metal-insulator transitions*, *Rev. Mod. Phys.* **70** (Oct, 1998) 1039–1263.

[50] M. Mochizuki and M. Imada, *Orbital physics in the perovskite Ti oxides*, *New Journal of Physics* **6** (2004), no. 1 154.

[51] J. M. Rondinelli and N. A. Spaldin, *Structure and properties of functional oxide thin films: Insights from electronic-structure calculations*, *Advanced Materials* **23** (2011), no. 30 3363–3381.

[52] G. Rupprecht, R. O. Bell, and B. D. Silverman, *Nonlinearity and microwave losses in cubic strontium-titanate*, *Phys. Rev.* **123** (Jul, 1961) 97–98.

[53] J. Appel, *Soft-mode superconductivity in $SrTiO_3$*, *Phys. Rev.* **180** (Apr, 1969) 508–516.

[54] P. Moetakef, T. A. Cain, D. G. Ouellette, J. Y. Zhang, D. O. Klenov, A. Janotti, C. G. V. de Walle, S. Rajan, S. J. Allen, and S. Stemmer, *Electrostatic carrier doping of $GdTiO_3/SrTiO_3$ interfaces*, *Applied Physics Letters* **99** (2011), no. 23 232116.

[55] C. A. Jackson and S. Stemmer, *Interface-induced magnetism in perovskite quantum wells*, *Phys. Rev. B* **88** (Nov, 2013) 180403.

[56] P. Moetakef, C. A. Jackson, J. Hwang, L. Balents, S. J. Allen, and S. Stemmer, *Toward an artificial mott insulator: Correlations in confined high-density electron liquids in $SrTiO_3$*, *Physical Review B* **86** (2012), no. 20.

[57] R. Scherwitzl, S. Gariglio, M. Gabay, P. Zubko, M. Gibert, and J.-M. Triscone, *Metal-insulator transition in ultrathin $LaNiO_3$ films*, *Phys. Rev. Lett.* **106** (Jun, 2011) 246403.

[58] A. V. Boris, Y. Matiks, E. Benckiser, A. Frano, P. Popovich, V. Hinkov, P. Wochner, M. Castro-Colin, E. Detemple, V. K. Malik, C. Bernhard, T. Prokscha, A. Suter, Z. Salman, E. Morenzoni, G. Cristiani, H.-U. Habermeier, and B. Keimer, *Dimensionality control of electronic phase transitions in nickel-oxide superlattices*, *Science* **332** (2011), no. 6032 937–940.

[59] J. Liu, M. Kareev, D. Meyers, B. Gray, P. Ryan, J. W. Freeland, and J. Chakhalian, *Metal-insulator transition and orbital reconstruction in mott-type quantum wells made of $NdNiO_3$*, *Phys. Rev. Lett.* **109** (Sep, 2012) 107402.

[60] K. Yoshimatsu, T. Okabe, H. Kumigashira, S. Okamoto, S. Aizaki, A. Fujimori, and M. Oshima, *Dimensional-crossover-driven metal-insulator transition in $SrVO_3$ ultrathin films*, *Phys. Rev. Lett.* **104** (Apr, 2010) 147601.

[61] R. Chen, S. Lee, and L. Balents, *Dimer mott insulator in an oxide heterostructure*, *Phys. Rev. B* **87** (Apr, 2013) 161119.

[62] A. C. Komarek, H. Roth, M. Cwik, W.-D. Stein, J. Baier, M. Kriener, F. Bourée, T. Lorenz, and M. Braden, *Magnetoelastic coupling in $RTiO_3$ ($R = \mathrm{La, Nd, Sm, Gd, Y}$) investigated with diffraction techniques and thermal expansion measurements*, *Phys. Rev. B* **75** (Jun, 2007) 224402.

[63] K. Takubo, M. Shimuta, J. E. Kim, K. Kato, M. Takata, and T. Katsufuji, *Crossover behavior of the crystal structure and the relation to magnetism in perovskite $RTiO_3$*, *Phys. Rev. B* **82** (Jul, 2010) 020401.

[64] T. Kiyama and M. Itoh, *Presence of 3d quadrupole moment in $LaTiO_3$ studied by $^{47,49}Ti$ NMR*, *Phys. Rev. Lett.* **91** (Oct, 2003) 167202.

[65] J. Akimitsu, H. Ichikawa, N. Eguchi, T. Miyano, M. Nishi, and K. Kakurai, *Direct observation of orbital ordering in $YTiO_3$ by means of the polarized neutron diffraction technique*, *Journal of the Physical Society of Japan* **70** (2001), no. 12 3475–3478.

[66] B. Jalan, R. Engel-Herbert, N. J. Wright, and S. Stemmer, *Growth of high-quality $SrTiO_3$ films using a hybrid molecular beam epitaxy approach*, *Journal of Vacuum Science & Technology A* **27** (2009), no. 3 461–464.

[67] P. Moetakef, D. G. Ouellette, J. Y. Zhang, T. A. Cain, S. J. Allen, and S. Stemmer, *Growth and properties of $GdTiO_3$ films prepared by hybrid molecular beam epitaxy*, *Journal of Crystal Growth* **355** (2012), no. 1 166 – 170.

[68] P. Moetakef, J. Y. Zhang, S. Raghavan, A. P. Kajdos, and S. Stemmer, *Growth window and effect of substrate symmetry in hybrid molecular beam epitaxy of a mott insulating rare earth titanate*, *Journal of Vacuum Science & Technology A: Vacuum, Surfaces, and Films* **31** (2013), no. 4 041503.

[69] J. M. LeBeau and S. Stemmer, *Experimental quantification of annular dark-field images in scanning transmission electron microscopy*, *Ultramicroscopy* **108** (2008), no. 12 1653 – 1658.

[70] D. O. Klenov, W. Donner, B. Foran, and S. Stemmer, *Impact of stress on oxygen vacancy ordering in epitaxial $(La_{0.5}Sr_{0.5})CoO_3$ thin films*, *Applied Physics Letters* **82** (2003), no. 20 3427–3429.

[71] J. Hwang, J. Y. Zhang, J. Son, and S. Stemmer, *Nanoscale quantification of octahedral tilts in perovskite films*, *Applied Physics Letters* **100** (2012), no. 19.

[72] J. Hwang, J. Son, J. Y. Zhang, A. Janotti, C. G. Van de Walle, and S. Stemmer, *Structural origins of the properties of rare earth nickelate superlattices*, *Phys. Rev. B* **87** (Feb, 2013) 060101.

[73] F. He, B. O. Wells, and S. M. Shapiro, *Strain phase diagram and domain orientation in $SrTiO_3$ thin films*, *Phys. Rev. Lett.* **94** (May, 2005) 176101.

[74] D. G. Ouellette, P. Moetakef, T. A. Cain, J. Y. Zhang, S. Stemmer, D. Emin, and S. J. Allen, *High-density two-dimensional small polaron gas in a delta-doped mott insulator*, *Scientific Reports* **3** (11, 2013) 3284 EP –.

[75] S. Pennycook, *Z-contrast stem for materials science*, *Ultramicroscopy* **30** (1989), no. 1 58 – 69.

[76] S. Pennycook and D. Jesson, *High-resolution Z-contrast imaging of crystals*, *Ultramicroscopy* **37** (1991), no. 1–4 14 – 38.

[77] P. Nellist and S. Pennycook, *Incoherent imaging using dynamically scattered coherent electrons*, *Ultramicroscopy* **78** (1999), no. 1–4 111 – 124.

[78] M. Heinrich, H.-A. Krug von Nidda, V. Fritsch, and A. Loidl, *Heavy-fermion formation at the metal-to-insulator transition in $Gd_{1-x}Sr_xTiO_3$*, *Phys. Rev. B* **63** (May, 2001) 193103.

[79] R. F. Loane, E. J. Kirkland, and J. Silcox, *Visibility of single heavy atoms on thin crystalline silicon in simulated annular dark-field STEM images*, *Acta Crystallographica Section A* **44** (Nov, 1988) 912–927.

[80] A. Mittal and K. A. Mkhoyan, *Limits in detecting an individual dopant atom embedded in a crystal*, *Ultramicroscopy* **111** (2011), no. 8 1101 – 1110.

[81] R. D. Shannon and C. T. Prewitt, *Effective ionic radii in oxides and fluorides*, *Acta Crystallographica Section B* **25** (May, 1969) 925–946.

[82] R. D. Shannon, *Revised effective ionic radii and systematic studies of interatomic distances in halides and chalcogenides*, *Acta Crystallographica Section A* **32** (Sep, 1976) 751–767.

[83] P. Blaha, K. Schwarz, G. Madsen, D. Kvasnicka, and J. Luitz, *WIEN2k: An augmented plane wave plus local orbitals program for calculating crystal properties*, .

[84] J. P. Perdew, K. Burke, and M. Ernzerhof, *Generalized gradient approximation made simple*, *Phys. Rev. Lett.* **77** (Oct, 1996) 3865–3868.

[85] J.-G. Cheng, Y. Sui, J.-S. Zhou, J. B. Goodenough, and W. H. Su, *Transition from orbital liquid to jahn-teller insulator in orthorhombic perovskites $RTiO_3$*, *Phys. Rev. Lett.* **101** (Aug, 2008) 087205.

[86] J. B. Goodenough and J.-S. Zhou, *Orbital ordering in orthorhombic perovskites*, *J. Mater. Chem.* **17** (2007) 2394–2405.

[87] M. Kubota, H. Nakao, Y. Murakami, Y. Taguchi, M. Iwama, and Y. Tokura, *Orbital ordering near a mott transition: Resonant x-ray scattering study of the perovskite Ti oxides $RTiO_3$ and $LaTiO_3$ (R = Gd, Sm, Nd, and La)*, *Phys. Rev. B* **70** (Dec, 2004) 245125.

[88] E. Pavarini, A. Yamasaki, J. Nuss, and O. K. Andersen, *How chemistry controls electron localization in $3d^1$ perovskites: a Wannier-function study*, *New Journal of Physics* **7** (2005), no. 1 188.

[89] C. W. Turner and J. Greedan, *Ferrimagnetism in the rare earth titanium (iii) oxides, $RTiO_3$; R = Gd, Tb, Dy, Ho, Er, Tm*, *Journal of Solid State Chemistry* **34** (1980), no. 2 207 – 213.

[90] G. Amow, J.-S. Zhou, and J. Goodenough, *Peculiar magnetism of the $Sm_{1-x}Gd_xTiO_3$ system*, *Journal of Solid State Chemistry* **154** (2000), no. 2 619 – 625.

[91] L. M. Roth, *Simple narrow-band model of ferromagnetism due to intra-atomic exchange*, *Phys. Rev.* **149** (Sep, 1966) 306–308.

[92] S. Inagaki, *Effect of orbital degeneracy and intra-atomic exchange on the occurrence of ferromagnetism*, *Journal of the Physical Society of Japan* **39** (1975), no. 3 596–604.

[93] D. Khomskii and K. Kugel, *Orbital and magnetic structure of two-dimensional ferromagnets with Jahn-Teller ions*, *Solid State Communications* **13** (1973), no. 7 763 – 766.

[94] P. A. Lee, N. Nagaosa, and X.-G. Wen, *Doping a Mott insulator: Physics of high-temperature superconductivity*, *Rev. Mod. Phys.* **78** (Jan, 2006) 17–85.

[95] S. Lee, R. Chen, and L. Balents, *Metal-insulator transition in a two-band model for the perovskite nickelates*, *Phys. Rev. B* **84** (Oct, 2011) 165119.

[96] T. Mizokawa, H. Namatame, A. Fujimori, K. Akeyama, H. Kondoh, H. Kuroda, and N. Kosugi, *Origin of the band gap in the negative charge-transfer-energy compound $NaCuO_2$*, *Phys. Rev. Lett.* **67** (Sep, 1991) 1638–1641.

[97] A. Subedi, O. E. Peil, and A. Georges, *Low-energy description of the metal-insulator transition in the rare-earth nickelates*, *Phys. Rev. B* **91** (Feb, 2015) 075128.

[98] J. B. Torrance, P. Lacorro, C. Asavaroengchai, and R. M. Metzger, *Simple and perovskite oxides of transition-metals: Why some are metallic, while most are insulating*, *Journal of Solid State Chemistry* **90** (1991), no. 1 168 – 172.

[99] J. Zaanen, G. A. Sawatzky, and J. W. Allen, *Band gaps and electronic structure of transition-metal compounds*, *Phys. Rev. Lett.* **55** (Jul, 1985) 418–421.

[100] M. L. Medarde, *Structural, magnetic and electronic properties of $RNiO_3$ perovskites (R = rare earth)*, *Journal of Physics: Condensed Matter* **9** (1997), no. 8 1679.

[101] G. Catalan, *Progress in perovskite nickelate research*, *Phase Transitions* **81** (2008), no. 7-8 729–749.

[102] J. B. Torrance, P. Lacorre, A. I. Nazzal, E. J. Ansaldo, and C. Niedermayer, *Systematic study of insulator-metal transitions in perovskites $RNiO_3$ (R = Pr, Nd, Sm, Eu) due to closing of charge-transfer gap*, *Phys. Rev. B* **45** (Apr, 1992) 8209–8212.

[103] P. C. Canfield, J. D. Thompson, S.-W. Cheong, and L. W. Rupp, *Extraordinary pressure dependence of the metal-to-insulator transition in the charge-transfer compounds $NdNiO_3$ and $PrNiO_3$*, *Phys. Rev. B* **47** (May, 1993) 12357–12360.

[104] X. Obradors, L. M. Paulius, M. B. Maple, J. B. Torrance, A. I. Nazzal, J. Fontcuberta, and X. Granados, *Pressure dependence of the metal-insulator transition in the charge-transfer oxides $RNiO_3$ (R = Pr, Nd, $Nd_{0.7}La_{0.3}$*, *Phys. Rev. B* **47** (May, 1993) 12353–12356.

[105] A. J. Hauser, E. Mikheev, N. E. Moreno, J. Hwang, J. Y. Zhang, and S. Stemmer, *Correlation between stoichiometry, strain, and metal-insulator transitions of $NdNiO_3$ films*, *Applied Physics Letters* **106** (2015), no. 9.

[106] J. Liu, M. Kareev, B. Gray, J. W. Kim, P. Ryan, B. Dabrowski, J. W. Freeland, and J. Chakhalian, *Strain-mediated metal-insulator transition in epitaxial ultrathin films of $NdNiO_3$*, *Applied Physics Letters* **96** (2010), no. 23.

[107] E. Mikheev, A. J. Hauser, B. Himmetoglu, N. E. Moreno, A. Janotti, C. G. Van de Walle, and S. Stemmer, *Tuning bad metal and non-Fermi liquid behavior in a Mott material: Rare-earth nickelate thin films*, *Science Advances* **1** (2015), no. 10.

[108] M. K. Stewart, J. Liu, M. Kareev, J. Chakhalian, and D. N. Basov, *Mott physics near the insulator-to-metal transition in $NdNiO_3$*, *Phys. Rev. Lett.* **107** (Oct, 2011) 176401.

[109] A. Tiwari, C. Jin, and J. Narayan, *Strain-induced tuning of metal–insulator transition in $NdNiO_3$*, *Applied Physics Letters* **80** (2002), no. 21 4039–4041.

[110] G. Catalan, R. M. Bowman, and J. M. Gregg, *Metal-insulator transitions in $NdNiO_3$ thin films*, *Phys. Rev. B* **62** (Sep, 2000) 7892–7900.

[111] P. Lacorre, J. Torrance, J. Pannetier, A. Nazzal, P. Wang, and T. Huang, *Synthesis, crystal structure, and properties of metallic $PrNiO_3$: Comparison with metallic $NdNiO_3$ and semiconducting $SmNiO_3$*, *Journal of Solid State Chemistry* **91** (1991), no. 2 225 – 237.

[112] G. Demazeau, A. Marbeuf, M. Pouchard, and P. Hagenmuller, *Sur une série de composés oxygènes du nickel trivalent derivés de la perovskite*, *Journal of Solid State Chemistry* **3** (1971), no. 4 582 – 589.

[113] J. L. García-Muñoz, J. Rodríguez-Carvajal, P. Lacorre, and J. B. Torrance, *Neutron-diffraction study of $RNiO_3$ (R = La, Pr, Nd, Sm): Electronically induced structural changes across the metal-insulator transition*, *Phys. Rev. B* **46** (Aug, 1992) 4414–4425.

[114] J. L. García-Muñoz, J. Rodríguez-Carvajal, and P. Lacorre, *Neutron-diffraction study of the magnetic ordering in the insulating regime of the perovskites $RNiO_3$ (R = Pr and Nd)*, *Phys. Rev. B* **50** (Jul, 1994) 978–992.

[115] J. Rodríguez-Carvajal, S. Rosenkranz, M. Medarde, P. Lacorre, M. T. Fernandez-Díaz, F. Fauth, and V. Trounov, *Neutron-diffraction study of the magnetic and orbital ordering in $^{154}SmNiO_3$ and $^{153}EuNiO_3$*, *Phys. Rev. B* **57** (Jan, 1998) 456–464.

[116] V. Scagnoli, U. Staub, A. M. Mulders, M. Janousch, G. I. Meijer, G. Hammerl, J. M. Tonnerre, and N. Stojic, *Role of magnetic and orbital ordering at the metal-insulator transition in $NdNiO_3$*, *Phys. Rev. B* **73** (Mar, 2006) 100409.

[117] J. L. García-Muñoz, M. A. G. Aranda, J. A. Alonso, and M. J. Martínez-Lope, *Structure and charge order in the antiferromagnetic band-insulating phase of $NdNiO_3$*, *Phys. Rev. B* **79** (Apr, 2009) 134432.

[118] M. Medarde, C. Dallera, M. Grioni, B. Delley, F. Vernay, J. Mesot, M. Sikora, J. A. Alonso, and M. J. Martínez-Lope, *Charge disproportionation in $RNiO_3$ perovskites (R = rare earth) from high-resolution x-ray absorption spectroscopy*, *Phys. Rev. B* **80** (Dec, 2009) 245105.

[119] I. I. Mazin, D. I. Khomskii, R. Lengsdorf, J. A. Alonso, W. G. Marshall, R. M. Ibberson, A. Podlesnyak, M. J. Martínez-Lope, and M. M. Abd-Elmeguid, *Charge ordering as alternative to Jahn-Teller distortion*, *Phys. Rev. Lett.* **98** (Apr, 2007) 176406.

[120] S. Johnston, A. Mukherjee, I. Elfimov, M. Berciu, and G. A. Sawatzky, *Charge disproportionation without charge transfer in the rare-earth-element nickelates as a possible mechanism for the metal-insulator transition*, *Phys. Rev. Lett.* **112** (Mar, 2014) 106404.

[121] D. Meyers, J. Liu, J. W. Freeland, S. Middey, M. Kareev, J. M. Zuo, Y.-D. Chuang, J. W. Kim, P. J. Ryan, and J. Chakhalian, *Selective interface control of order parameters in complex oxides*, *arXiv* (05, 2015).

[122] M. H. Upton, Y. Choi, H. Park, J. Liu, D. Meyers, J. Chakhalian, S. Middey, J.-W. Kim, and P. J. Ryan, *Novel electronic behavior driving $NdNiO_3$ metal-insulator transition*, *Phys. Rev. Lett.* **115** (Jul, 2015) 036401.

[123] V. Scagnoli, U. Staub, M. Janousch, A. M. Mulders, M. Shi, G. I. Meijer, S. Rosenkranz, S. B. Wilkins, L. Paolasini, J. Karpinski, S. M. Kazakov, and S. W. Lovesey, *Charge disproportionation and search for orbital ordering in $NdNiO_3$ by use of resonant x-ray diffraction*, *Phys. Rev. B* **72** (Oct, 2005) 155111.

[124] U. Staub, G. I. Meijer, F. Fauth, R. Allenspach, J. G. Bednorz, J. Karpinski, S. M. Kazakov, L. Paolasini, and F. d'Acapito, *Direct observation of charge order in an epitaxial $NdNiO_3$ film*, *Phys. Rev. Lett.* **88** (Mar, 2002) 126402.

[125] Z. He and A. J. Millis, *Strain control of electronic phase in rare-earth nickelates*, *Phys. Rev. B* **91** (May, 2015) 195138.

[126] H. Park, A. J. Millis, and C. A. Marianetti, *Site-selective Mott transition in rare-earth-element nickelates*, *Phys. Rev. Lett.* **109** (Oct, 2012) 156402.

[127] J. M. LeBeau, A. J. D'Alfonso, N. J. Wright, L. J. Allen, and S. Stemmer, *Determining ferroelectric polarity at the nanoscale*, *Applied Physics Letters* **98** (2011), no. 5 052904.

[128] J. Liu, M. Kargarian, M. Kareev, B. Gray, P. J. Ryan, A. Cruz, N. Tahir, Y.-D. Chuang, J. Guo, J. M. Rondinelli, J. W. Freeland, G. A. Fiete, and J. Chakhalian, *Heterointerface engineered electronic and magnetic phases of $NdNiO_3$ thin films*, *Nat Commun* **4** (11, 2013).

[129] P. Hansmann, X. Yang, A. Toschi, G. Khaliullin, O. K. Andersen, and K. Held, *Turning a nickelate fermi surface into a cupratelike one through heterostructuring*, *Phys. Rev. Lett.* **103** (Jun, 2009) 016401.

[130] J. Chaloupka and G. Khaliullin, *Orbital order and possible superconductivity in $LaNiO_3/LaMO_3$ superlattices*, *Phys. Rev. Lett.* **100** (Jan, 2008) 016404.

[131] A. S. Disa, D. P. Kumah, J. H. Ngai, E. D. Specht, D. A. Arena, F. J. Walker, and C. H. Ahn, *Phase diagram of compressively strained nickelate thin films*, *APL Mater.* **1** (2013), no. 3.

[132] L. Vasylechko, L. Akselrud, W. Morgenroth, U. Bismayer, A. Matkovskii, and D. Savytskii, *The crystal structure of $NdGaO_3$ at 100 k and 293 k based on synchrotron data*, *Journal of Alloys and Compounds* **297** (2000), no. 1–2 46 – 52.

[133] A. M. Glazer, *Simple ways of determining perovskite structures*, *Acta Crystallographica Section A* **31** (Nov, 1975) 756–762.

[134] J. M. Cowley, J. C. H. Spence, M. Tanaka, B. K. Vainshtein, B. B. Zvyagin, P. A. Penczek, and D. L. Dorset, *Electron diffraction and electron microscopy in structure determination*, in *INTERNATIONAL TABLES FOR CRYSTALLOGRAPHY, VOL. B: RECIPROCAL SPACE, THIRD EDITION*, vol. B of *International Tables for Crystallography Volume B*, pp. 297–402. SPRINGER, PO BOX 17, 3300 AA DORDRECHT, NETHERLANDS, 2008.

[135] S. Pennycook and P. Nellist, eds., *Scanning Transmission Electron Microscopy: Imaging and Analysis*. Springer New York, 2011.

[136] P. M. Voyles, D. A. Muller, J. L. Grazul, P. H. Citrin, and H. J. L. Gossmann, *Atomic-scale imaging of individual dopant atoms and clusters in highly n-type bulk Si*, *Nature* **416** (04, 2002) 826–829.

[137] K. van Benthem, A. R. Lupini, M. P. Oxley, S. D. Findlay, L. J. Allen, and S. J. Pennycook, *Three-dimensional {ADF} imaging of individual atoms by through-focal series scanning transmission electron microscopy*, *Ultramicroscopy* **106** (2006), no. 11–12 1062 – 1068. Proceedings of the International Workshop on Enhanced Data Generated by ElectronsProceedings of the International Workshop on Enhanced Data Generated by Electrons.

[138] S. H. Oh, K. van Benthem, S. I. Molina, A. Y. Borisevich, W. Luo, P. Werner, N. D. Zakharov, D. Kumar, S. T. Pantelides, and S. J. Pennycook, *Point defect configurations of supersaturated au atoms inside Si nanowires*, *Nano Letters* **8** (2008), no. 4 1016–1019.

[139] H. Okuno, J.-L. Rouvière, P.-H. Jouneau, P. Bayle-Guillemaud, and B. Daudin, *Visualization of Tm dopant atoms diffused out of GaN quantum dots*, *Applied Physics Letters* **96** (2010), no. 25.

[140] M. Couillard, G. Radtke, A. P. Knights, and G. A. Botton, *Three-dimensional atomic structure of metastable nanoclusters in doped semiconductors*, *Phys. Rev. Lett.* **107** (Oct, 2011) 186104.

[141] M. Bar-Sadan, J. Barthel, H. Shtrikman, and L. Houben, *Direct imaging of single Au atoms within GaAs nanowires*, *Nano Letters* **12** (2012), no. 5 2352–2356.

[142] O. L. Krivanek, M. F. Chisholm, V. Nicolosi, T. J. Pennycook, G. J. Corbin, N. Dellby, M. F. Murfitt, C. S. Own, Z. S. Szilagyi, M. P. Oxley, S. T. Pantelides, and S. J. Pennycook, *Atom-by-atom structural and chemical analysis by annular dark-field electron microscopy*, *Nature* **464** (03, 2010) 571–574.

[143] M. Varela, S. D. Findlay, A. R. Lupini, H. M. Christen, A. Y. Borisevich, N. Dellby, O. L. Krivanek, P. D. Nellist, M. P. Oxley, L. J. Allen, and S. J. Pennycook, *Spectroscopic imaging of single atoms within a bulk solid*, *Phys. Rev. Lett.* **92** (Mar, 2004) 095502.

[144] A. A. Gunawan, K. A. Mkhoyan, A. W. Wills, M. G. Thomas, and D. J. Norris, *Imaging "invisible" dopant atoms in semiconductor nanocrystals*, *Nano Letters* **11** (2011), no. 12 5553–5557.

[145] M. D. Rossell, Q. M. Ramasse, S. D. Findlay, F. Rechberger, R. Erni, and M. Niederberger, *Direct imaging of dopant clustering in metal–oxide nanoparticles*, *ACS Nano* **6** (2012), no. 8 7077–7083.

[146] G.-z. Zhu, S. Lazar, A. P. Knights, and G. A. Botton, *Atomic-level 2-dimensional chemical mapping and imaging of individual dopants in a phosphor crystal*, *Phys. Chem. Chem. Phys.* **15** (2013) 11420–11426.

[147] A. Howie, *Image contrast and localized signal selection techniques*, *Journal of Microscopy* **117** (1979), no. 1 11–23.

[148] R. F. Loane, P. Xu, and J. Silcox, *Incoherent imaging of zone axis crystals with ADF STEM*, *Ultramicroscopy* **40** (1992), no. 2 121 – 138.

[149] S. Hillyard and J. Silcox, *Detector geometry, thermal diffuse scattering and strain effects in ADF STEM imaging*, *Ultramicroscopy* **58** (1995), no. 1 6 – 17.

[150] D. E. Jesson and S. J. Pennycook, *Incoherent imaging of crystals using thermally scattered electrons*, *Proceedings of the Royal Society of London A: Mathematical, Physical and Engineering Sciences* **449** (1995), no. 1936 273–293.

[151] J. M. LeBeau, S. D. Findlay, L. J. Allen, and S. Stemmer, *Standardless atom counting in scanning transmission electron microscopy*, *Nano Letters* **10** (2010), no. 11 4405–4408.

[152] S. V. Aert, J. Verbeeck, R. Erni, S. Bals, M. Luysberg, D. V. Dyck, and G. V. Tendeloo, *Quantitative atomic resolution mapping using high-angle annular dark field scanning transmission electron microscopy*, *Ultramicroscopy* **109** (2009), no. 10 1236 – 1244.

[153] S. Kim, Y. Oshima, H. Sawada, T. Kaneyama, Y. Kondo, M. Takeguchi, Y. Nakayama, Y. Tanishiro, and K. Takayanagi, *Quantitative annular dark-field STEM images of a silicon crystal using a large-angle convergent electron probe with a 300-kV cold field-emission gun*, *Journal of Electron Microscopy* **60** (2011), no. 2 109–116.

[154] A. De Backer, G. Martinez, A. Rosenauer, and S. V. Aert, *Atom counting in HAADF STEM using a statistical model-based approach: Methodology, possibilities, and inherent limitations*, *Ultramicroscopy* **134** (2013) 23 – 33.

[155] Z. W. Wang, Z. Y. Li, S. J. Park, A. Abdela, D. Tang, and R. E. Palmer, *Quantitative Z-contrast imaging in the scanning transmission electron microscope with size-selected clusters*, *Phys. Rev. B* **84** (Aug, 2011) 073408.

[156] J. M. LeBeau, S. D. Findlay, X. Wang, A. J. Jacobson, L. J. Allen, and S. Stemmer, *High-angle scattering of fast electrons from crystals containing heavy elements: Simulation and experiment*, *Phys. Rev. B* **79** (Jun, 2009) 214110.

[157] M. Pierre, R. Wacquez, X. Jehl, M. Sanquer, M. Vinet, and O. Cueto, *Single-donor ionization energies in a nanoscale CMOS channel*, *Nat Nano* **5** (02, 2010) 133–137.

[158] G. P. Lansbergen, R. Rahman, C. J. Wellard, I. Woo, J. Caro, N. Collaert, S. Biesemans, G. Klimeck, L. C. L. Hollenberg, and S. Rogge, *Gate-induced quantum-confinement transition of a single dopant atom in a silicon FinFET*, *Nat Phys* **4** (08, 2008) 656–661.

[159] P. M. Koenraad and M. E. Flatte, *Single dopants in semiconductors*, *Nat Mater* **10** (02, 2011) 91–100.

[160] R. Erni, M. D. Rossell, C. Kisielowski, and U. Dahmen, *Atomic-resolution imaging with a sub-50-pm electron probe*, *Phys. Rev. Lett.* **102** (Mar, 2009) 096101.

[161] P. E. Batson, N. Dellby, and O. L. Krivanek, *Sub-angstrom resolution using aberration corrected electron optics*, *Nature* **418** (08, 2002) 617–620.

[162] P. D. Nellist, M. F. Chisholm, N. Dellby, O. L. Krivanek, M. F. Murfitt, Z. S. Szilagyi, A. R. Lupini, A. Borisevich, W. H. Sides, and S. J. Pennycook, *Direct sub-angstrom imaging of a crystal lattice*, *Science* **305** (2004), no. 5691 1741–1741.

[163] D. A. Muller, L. F. Kourkoutis, M. Murfitt, J. H. Song, H. Y. Hwang, J. Silcox, N. Dellby, and O. L. Krivanek, *Atomic-scale chemical imaging of composition and bonding by aberration-corrected microscopy*, *Science* **319** (2008), no. 5866 1073–1076.

[164] P. Voyles, D. Muller, and E. Kirkland, *Depth-dependent imaging of individual dopant atoms in silicon*, *Microscopy and Microanalysis* **10** (4, 2004) 291–300.

[165] H. L. Xin and D. A. Muller, *Three-dimensional imaging in aberration-corrected electron microscopes*, *Microscopy and Microanalysis* **16** (8, 2010) 445–455.

[166] P. D. Nellist and P. Wang, *Optical sectioning and confocal imaging and analysis in the transmission electron microscope*, *Annual Review of Materials Research* **42** (2012), no. 1 125–143.

[167] A. J. Koster, U. Ziese, A. J. Verkleij, A. H. Janssen, , and K. P. de Jong, *Three-dimensional transmission electron microscopy: a novel imaging and characterization technique with nanometer scale resolution for materials science*, *The Journal of Physical Chemistry B* **104** (2000), no. 40 9368–9370.

[168] P. Midgley and M. Weyland, *3D electron microscopy in the physical sciences: the development of Z-contrast and EFTEM tomography*, *Ultramicroscopy* **96** (2003), no. 3–4 413 – 431. Proceedings of the International Workshop on Strategies and Advances in Atomic Level Spectroscopy and Analysis.

[169] R. Ishikawa, A. R. Lupini, S. D. Findlay, T. Taniguchi, and S. J. Pennycook, *Three-dimensional location of a single dopant with atomic precision by aberration-corrected scanning transmission electron microscopy*, *Nano Letters* **14** (2014), no. 4 1903–1908.

[170] M. Treacy and J. Gibson, *Coherence and multiple scattering in "Z-contrast" images*, *Ultramicroscopy* **52** (1993), no. 1 31 – 53.

[171] M. Treacy, J. Gibson, K. Short, and S. Rice, *Channeling effects from impurity atoms in the high-angle annular detector of the stem*, *Ultramicroscopy* **26** (1988), no. 1–2 133 – 142.

[172] P. Voyles, J. Grazul, and D. Muller, *Imaging individual atoms inside crystals with ADF-STEM*, *Ultramicroscopy* **96** (2003), no. 3–4 251 – 273. Proceedings of the International Workshop on Strategies and Advances in Atomic Level Spectroscopy and Analysis.

[173] A. Lupini, A. Borisevich, J. Idrobo, H. Christen, M. Biegalski, and S. Pennycook, *Characterizing the two- and three-dimensional resolution of an improved aberration-corrected STEM*, *Microscopy and Microanalysis* **15** (10, 2009) 441–453.

[174] T. Grieb, K. Muller, R. Fritz, V. Grillo, M. Schowalter, K. Volz, and A. Rosenauer, *Quantitative chemical evaluation of dilute GaNAs using ADF STEM: Avoiding surface strain induced artifacts*, *Ultramicroscopy* **129** (2013), no. 0 1 – 9.

[175] L. Jones and P. D. Nellist, *Identifying and correcting scan noise and drift in the scanning transmission electron microscope*, *Microscopy and Microanalysis* **19** (8, 2013) 1050–1060.

[176] M. M. Treacy, *Z dependence of electron scattering by single atoms into annular dark-field detectors*, *Microscopy and Microanalysis* **17** (12, 2011) 847–858.

[177] E. Okunishi, I. Ishikawa, H. Sawada, F. Hosokawa, M. Hori, and Y. Kondo, *Visualization of light elements at ultrahigh resolution by STEM annular bright field microscopy*, *Microscopy and Microanalysis* **15** (7, 2009) 164–165.

[178] N. Shibata, Y. Kohno, S. D. Findlay, H. Sawada, Y. Kondo, and Y. Ikuhara, *New area detector for atomic-resolution scanning transmission electron microscopy*, *Journal of Electron Microscopy* **59** (2010), no. 6 473–479.

[179] S. D. Findlay, N. Shibata, H. Sawada, E. Okunishi, Y. Kondo, T. Yamamoto, and Y. Ikuhara, *Robust atomic resolution imaging of light elements using scanning transmission electron microscopy*, *Applied Physics Letters* **95** (2009), no. 19.

[180] N. Shibata, S. D. Findlay, Y. Kohno, H. Sawada, Y. Kondo, and Y. Ikuhara, *Differential phase-contrast microscopy at atomic resolution*, *Nat Phys* **8** (08, 2012) 611–615.

[181] M. Isaacson, D. Kopf, M. Ohtsuki, and M. Utlaut, *Atomic imaging using the dark-field annular detector in the stem*, *Ultramicroscopy* **4** (1979), no. 1 101 – 104.

[182] E. James and N. Browning, *Practical aspects of atomic resolution imaging and analysis in STEM*, *Ultramicroscopy* **78** (1999), no. 1–4 125 – 139.

[183] D. E. Jesson and S. J. Pennycook, *Incoherent imaging of thin specimens using coherently scattered electrons*, *Proceedings of the Royal Society of London A: Mathematical, Physical and Engineering Sciences* **441** (1993), no. 1912 261–281.

[184] D. O. Klenov and S. Stemmer, *Contributions to the contrast in experimental high-angle annular dark-field images*, *Ultramicroscopy* **106** (2006), no. 10 889 – 901.

[185] S. Findlay and J. LeBeau, *Detector non-uniformity in scanning transmission electron microscopy*, *Ultramicroscopy* **124** (2013), no. 0 52 – 60.

[186] H. E. MacArthur, K. E. MacArthur, T. J. Pennycook, E. Okunishi, A. J. D'Alfonso, N. Lugg, L. J. Allen, and P. D. Nellist, *Probe integrated scattering cross sections in the analysis of atomic resolution HAADF STEM images*, *Ultramicroscopy* **133** (2013) 109 – 119.

[187] I. Daberkow, K.-H. Herrmann, and F. Lenz, *A configurable angle-resolving detector system in STEM*, *Ultramicroscopy* **50** (1993), no. 1 75 – 82.

[188] M. Haider, A. Epstein, P. Jarron, and C. Boulin, *A versatile, software configurable multichannel STEM detector for angle-resolved imaging*, *Ultramicroscopy* **54** (1994), no. 1 41 – 59.

[189] M. Hammel and H. Rose, *Optimum rotationally symmetric detector configurations for phase-contrast imaging in scanning transmission electron microscopy*, *Ultramicroscopy* **58** (1995), no. 3–4 403 – 415.

[190] T. Caswell, P. Ercius, M. Tate, A. Ercan, S. Gruner, and D. Muller, *A high-speed area detector for novel imaging techniques in a scanning transmission electron microscope*, *Ultramicroscopy* **109** (2009), no. 4 304 – 311.

[191] G. McMullan, A. Faruqi, D. Clare, and R. Henderson, *Comparison of optimal performance at 300 keV of three direct electron detectors for use in low dose electron microscopy*, *Ultramicroscopy* **147** (2014) 156 – 163.

[192] S. Findlay, L. Allen, M. Oxley, and C. Rossouw, *Lattice-resolution contrast from a focused coherent electron probe. part ii*, *Ultramicroscopy* **96** (2003), no. 1 65 – 81.

[193] C. J. Humphreys, *The scattering of fast electrons by crystals*, *Reports on Progress in Physics* **42** (1979), no. 11 1825.

[194] L. J. Allen and C. J. Rossouw, *Effects of thermal diffuse scattering and surface tilt on diffraction and channeling of fast electrons in CdTe*, *Phys. Rev. B* **39** (Apr, 1989) 8313–8321.

[195] H. Bethe, *Theorie der beugung von elektronen an kristallen*, *Annalen der Physik* **392** (1928), no. 17 55–129.

[196] J. M. Cowley and A. F. Moodie, *The scattering of electrons by atoms and crystals. I. A new theoretical approach*, *Acta Crystallographica* **10** (Oct, 1957) 609–619.

[197] R. F. Loane, P. Xu, and J. Silcox, *Thermal vibrations in convergent-beam electron diffraction*, *Acta Crystallographica Section A* **47** (May, 1991) 267–278.

[198] D. Van Dyck, *Is the frozen phonon model adequate to describe inelastic phonon scattering?*, *Ultramicroscopy* **109** (2009), no. 6 677 – 682.

[199] Y. Wang, C. Nelson, A. Melville, B. Winchester, S. Shang, Z.-K. Liu, D. G. Schlom, X. Pan, and L.-Q. Chen, *$BiFeO_3$ domain wall energies and structures: A combined experimental and density functional theory+**U** study*, *Phys. Rev. Lett.* **110** (Jun, 2013) 267601.

[200] A. Rosenauer, K. Gries, K. Müller, A. Pretorius, M. Schowalter, A. Avramescu, K. Engl, and S. Lutgen, *Measurement of specimen thickness and composition in $Al_xGa_{1-x}N/GaN$ using high-angle annular dark field images*, *Ultramicroscopy* **109** (2009), no. 9 1171 – 1182.